TIME-LAPSE AND INFRARED THERMOGRAPHIC DEFECTS/FEATURES CLASSIFICATIONS FOR AGEING BUILDING ENVELOPES AND SECONDARY LANDSLIDE HAZARDS

CHIU SIN YAU LYDIA

PhD

The Hong Kong Polytechnic University

2025

The Hong Kong Polytechnic University

Department of Land Surveying and Geo-informatics

Time-lapse and Infrared Thermographic Defects/Features
Classifications for Ageing Building Envelopes and Secondary
Landslide Hazards

Chiu Sin Yau Lydia

A thesis submitted in partial fulfillment of the requirements for
the degree of Doctor of Philosophy

December 2024

CERTIFICATE OF ORIGINALITY

I hereby declare that this thesis is my own work and that, to the best of my knowledge and belief, it reproduces no material previously published or written, nor material that has been accepted for the award of any other degree or diploma, except where due acknowledgment has been made in the text.

Signature: _____

Name of Student: Chiu Sin Yau Lydia

Abstract

Non-destructive testing (NDT) and remote sensing techniques in building and civil engineering have been widely adopted in defect/feature classification. Among various NDTs, research and implementation of Infrared Thermography (IRT) has increased rapidly since 2008. With its advantages of non-contact, remote from targets, effective data collection and rapid imaging of temperature distributions, IRT is commonly adopted for evaluating the conditions of building envelopes and secondary landslide hazards. For both building envelopes and secondary landslide hazards, the need for such quantitative evaluation is ever-increasing due to the ageing of buildings and extreme weather, respectively. But traditional snapshot IRT only provides qualitative results indicating the numbers and locations of the suspected defects, but not severity leading to potential hazards, such as falling tiles from height and hidden saturated water channels causing secondary landslides. The accuracy of IRT evaluation, and its usefulness are always highly in doubt.

This thesis develops a novel time-lapse IRT approach on evaluating building envelopes and the hazard of secondary landslide by making use of the different rates of change of heat transfer in different materials during heat absorption (illuminated by the Sun) and dissipation (during sunset). Time-lapse measurements of thermal contrasts were conducted by a ground-based IR camera and a UAS-IR camera for building envelopes and potential secondary landslides, respectively. A novel physical approach (Thermal Decay Mapping) and a statistical approach (Supervised Machine

Learning) were developed to conduct defects/features classification through a series of rigorous validation experiments. The defect classes of building envelopes were binary: debond or intact wall finishes, and defects/feature classes of slopes were rocks of different weathering states, visual/hidden cracks, moisture and vegetation. All these defects/features are of high engineering interest because ignorance would cause casualties which could be warned and prevented with the IRT approaches developed and validated in this thesis.

In the physical approach (Thermal Decay Mapping), thermal images with different time stamps were processed, and linear regression was performed on the temperature curves of each pixel on a natural logarithmic scale. The values in the natural logarithmic base (for both temperature and time) were normalized to retrieve the gradient of thermal decay of each pixel and generate a thermal decay map of the target of interest (i.e. building envelopes and secondary landslide hazards). Two thresholding methods, adaptive thresholding and Otsu's thresholding, were performed to generate binary images for defect classification. The performance of these thresholding methods was evaluated by the calculation of a confusion matrix (true positive, true negative, false positive and false negative). The results showed that the defect/feature classifications were further enhanced by making use of the pixel's standard deviation (SD method). For building inspection, the results reported an average accuracy of 80%, which is considered satisfactory in NDT's world. Meanwhile, for the slope inspection, vegetation, suspected moisture and suspected cracks could be successfully segmented, although accuracy could not be evaluated due to a lack of ground truth data.

In the statistical method (supervised machine learning), the classic logistic regression algorithm was adopted. The models were trained by datasets involving sample walls built with different wall finishing materials, yielding the highest, high and low emissivity values, and a rock slope with hexagonal rock columns. The results showed successful predictions on the target walls in the building datasets. For the bi-

nary images produced from the building datasets, the sizes of the suspected debonds can be estimated at an accuracy rate of 88%. This percentage can adequately predict the severity of those invisible debonds on building envelopes. But on the other hand, the prediction model for slope inspection could not return a favourable prediction. It was due to limitations like poorer spatial resolution measured by instantaneous field of view (IFOV), insufficient number of temperature data points in the training datasets, and complexity & mixture of various feature types, all of which were in comparison with datasets of building envelopes.

In general, quantitative IRT analysis was proven scientifically sound, feasible and practical for defect/feature classification for evaluation of both building envelope and hazard of secondary landslides. Various experimental, environmental and material factors, including data acquisition and materials' colours and texture affecting the performance of the two physical and statistical methods were thoroughly evaluated in this thesis. The findings, analysis and conclusions clearly pave the way for the NDT industry to migrate from arbitrary and qualitative defect mapping to scientific and quantitative analysis of defect severity in building envelopes and secondary landslide hazards.

Publications Arising from the Thesis

Journal article(s):

1. <u>Lydia Sin-Yau Chiu</u>, Wallace Wai-Lok Lai, Sónia Santos-Assunção, Sahib Singh Sandhu, Janet Fung-Chu Sham, Nelson Fat-Sang Chan, Jeffrey Chun-Fai Wong and Wai-Kin Leung (2023). A Feasibility Study of Thermal Infrared Imaging for Monitoring Natural Terrain—A Case Study in Hong Kong. *Remote Sensing* 15(24):5787.

2. <u>Lydia Sin-Yau Chiu</u>, Celia Y. Y. Yang and Wallace Wai-Lok Lai, "Characterization of Geotechnical and Geological Features with Time-Lapse Infrared Thermography and Geo-Spatial Technologies" (2025)(Submitted to Landslides).

3. <u>Lydia Sin-Yau Chiu</u>, Wallace Wai-Lok Lai and Janet Fung-Chu Sham. Time-lapse and infrared thermographic defects/features classifications for ageing building envelops, part 1: A physical thermal decay method (2025)(submitted to NDT and E International)

4. <u>Lydia Sin-Yau Chiu</u>, Wallace Wai-Lok Lai and Janet Fung-Chu Sham. Time-lapse and infrared thermographic defects/features classifications for ageing building envelops, part 2: A statistical machine Learning method. (2025)(submitted

iv

to NDT and E International)

Conference proceeding(s):

1. <u>S. Y. Chiu</u>, Wallace W. L. Lai, Janet F. C. Sham and Miranda C. Y. Lui, "Influence of cover depth towards quantitative size estimation of delaminations in external wall using passive infrared thermography", in *3rd Quantitative Infrared Thermography Asian Conference (QIRT-Asia 2019)* (2019).

2. Janet F. C. Sham, Wallace W. L. Lai and <u>S. Y. Chiu</u>, "Effects of thermal contrast on size estimation of debonds in different external wall's composite finishes via passive infrared thermography and a modified gradient algorithm", in *3rd Quantitative Infrared Thermography Asian Conference (QIRT-Asia 2019)* (2019).

3. <u>Lydia S. Y. Chiu</u>, Wallace W. L. Lai, Miranda C. Y. Lui, "Developing Quantifiable Defect Record for Tall Building Envelop using Passive Infrared Thermography and Building Information Modelling", in *15th Quantitative InfraRed Thermography Conference* (2020).

4. <u>Lydia Sin-Yau Chiu</u>, Wallace Wai-Lok Lai, Janet Fung-Chu Sham, and C. P. Yuen, "Selection of Thresholding for Defect Detection and Size Estimation of Building Exterior Wall Using Passive Infrared Thermography", in *17th Quantitative InfraRed Thermography Conference* (2024).

Acknowledgments

It has been a long journey for me to complete this thesis, especially during the COVID-19 pandemic, when every one in the society encountered different difficulties in their life. I am grateful that every one I love is strong enough to live through the pandemic.

During my journey, I received a lot of support and guidance from many people. Firstly, I would like to thank my chief supervisor, Ir Prof. Wallace Wai-Lok Lai, for his guidance and encouragement. During my bachelor degree, he introduced me the topic of infrared thermography in my final year project, and offered me the opportunity to start my PhD study, which was the beginning of this journey. I am grateful that my co-supervisor, Ir Prof. Chi-sun Poon, who gave me valuable insights in civil engineering.

I also would like to thank all of my colleagues in the research team, including Sahib and Nelson for helping in UAV data collection, Mr. Ho and Shing for organising the equipment, and especially Janet. She is the supportive guide during my journey, who shared her experience in the field of infrared thermography, and encouraged me to keep going when I encountered so many obstacles during the journey. Also a special shout-out to Phoebe, who offered valuable experience in programming on machine learning.

Lastly, I would like to show my gratitude to my family and friends, especially my

parents for all of their love and support. I also would like to give a special shoutout to my friends Kiki, Ivy, Manbo and Zoe. They keep me staying positive when I was overwhelmed by works and researches. Without them, I cannot complete this thesis.

Table of Contents

List of Figures

List of Tables

Chapter 1

Introduction

1.1 Background and Overview

Adopting non-destructive testing (NDT) techniques in defect/feature classification has been widely discussed in the research field, in which the implementation of Infrared Thermography (IRT) has increased rapidly since 2008, after the reviews of several international standards regarding IRT surveys such as ASTM D4788 for bridge deck inspection. In an IRT survey, defects/features on a target surface after heating can be identified in a thermal image (i.e. thermogram) captured by a thermal camera, due to the physical and thermal properties of the materials. Physical properties of the materials such as colours and textures, with the thermal properties including thermal conductivities, specific heat capacities and emissivities affect the rate of different modes of heat transfer of the target. The detector in a thermal camera can detect the heat radiation emitted and reflected by the target, and hence forms the visualization of the temperature distribution of the target in the form of thermograms. Hence, defects/features that are not visible or hard to notice in visual images can be captured in a thermal image. All of these phenomena will be discussed in the following chapters of this study. The key point is that IRT can be used to

1

identify defects/features in any targets when heat sources are provided.

There are various research in the field conducting defect detection and evaluation in different materials, such as concrete [1,2], composite materials [3,4] and stone panels [5], which experiments and data collection were mostly conducted in laboratories with controlled environment with active IRT using active sources of thermal stimulus. Unlike these experiments conducted in laboratories, passive IRT performed in an outdoor environment uses natural sunlight as the heat source, which means various environmental parameters cannot be manually controlled. This poses a challenge when performing defect/feature classification on an outdoor target such as a building envelope and natural terrain. In this thesis, with the development of image processing techniques and artificial intelligence, this limitation could be significantly improved with time-lapse thermography assisted with supervised machine learning. The two main targets will be building envelopes and slopes in natural terrain.

1.1.1   Building Envelope

The fast-growing population, ageing buildings and economic growth in the world, drive the ever-increasing need to develop and maintain existing infrastructures. Legislation and standards regarding building facade inspection have been established worldwide, which buildings of five or more stories to be frequently inspected, with the inspection frequency ranging from 5 to 12 years [6], including Hong Kong, one of the Asian cities with many tall buildings built along the hillside. For example, the Buildings Department of the Hong Kong government has established the "Mandatory Building Inspection Scheme (MBIS)". [7] MBIS requires owners of buildings aged 30 years or above to schedule a regular building inspection by a registered inspector every 10 years, which ensures existing buildings have proper maintenance and minimizes risks to public safety. The causes of material failure can be from corrosion of steel, delamination of render and cracks, which result in falling tiles and endanger the

pedestrian [8].

Traditional building inspection techniques including visual inspection and hammer tapping test are listed as the accepted non-destructive inspection techniques in MBIS. However, these traditional building inspection techniques depend heavily on labour and time as they mostly require scaffolding, which lowers the efficiency of large-scale inspection and increases the cost. Passive IRT, as a non-contact and non-destructive imaging technique, is accredited by the Hong Kong Laboratory Accreditation Scheme (HOKLAS) [9] and accepted in MBIS [7]. Invisible defects within the external wall finishes of buildings can be detected by IRT, which defects appear as abnormal temperature distributions in thermal images (thermograms) due to contrasts in the thermal conductive and emissive properties of air (defect) and intact areas (finishes). Although IRT can provide a fast and efficient inspection when compared to traditional building inspection techniques, IRT assessment in Hong Kong normally provides qualitative results, which indicate only the numbers and locations of defects, and highly depend upon the registered inspector's experience under HOKLAS and MBIS. Such information cannot reflect the severity of the detected defects, and hence it is unfavourable in maintenance planning. Quantifiable debond size estimation is a crucial procedure when attempting to improve the effectiveness of building maintenance, and the adoption of quantitative IRT in debond size estimation has proven to be feasible [10,11] for estimating the size of the debond and the cost of rehabilitation. Lai, Lee and Poon [10] utilized a spatial pixel differentiation algorithm to detect the boundaries of defects and hence estimated sizes. Yet their research only constructed a sample wall with one wall finishing material only (i.e. rendering). Therefore, it is necessary to perform experiments on other wall finishing materials since the difference in thermal properties of different materials commonly used for building envelopes will affect the thermal contrasts between the defect area and the intact area.

1.1.2   Secondary Landslide Hazards in Natural Terrain

Other than building safety, landslides in natural terrain are also one of the problems in Hong Kong endangering public safety. 601 landslides were reported in 2023 [12], including two recent and notable landslides (Yiu Hing Road Landslide and Shek O Road Landslide [13]) that occurred from 7 to 8 September 2023, when a Black rainstorm warning signal was issued on the day before the landslides occurred. A landslide of over 3000 cubic meters occurred at Yiu Hing Road, where the location is less than 100m from the residential area in Yiu Tung Estate, and this incident led to the closure of Yiu Hing Road and the maintenance work needed at least half a year to be completed. To address the landslides problem in Hong Kong, site investigation is the main approach in secondary landslide hazard survey, with the aid of different inspection techniques including topographic and geological mapping, aerial photographic imagery, borehole survey and other geophysical techniques to map out anomalies on slopes, but only a few non-invasive methods are available for secondary landslide hazard survey.

1.1.3   Time-lapse Passive Infrared Thermography Approach

Therefore, this thesis aims to develop a generic approach of time-lapse infrared thermography for automatic feature classification on both building external walls and natural terrain. For building inspection, thermal images of the external wall are performed by ground-based IRT, while rock cliffs or slopes can be inspected with the combination of unmanned aerial system (UAS) and IRT. Thermal contrast between the defect area and intact area was analysed to identify different features, including defects on buildings' envelopes, and cracks, moisture and other features on a slope.

In this thesis, there are two generic approaches for performing feature classification on building external walls and natural terrain, which are the physical approach (the time-lapse Thermal Decay Mapping method) and the statistical approach (the

machine learning method). This study utilized these two approaches in an attempt to perform a straightforward and automatic feature classification and size estimation: identifying debond and delaminations on building envelopes, and cracks, moisture and other features on slopes. In the time-lapse Thermal Decay Mapping method, thermal images with different time stamps were processed, and linear regression was performed on the temperature curves of each pixel. The values in the natural logarithmic base (for both temperature and time) were normalized to retrieve the gradient of thermal decay of each pixel and form a thermal decay map of the target (i.e. building envelope and secondary landslide hazards). Thresholding was performed to get a binary image for defect size estimation. In the machine learning method, the logistic regression algorithm was adopted, and the model was trained by datasets involving sample walls built with different wall finishing materials and slopes with hexagonal rock columns. Different factors including the instrumental, environmental and material factors were summarized in this thesis. The severity of the defects on building envelopes can be presented in the form of reference estimated sizes, and potential weakening areas on slopes can then be analysed from the feature classification results.

1.2 Research Objectives

The major objectives of this research are to:

1. Classify subsurface defects, including (1) debonds and delaminations, in building structures, and (2) rocks, cracks and vegetation in natural terrain using time-lapse thermal decay analysis and supervised machine learning, and evaluate different experimental, environmental and material factors affecting the detectability of subsurface defects and other features by thermal decay analysis and logistic regression.

2. Develop a time-lapse thermal decay method which utilises a sequence of thermal

images of the target surface, and visualise the resulting thermal decay gradient in the form of a time-lapse thermal decay Map highlighting the potential defects/features on the target.

3. Build a logistic regression machine learning model for classifying subsurface defects in building structures, and various features in natural terrain.

4. Develop a generic workflow for time-lapse and passive IRT by the proposed time-lapse Thermal Decay Mapping method and machine learning method

1.3   Contributions

This thesis aims to develop an automatic feature classification and defect size estimation using time-lapse infrared thermography in two approaches: the physical approach (the Thermal Decay Mapping method) and the statistical approach (the machine learning method). Considering building inspection, recent studies on quantitative infrared thermography analysis in the research fields either focused on concrete [1, 14–17] and composite samples [4, 18–20], energy loss in buildings envelope [21–23], or 3D thermal modelling [24–28]. Research on defect size estimation on building external walls is rather limited, due to the complication of dealing with different materials (i.e. windows, metal claddings, etc.). While the common practice in building inspection using IRT in Hong Kong only provides qualitative results indicating locations and numbers, it does not reflect the severity of the defects of the building. For secondary landslide hazards, the recent studies on geotechnical surveys using IRT focused on detecting anomalies on slopes [29–33], evaluating rock characteristics and properties [34–37], and combining IRT slope survey with other remote sensing technologies [38–42]. Only Loche et al. [42] adopted time-lapse infrared thermography in slope inspection, where the UAS-IRT system in their study was considered as ground-based IRT since the system was fixed on a platform on ground level

6

and did not perform an airborne survey. This thesis follows a similar data collection approach, which utilizes the flexibility of a UAS system to collect thermal images of a natural terrain remotely. Another significant study [43] proposed the calculation of a Cooling Rate Index (CRI) for analysing the degree of fracturing of rock masses. The CRI was a ratio between the variation of the average temperatures of the rock mass and the time interval, and there was only one CRI representing the whole rock mass surface since the average temperatures were used in the calculation. However, using the average temperatures to represent the entire rock mass surface could be a limitation when analysing rock masses with rough surfaces. The proposed Thermal Decay Mapping method in this thesis has a different approach and takes every pixel in the thermal images into consideration, where the thermal decay gradient in each pixel is calculated and visualised in the form of a thermal decay map. Hence, this thesis aims at developing an automatic feature classification and defect size estimation by the Thermal Decay Mapping method and machine learning method, which is currently lacking in the research field, and this thesis represents the first attempt at time-lapse infrared thermography in slope inspection and feature classification in Hong Kong [44]. Based on the estimated sizes retrieved from the proposed methods, this can be useful in the maintenance of buildings or slopes.

1.4 Thesis Organization

This thesis consists of eight chapters including this introduction chapter and bibliography.

In CHAPTER 2, works of literature on IR thermography on building structures and natural terrain are introduced, followed by reviews on surface and subsurface defect detection on building structures and natural terrain. Fundamental concepts on IR thermography and thermal properties of test materials are discussed and fundamental principles of passive and time-lapse thermography are reviewed. Subsurface

defect detection by passive and time-lapse thermography is examined.

CHAPTER 3 demonstrates the conceptual workflow for fulfilling the research objectives. It describes the design of the test specimens used in this study and the field data to be used for validation of the proposed workflow.

CHAPTER 4 and 5 summarise the results of the physical approach (the Thermal Decay Mapping method), including the parameters affecting the results on building wall finishes and rock slopes respectively.

In CHAPTER 6, the thermal image processing results by the statistical approach (the machine learning method) for building inspection and secondary landslide hazard inspection are summarized, with a discussion of different factors affecting defect detection in building structures, and the application of the machine learning method in slope feature classification.

Finally, CHAPTER 7 summarizes all the results obtained. Possible sources of errors are discussed and recommendations for future research are presented.

Chapter 2

Literature Review

2.1 Chapter Overview

This chapter first introduces the fundamentals of heat transfer and infrared thermography (IRT) and reviews the application of passive IRT and time-lapse IRT on building wall inspection and secondary landslide hazard monitoring and feature analysis. The limitations of IRT are summarized. The Thermal Decay Mapping method and the machine learning method are also reviewed.

2.2 Introduction to Heat Transfer

When adopting IRT in building and secondary landslide inspection, the operators need to know the basics of heat transfer to understand what affects the thermal contrast between the defect area and the intact area. The temperature in 0 K (degree Kelvin) is called absolute zero, and any object with a temperature above absolute zero emits heat energy. According to the second law of thermodynamics, when there is a difference in temperature in a physical system, heat will be transferred from a

high-temperature region to a low-temperature region, and there are three modes of heat transfer: conduction, convection and radiation.

2.2.1 Conduction Heat Transfer

Conduction occurs whenever there is a temperature difference between two solid bodies in contact or between different parts of a single body [45]. Heat energy (kinetic energy) is transferred between molecules by collision. This type of heat transmission happens in gases, liquids and solids. However, heat conduction seldom occurs in liquids and gases (i.e. fluids) since the molecules in fluids are further apart and hence less collision happens. When dealing with an opaque material (neither transparent nor translucent), heat conduction transfer is the only internal mode of heat transfer. The equation for calculating the rate of conduction heat transfer is known as the Fourier Law, which is expressed as:

$$q_k = \text{-}k\frac{dT}{dx} \tag{2.1}$$

Where q_k (conduction heat flux) is the rate of heat transfer in x direction per unit area perpendicular to the temperature gradient $\frac{dT}{dx}$, where dT is the temperature difference between two mediums. The constant k in Eq. (2.1) is a proportional constant known as thermal conductivity. The minus sign in the equation indicates the decrease in temperature along the temperature gradient. k is the same in all directions when dealing with isotropic materials. However, building envelopes or slopes are anisotropic materials, for which k varies due to the difference in materials inside the anisotropic materials. When choosing appropriate equations for understanding heat transfer within the target, selecting a suitable coordinate system according to the target geometrics is crucial, as equations of conduction heat transfer can be in different coordinate systems, including Cartesian, cylindrical and spherical coordinates. Since

buildings and natural slopes are commonly rectangular and only the surfaces of the slopes are inspected, the Cartesian coordinate system is selected in this study.

After selecting a suitable coordinate system, the number of dimensions needs to be considered in the calculation of conduction heat transfer. One-dimensional (1D) heat conduction is applicable when dealing with objects which are very large in size and whose area is considered infinite when compared to their thickness. Two-dimensional (2D) and three-dimensional (3D) conductions are applicable when conduction heat transfer occurs in two or three directions respectively.

When the surface temperature of an object is altered, the temperature within the body changes according to the second law of thermodynamics until the temperature within the body reaches an equilibrium state. In this study, both the surface of the building envelope and the slope are heated up by natural sunlight, and hence the phenomenon can be demonstrated by a 3D heat conduction equation, which can be presented by the following equation [45]:

$$\frac{\partial^2 T}{\partial x^2} + \frac{\partial^2 T}{\partial y^2} + \frac{\partial^2 T}{\partial z^2} = \frac{1}{\alpha}\frac{\partial T}{\partial t} \tag{2.2}$$

where T is the temperature in K, t is the time elapsed, α is thermal diffusivity (i.e. $\frac{k}{c_p \rho}$, which k is thermal conductivity, c_p is the specific heat capacity and ρ is the density).

The 3D heat conduction in a building or a slope is interrupted when defects (in the building envelope), or cracks/moisture appear on the surface to be inspected. These anomalies can be detected because of different thermal transfer capacities, the equation is as follows:

$$C\rho\frac{\partial T}{\partial t} = \frac{\partial}{\partial x}(k_x\frac{\partial T}{\partial x}) + \frac{\partial}{\partial y}(k_y\frac{\partial T}{\partial y}) + \frac{\partial}{\partial z}(k_z\frac{\partial T}{\partial z}) \tag{2.3}$$

which Eq. (2.3) is a general form of Eq. (2.2), where C is specific heat (J kg^{-1} K^{-1}), ρ is density (kg m^{-3}), and k_x, k_y, and k_z (W m^{-1} K^{-1}) are the anisotropic thermal conductivities of heat transfer within the material in the x, y, and z directions respectively [45] (Fig. 2.1). The maximum heat transfer in a material can be expressed by $\frac{C\rho}{k}\frac{\partial T}{\partial t}$, where k is a material-dependent constant. Therefore, the specific heat capacity, density, and thermal conductivity of the different materials such as tiles, rendering, rock types and air could be factors affecting the rate of heat transfer. Hence, time-lapse infrared thermography can be adopted in this study according to Eq. (2.3) because of the time factor ∂t.
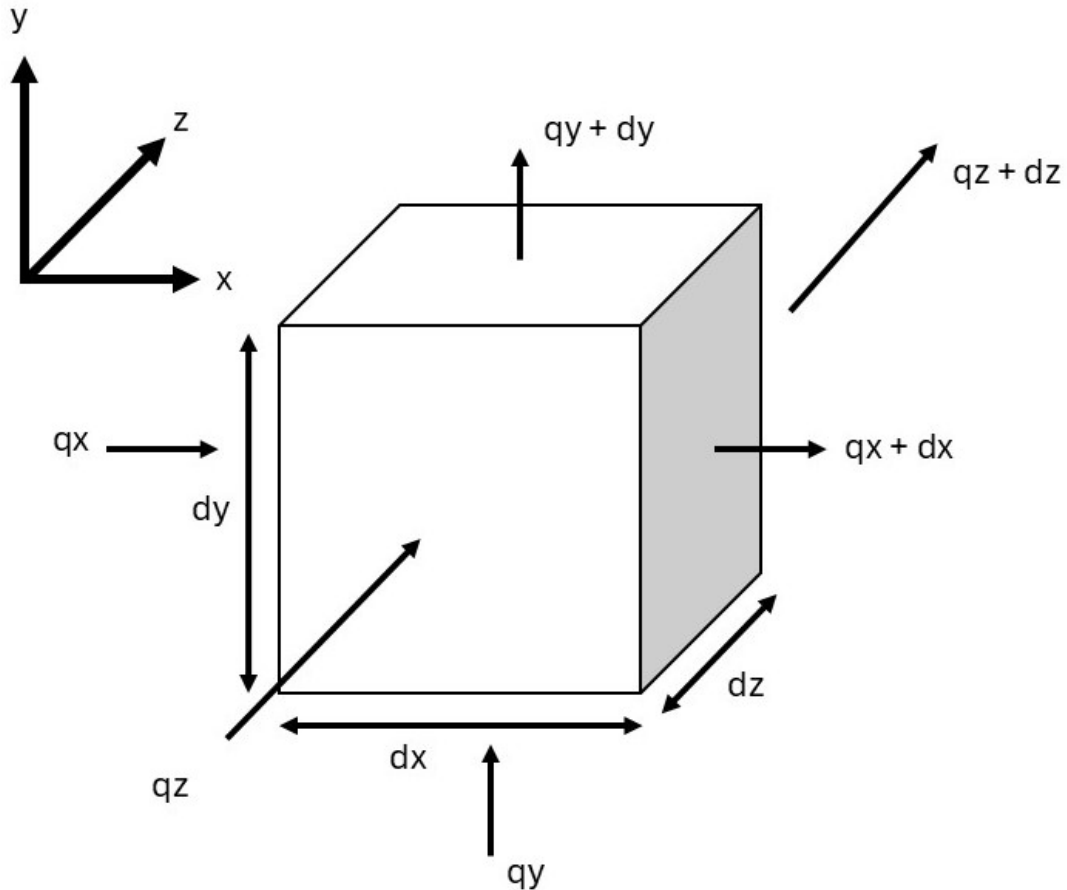
Figure 2.1: Visualisation of 3D heat conduction in a Cartesian coordinate system.

2.2.2   Convection Heat Transfer

Convection takes place when there is a mass movement of liquid or gas molecules [45]. When two solid objects are in contact with a fluid (i.e. gases or liquids), heat energy can be transferred by convection. There are two types of convection flow: forced convection (in which an external force like electrical fans creates the flow) and free convection (in which the flow is caused by an induced thermal density gradient). Newton's law of cooling states that the rate of heat loss of a body is directly proportional to the difference in the temperatures between the body and its environment (convection effect), which exists in UAS IRT surveys but not in controlled laboratory experiments because of the low wind speed in the lab compared to the field. In Eq. (2.4), the heat transfer rate q_c is related to the heat transfer coefficient h_c (which is a constant), the area A and the difference between the initial temperature T_0 and the environment temperature T_{env}.

$$q_c(t) = hA(T(t) - T_{env}) \tag{2.4}$$

or in differential form

$$-\frac{dQ}{dt} \propto \Delta T \tag{2.5}$$

$$-\frac{dQ}{dt} = k\Delta T \tag{2.6}$$

that can be deduced into Eq. (2.7):

$$T(t) = T_{env} + (T_0 - T_{env})e^{-\gamma t} \tag{2.7}$$

where γ is a decay constant and depends on the material type which is used to characterize suspected anomalies (e.g. defects in buildings, and cracks and moisture in slopes).

2.2.3   Radiation Heat Transfer

Any object with a temperature that is greater than absolute zero (i.e. 0K) emits heat energy, which can be transferred through a very large distance even in a vacuum where no conduction or convection heat transfer occurs [45]. The electromagnetic spectrum is shown in Figure 2.2.
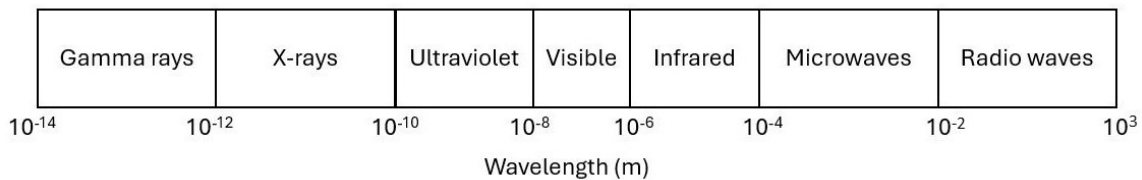
Figure 2.2: Electromagnetic spectrum.

From Figure 2.2, the radiation spectrum is divided into several regions within different wavelength ranges, including gamma rays, x-rays, ultraviolet, visible light, infrared, microwaves and radio waves. Infrared has a wavelength longer than visible light, which human eyes cannot detect wavelengths that are longer or shorter than the wavelengths of visible light (i.e. 400 to 700 nm). Heat emission by matter is further discussed in the following Section 2.3.2.

2.3 Infrared Thermography

2.3.1 Background of Infrared Thermography

The origin of Infrared technology can be traced back to 1800, when William Herschel demonstrated an experiment that validated the presence of the infrared radiation spectrum [45]. Infrared thermography (IRT) involves the measurement of the temperature of the target surface. The first thermocouple was invented by Leopold Nobili in 1829 [45], which was based on Seebeck's discovery of the thermoelectric effect in 1821 [46]. Other than temperature measurement, the first infrared image was produced by John Hershel in 1840 [45]. With the rapid development and innovations, IRT was applied in NDT since the 1960s, when evolving military technology led to the production of the first commercial infrared cameras [45].

Compared to other NDT technologies, IRT is time- and cost-effective since it can capture a large area of the target in one shot, although it is highly prone to environmental effects and the depth of investigation is only within a few centimetres. The target can be inspected from a position ranging from a few millimetres to several kilometres with the aid of the appropriate lens. Hence the temperature of potentially weakening areas on slopes and defects on building envelopes of high-rise buildings can be detected by thermal cameras. This NDT technology is adopted worldwide, and international standards are established to provide guidelines and standardized workflow for practitioners, such as ASTM D4788 on bridge inspection [47] and HKCI TM1 on building inspection [48].

2.3.2 Introduction to Thermal Transmission

Particles in oscillations emit thermal energy as the temperature of the materials causes these oscillations. As mentioned in Section 2.2.3, all matter that has a

temperature greater than absolute zero produces thermal emission and these emissions transfer energy by radiation. In this study, building envelopes and slopes are the target surfaces to be inspected, and hence this study focuses on the discussion of surface emission.

Thermal emission, as a form of radiation, can be transported without the aid of a medium. Since thermal emission can be treated as either photo emission or an electromagnetic wave with a specific frequency, it can be correlated with the equation as follows, where photonic energy W, the product of particle oscillation, is released by a given wavelength λ of the electromagnetic wave (measured in J).

$$W = \frac{hc}{\lambda} \tag{2.8}$$

Where h is the Planck constant (which is 6.626×10^{-34} J s) and c is the speed of light. The specific wavelength applied above can be calculated by the following equation from frequency f in hertz [49]:

$$\lambda = \frac{c}{f} \tag{2.9}$$

Figure 2.3 shows the infrared regions within an electromagnetic spectrum [50].
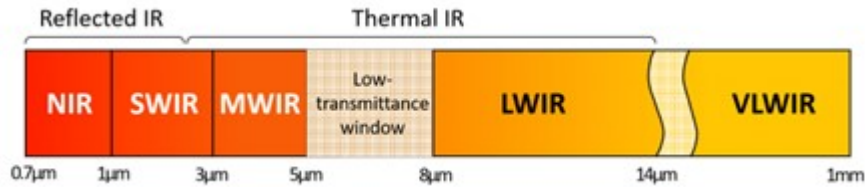
Figure 2.3: Infrared regions within an electromagnetic spectrum. [50]

Almost all surfaces on Earth emit infrared radiation in various wavelengths ranging from 700nm to 1mm, having longer wavelengths than visible light (Figure

2.3). Typically, it is defined as near-infrared (NIR) from 0.7 µm to 1 µm and short-wave infrared (SWIR) from 1 µm to 3 µm [50]. Medium-wave infrared (MWIR) is a subdivision of the IR band of the electromagnetic spectrum, which captures infrared energy in the 3 µm to 5 µm. Long-wave infrared (LWIR) is a subdivision of the IR band of the electromagnetic spectrum, which captures infrared energy in the 8 µm to 14 µm long-wave infrared (LWIR). For a superior wavelength, it is designed as Very Long Wavelength Infrared (VLWIR). LWIR is commonly used in the NDT field. The thermal camera must be calibrated and associated with a blackbody due to the non-uniformity of energy emission of many wavelengths. There are three important laws governing the physics behind thermal cameras, which are Planck's Law, Stefan-Boltzmann Law, and Wien's Displacement Law.

Planck's Law

Plank's law describes that all objects with a temperature greater than absolute zero emit radiation [51]. It describes the spectral radiance $L'_{\lambda,b}(\lambda, T)$ emitted by a blackbody at all wavelengths per unit surface and per unit of solid angle, as shown in the equation below [52]:

$$L'_{\lambda,b}(\lambda, T_b) = \frac{2hc^2}{\lambda^5 [\exp(\frac{hc}{\lambda K_B T - 1})]} \tag{2.10}$$

Where T_b is the temperature of blackbody (K), K_B = Boltzmann's constant (which is 1.381×10^{-23} (J K^{-1})) and b is the subscript of blackbody. Fig. 2.4 shows the spectral distribution of energy radiated from blackbodies of various temperatures [53], where each curve shows the radiation intensity in each wavelength band that allows the camera to convert into an image (i.e. the area under each curve). At room temperature (300K), there is sufficient energy to allow successful imaging in both MWIR and LWIR, and the intensity in LWIR is higher than in MWIR. This suggests using an LWIR camera in both building inspection and slope monitoring.
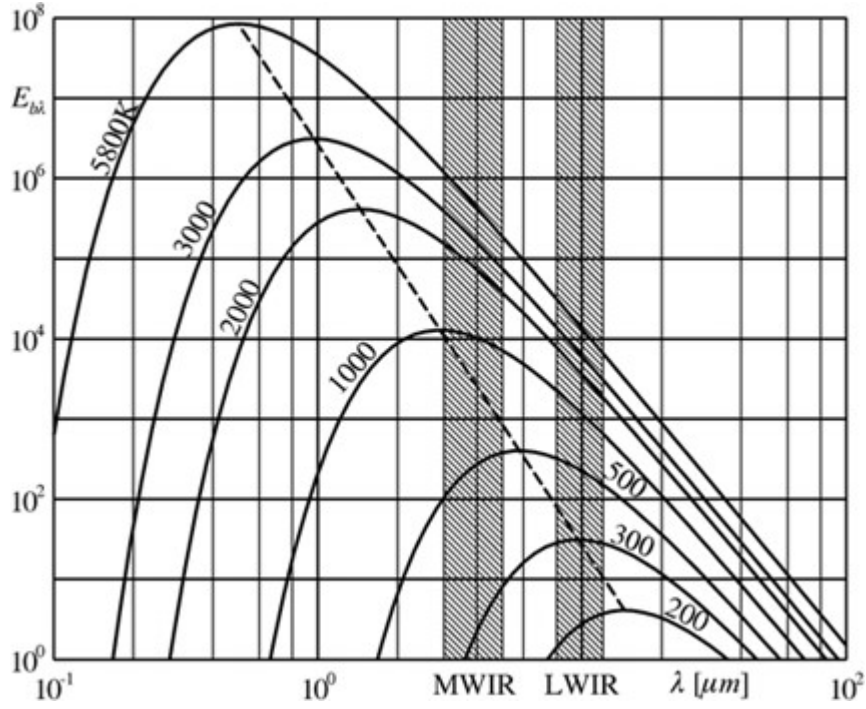
Figure 2.4: Planck's law: spectral distribution of energy radiated from blackbodies of various temperatures [53]

Stefan-Boltzmann Law

Stefan-Boltzmann Law describes that the total emission irradiated from a blackbody at all wavelengths is proportional to the blackbody's absolute temperature. The equation of Stefan-Boltzmann Law integrates Planck's law for all wavelengths ($0 < \lambda < \infty$) and is shown as follows [54]:

$$M = \varepsilon \sigma T^4 (Wm^{-2}) \tag{2.11}$$

where M is total radiant exitance from the material surface, σ is the Stefan-Boltzmann constant (which is 5.6697×10^{-8}, $Wm^{-2}K^{-4}$). The total amount of thermal radiation emitted from a real object M is a portion of thermal radiation emitted from a blackbody M_b, and is related to the emissivity ε of the material, as

shown in the equation below [54]:

$$M_b = \sigma T^4 (Wm^{-2}) \tag{2.12}$$

Wien's Displacement Law

Wien's Displacement Law states that different wavelength spectra are emitted by different objects at different temperatures, which the equation is shown below [55]:

$$\lambda_{\max} = \frac{c_3}{T} \tag{2.13}$$

Where $\lambda_{\max}$ is optimum wavelength and $c_3 = 2897.7mK$ is the third radiation constant. Eq. (2.13) shows that increasing temperature results in decreasing wavelength of the maximum radiation intensity. This relationship of maximum spectral radiance at different temperatures can provide guidance in choosing the appropriate IR camera. Room temperature (at around 25℃, i.e. 300K) emits the highest intensity of spectral radiance at the wavelength of 9 μm according to Fig. 2.4. Hence, an LWIR detector is used in this study since the temperatures of a building envelope and a slope in natural terrain, which are close to room temperature, match the wavelength in LWIR.

Absorption, Reflection and Transmission

After determining the emission behaviour of an opaque material, its spectral response when external radiation (i.e. natural sunlight in this study) reaches its surface can be illustrated in Fig. 2.5. Materials like building envelopes and slopes are opaque objects, which do not act as blackbodies. Therefore, the incoming heat flux may be absorbed, reflected and transmitted by the materials. The angles and the

spectral distributions of the incident radiation affect the amount of absorption and reflection. According to the law of energy conservation, the total sum of absorbed, reflected and transmitted heat flux equals the incoming heat flux.
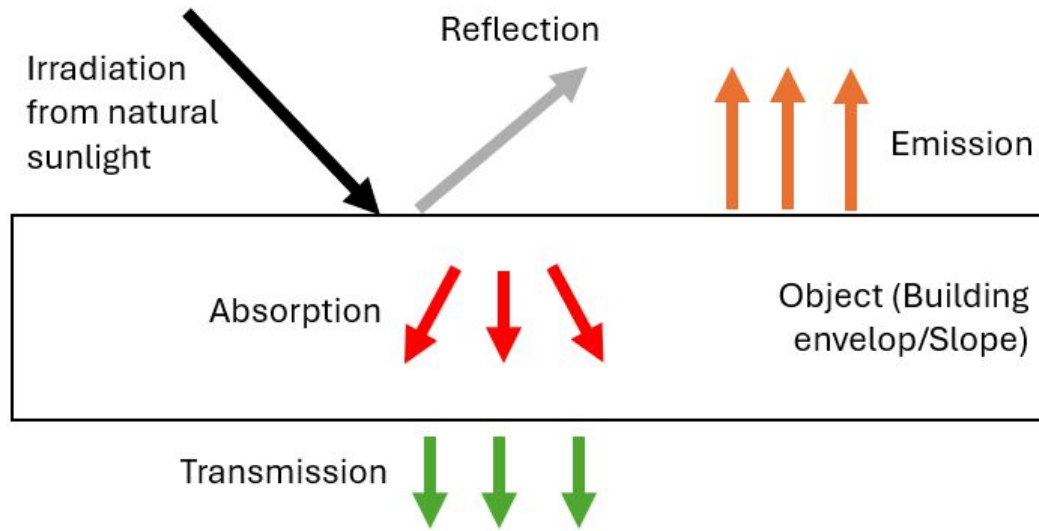
Figure 2.5: Absorption, reflection and transmission in an opaque material

Therefore, the following equation describes the relationship of absorption, reflection and transmission in photonic energy [45]:

$$a + r + \tau = 1 \qquad (2.14)$$

which a is the absorptance, r is the reflectance and τ is the transmittance. These coefficients vary when there is a difference in wavelengths of the incident radiation, properties of the materials, state of polarization, object temperature and conditions of the target surface. In this study, opaque materials like rendering and ceramic tiles in building envelopes, and rocks and vegetation in slopes, transmittance τ can be ignored. Since these opaque materials are mostly non-reflective except for windows and metal fins, when building inspection is conducted, Eq 2.14 can be simplified as follows:

$$a = 1 \tag{2.15}$$

As shown in Eq. 2.15, the key factor which affects the heat transfer inside the materials used in this study (i.e. rendering or rocks) is the absorptivity. The above equation can be simplified by Kirchhoff's law [55], as the law states that the ratio of the absorptivities for two objects equals the ratio of their radiation intensities. Hence it means that the absorptance equals the emissivity in Eq. 2.16. This indicates the importance of emissivity in radiation energy transfer.

$$a(T) = \varepsilon(T) \tag{2.16}$$

2.3.3 Thermal Properties

In the following section, thermal properties that affect defect detection in a target object are discussed, including emissivity (ε), specific heat capacity (c_p), density (ρ) and conductivity (k) in Eq. 2.1 to 2.3 in Section 2.2.

Emissivity, ε

Emissivity is a variable ranging from 0 to 1, which refers to the ratio of the total sum of energy radiated by an object at a given temperature to the total sum of energy radiated by a blackbody at the same temperature. A perfect blackbody has an emissivity value equal to 1, while opaque materials like rendering and rocks in this study have an emissivity value ranging from 0 to 1.

Specific Heat Capacity, c_p, Density, ρ and Conductivity, k

Specific heat capacity c_p is the amount of heat energy required to elevate the temperature of a material by one degree per unit mass [45], which water has one of the highest heat capacities among the materials that appeared in this study.

Density ρ measures the mass of a material per its unit volume. Specific heat capacity is the product of density and specific heat, which indicates how much thermal energy can be stored in a material. [55].

Thermal conductivity k describes the rate of energy diffusion of a material by conduction. The positive relationship between heat flux and thermal conductivity means both parameters increase at the same time with the same thermal gradient. The conductivity of gases is lower than that of liquids and solids, in which solids have the highest conductivity among the others [56].

2.3.4   Passive Infrared Thermography

Infrared thermography (IRT) is a debond evaluation method that was initially designed and developed for military [57] and aerospace sectors [58,59]. It can be used to measure electromagnetic radiation with wavelengths of between 8 and 14 µm for MWIR and LWIR radiation [54]. IRT can be divided into active and passive methods, and is a commonly used technique in building and secondary landslide hazard diagnosis. To detect anomalies in a building's exterior walls or slopes, active heat sources are needed to elevate the temperature of the walls to observe the relationship between defects and the spatial distribution of thermal decay. A passive heat source (sunlight) is preferable in building and secondary landslide hazard inspection using IRT as it can provide relatively even heat stimulation over a large area [10], although it is sensitive to environmental effects and the depth of investigation is only within a few centimetres.

2.3.5   Applications of Passive Infrared Thermography on Building Wall Finishes

After reviewing the research in the field which adopted IRT, these research were categorized into several groups, which are:

I IRT application in buildings;

II IRT application in concrete, composite or other structures;

III Application of time-lapse IRT;

IV Combination of IRT with machine learning or deep learning.

In Category I, the research on applying IRT in buildings evolved from a qualitative approach [8,60–63] to a quantitative approach [10,64–67] in recent years. Balaras and Argiriou [61] evaluated the application of IRT for building diagnostics and summarized the favourable conditions and requirements to perform an accurate building inspection using IRT, which includes the consideration of the distance between the target and the thermal camera and weather condition in the field, which the authors suggested that the thermal camera should be placed as close as possible to the target. Another research conducted by Meola et al. [63] compared IRT with ultrasonics and electric-type geophysical methods in detecting defects in architectural structures, and commented that IRT is a time-effective and user-friendly technique compared to the other two techniques, which could provide qualitative results that indicate the presence of hidden defects. Lai, Lee and Poon [10] proved the possibility of defect size estimation in external wall finishes using passive IRT, which applied a spatial pixel differentiation algorithm, a technique based on active IRT applied on composite materials, to detect the boundaries of defects. Research conducted by Anuar et al. [67] introduced the idea of a rating system for building health monitoring using IRT, in which the severity of the detected defects could be rated by their thermal contrast.

This shows the possibility of using estimated sizes from the proposed methods in this study to develop a grading system, which can present the severity of the defects detected in a quantitative approach.

Defects hidden in the building structures cause falling tiles or part of the external wall finishes, which pose a threat to the general public [8]. For defect detection of building structures in Hong Kong, visual inspection and passive thermography are widely applied to the pathology of building defect diagnosis. Lo and Choi [62] suggested that buildings should perform regular IRT surveys for better building health monitoring. Since IRT is widely accepted and used by the Buildings Department in building condition surveys (i.e. MBIS), a test method for inspecting external wall debonding/delamination by IRT was first published in 2009 by Hong Kong Concrete Institute [68]. The test method was reviewed in 2022, which requires the adjustment of the temperature span used in a single thermal image to be based on the maximum and minimum temperature of the target according [48]. However, the test method only focuses on qualitative evaluation of the subsurface defects, which means the location of the suspected defects, without providing any quantitative evaluation of the suspected defects including the sizes and depths of such defects. It is because the current practice only adopts snapshot IRT which the resulting thermal image only captures the temperature of the target at a specific timestamp, and the detectability of the suspected defects is highly affected by the environmental effects. This thesis bridges this gap by developing an automatic defect detection system using the physical approach (the time-lapse Thermal Decay Mapping method) and the statistical approach (the machine learning method), in which binary images highlighting the suspected defects can be used for defect size estimation.

In Category II, most of the researchers conducted experiments on various structures such as concrete and composite in an indoor and controlled laboratory environment using active heat sources like halogen lamps [1, 11, 69–74]. But active IRT, though useful in algorithm development, is inefficient in large-scale mapping. Passive

IRT was adopted when inspecting different large-scale structures in outdoor environments, such as bridges [75–79], facades [80] and heritages [64, 81–83]. Research conducted by Watase et al. [75] investigated the optimal time windows for an IRT survey on a concrete bridge, in which several concrete plates embedded with delamination were used in outdoor experiments in selected locations on a concrete bridge including the bridge deck top and soffit. The results showed that 12 nn is the optimal time for IRT inspection on the deck top while midnight is the optimal time for performing an IRT survey on the deck soffit. However, these suggested optimal times may vary depending on the location of the survey taking place (i.e. Northern/-Southern hemisphere). Omar, Nehdi and Zayed [77] developed an IRT data collection system, in which a vehicle was equipped with an IRT camera system to inspect the bridge deck. Thermal data collected was analysed and areas showing thermal anomalies were categorized into three warning groups, which are warning, monitoring and sound. Areas with the label "warning" represented the region with significant defects while areas with the label "monitoring" represented the region starting to deteriorate and needed regular monitoring. Another research on defect segmentation on bridge decks utilized deep learning methods on the thermal images collected by a UAS system [79], which could provide automated defect detection. However, since it was an image-based detection using deep learning, selecting appropriate image augmentation strategies was necessary to ensure the accuracy of the prediction model. The above research showed successful application of passive IRT in various structures, and such application could lead to the development of automatic defect detection. However, the specimens and samples used in these research were mostly homogeneous materials only, while the targets such as building external walls in this study involved multiple-layered materials on the same surface. The severity rating system proposed in [77] showed the potential of implementing a similar system in building inspection.

Research adopting time-lapse IRT are categorized in Category III, which includes studies on thermal behaviours of building envelopes [84, 85], detection of

cracks [86] and defects in buildings and infrastructures [87–89]. A study on the sensible heat flux of a building was conducted by Hoyano, Asano and Kanamaru [84], using thermal data collected at one-minute intervals within 24 hours. Time-lapse IRT survey was performed in both outdoor and indoor environments in [85] to detect buildings' defects, which suggested that time-lapse IRT could be utilized for better observation of the evolution of heat loss of the target because the thermal decay rates at the defective and intact area are different according to Eq. 2.3. Bauer et al. [86] performed an experiment involving crack detection using time-lapse thermography, and suggested that the optimal time for thermal inspection of the facade is in the morning session, when the thermal contrast between the defective area and intact area is the largest. With the aid of image processing techniques, the edges of the detected defects could be identified by applying the active contour method on time-lapse thermal data [87]. Rakha et al. [88] conducted a time-lapse IRT survey with the use of a UAS, and the results showed that time-lapse thermal data could be used in forming photogrammetry models, which facilitates thermal anomaly detection at different times of the day. Although the current practice adopting snapshot IRT allows defect detection in a single thermal image, an exact optimal time for capturing a thermal image allowing the highest accuracy of defect detection cannot be determined since temperatures of the target surface keep changing in time and the orientation of the target affects the amount of irradiation absorbed on the target surface. Hence, time-lapse IRT is adopted in this study, albeit its long observation time compared to snapshot IRT imaging, to observe the whole heat dissipation period of the target (i.e. building envelopes).

With the development of Artificial Intelligence (AI), many research in the field started to combine IRT with machine learning or deep learning (Category IV), which include inspection on bridges [77, 90–92], photovoltaic (PV) module [93, 94], composite materials [19, 73, 95], buildings [21, 96–99] and dam [14], and material classification [100]. Park et al. [96] performed an image-based segmentation using a

Convolutional Neural Network (CNN) on a building envelope, which could separate walls and windows. Then thresholding was applied to the segmented thermal image for thermal anomaly detection. Kim et al. [98] further developed the method in [96], and utilized the segmentation results for feature classification. Another research performed similar image segmentation on thermal images of building external walls, in which the segmentation process was firstly applied on corresponding visual images (that were registered with thermal images beforehand), and then applied to thermal images using the same parameters [97]. Object detector RetinaNet was then used to detect windows and defects on the segmented images. However, the above research mainly performed image-based deep learning, which used the whole thermal images as a single data point. This has a limitation which the user-defined temperature span and colour palette used in the thermal image could affect the accuracy of the learning process. In this study, the temperature value in each pixel of a thermal image was treated as individual data points, which eliminated the human bias involved in the selection of the temperature span and colour palette. After reviewing the related studies above, there is a research gap in the field in which research on adopting time-lapse IRT surveys and machine learning in defect detection and classification are rather limited. Hence, this study adopted a time-lapse IRT survey to perform inspection on building envelopes, and attempted feature classification and size estimation in two approaches, which are the physical approach (the Thermal Decay Mapping method) (which is further developed from [101]) in Chapter 4, and the statistical approach (the machine learning method) (which is further developed from [102]) in Chapter 6.

2.3.6 Applications of Passive Infrared Thermography by UAS on Rock Slope Features

If building inspection is regarded as difficult because of its height in nature, and its danger for human access, the inspection of landslides in natural terrain can

further be thought to be even more difficult because of its rural remoteness. Recent studies on geotechnical surveys using IRT can be summarized into three main categories, including detecting anomalies on slopes, evaluating rock characteristics and properties, and combining IRT slope surveys with other remote sensing technologies. The proposed Thermal Decay Mapping method in this study is the first local and one of the very few international studies on geotechnical surveys using IRT [44].

For anomaly detection on slopes, implementing IRT into geotechnical surveys was investigated by several researchers, which utilized the observation of thermal contrast between fracturing areas and intact areas. Cases involved in these research included eroded caves [29], surface weaknesses [30], open fractures and cracks [31, 32, 38, 40, 103–105], water seepage [32] and old landslide bodies [33]. Wu et al. [29] utilized snapshot and ground-based IRT to identify eroded caves hidden in a shotcreted slope, where thermal anomalies shown in thermal images due to thermal contrast between voids and the intact area were identified, and GPR was used to validate the results. Other than locating eroded caves, the same approach was adopted in [31] to identify open fractures and cracks in cliffs and rockslides. Another research [30] showed the potential of using thermal data in the cooling phase to locate weaknesses on a rock cliff, in which the thermal data of a rock cliff was collected by a ground-based IRT survey. Combining with point cloud data, Casagli et al. [106] proved the possibility of forming a 3D landslide map using ground-based IRT, which results could be used for emergency management as anomalies such as cracks and moisture can be located on the 3D landslide map. Based on the difference in thermal contrast, anomalies on slopes can be identified using IRT. These research proved that regions showing abnormal temperature distribution (usually high temperature contrast) indicate the presence of open fractures or eroded caves as the presence of air inside has different thermal properties when compared to the intact area. Despite its usefulness in identifying thermal anomalies on rock slopes, a ground-based IRT survey has a limitation that requires the site to be accessible, which is unfavourable

in monitoring remote landslides.

Using IRT to perform evaluation on rock physical and mechanical properties is another popular topic in the field, which includes research on ratio of radiance [34], rock types and its corresponding properties [35, 107], thermal properties including conductivities and emissivities of different rock types [36, 108] and the factors affecting the cooling rate of rocks such as porosity [37, 43, 109–111], and the status of fracturing [108]. These studies utilized the advantages of IRT to analyse both the physical and mechanical properties of different rocks. Results from these research suggested that there are several factors which could affect the thermal contrast shown in thermal images, including the chemical properties of different compositions in rocks, water content in rocks, and the porosity of the rocks. This showed the potential of adopting IRT in rock-type classification. However, getting rock samples from the target slopes for further experiments could be hard when access to the sources is impossible. Furthermore, the data analysis for rock-type classification required extensive knowledge of physics and chemistry, and a long processing time. This study adopted the Thermal Decay Mapping method, which was inspired by the research conducted in [43]. Their research proposed an index called the "Cooling Rate Index", which considered the elapsed time when performing rock mass analysis. However, their research adopted ground-based IRT only. In this study, time-lapse IRT was adopted and a case study was presented in which thermal data were collected by a UAS equipped with a thermal camera.

IRT could be combined with other inspection technologies for assessing rock slopes, which research showed successful combination, including unmanned aerial vehicle (UAS) [112–115], seismic survey [38], photogrammetry [41], laser scanning [39], and rebound hammer test [42]. With the aid of other remote sensing technologies, IRT could be used to perform remote slope monitoring and rock assessment. Combining with UAS, thermal data could be collected remotely and used in numerous aspects, including monitoring the degree of erosion in a river embankment [113], detecting

the state of weathering in tuff cliffs [112], and evaluating rock mass in a qualitative approach [114]. However, the UAS data and thermal data were collected separately in these studies, which did not fully address the potential of combining IRT with UAS. Vivaldi et al. [115] demonstrated a landslide remote monitoring which fully utilized the combination of UAS and IRT, in which snapshot IRT was adopted for monitoring the whole area where a landslide occurred. Features that are normally difficult to distinguish in visual data could be identified with the aid of IRT, including the crown and head of the landslide scar, moisture in wet terrain and man-made objects such as grooves and pile walls. However, research combining time-lapse IRT and UAS for monitoring slopes or landslides are limited in the research field, which is only mentioned in [42, 116], which emphasizes considering the "time" factor in the analysis.

Tables 2.1 to 2.3 summarize the important findings in the related literature in four main categories, mentioned in the above paragraphs. After reviewing the above-related studies, there is a research gap in the field in which research on time-lapse IRT surveys using a UAS are rather limited. Hence, this study adopted a time-lapse IRT survey using a UAS to perform slope assessment, and attempted feature classification and size estimation in two approaches, which are the physical approach (the Thermal Decay Mapping method) (which is further developed from [101]), and the statistical approach (the machine learning method).

Table 2.1: Summary of Literature of IRT Application on Detection of Failures and Abnormalities on Rock Slopes.

Author(s) & Year	Main Focus	Main Findings/Outcome/Discussions	Season	Site(s) of Case Studies
Wu et al. [29]	Eroded caves behind shotcreted slopes	• IRT matched with visual inspection, tapping test and GPR survey • High temperature contrast indicated the presence of eroded caves in fine-grained sandstone and shale	Spring	Taiwan
Teza et al. [30]	Surface and shallow weakness of rock cliff	• IRT-based analysis could allow contactless recognition on thermal anomalies • Provide information on stability of the protruding elements	Spring	Italy
Baron et al. [31]	Open fractures in rockslides and cliffs	• IRT could be used for locating open cracks • Temperature contrast increases when the length depth of the cracks increases	Winter	Czech Republic, Austria
Frodella et al. [32]	Multi-temporal survey (24h cycle) for 2D and 3D landslide and cracks mapping characterisation mapping characterisation and detection of water seepage	• Low temperature was related to the water seepage • High differential temperature between different day times was associated with unstable volumes - possible landslide • Summer is the best season to observe temperature contrasts	Spring, Summer, Winter	Italy
Pappalardo et al. [33]	Study on surveyed land-slides from risk management aspect and integration of IRT and DInSAR	• IRT could be used to map key morphological elements due to thermal contrast • Identify old landslide bodies which are no longer visible to field inspections.	N/A	Italy
Mineo et al. [103]	Evaluation of the degree of fracturing in bare rock masses	• Highest temperatures are related only to the fractured/hollow portions • Water influence images taken late in the evening are considered the most reliable	Sunny day during dry season (3 times day)	Italy
Pappalardo & Mineo [104]	Cooling Rate Index (CRI), useful for the evaluation of the jointing condition of the rock	• Highest temperatures were observed in the bare, fractured rock	Summer, Winter	Italy
Junique et al. [105]	Study on irreversible cracking threshold of rocks using IRT	• Chalk and weathered granite were less susceptible to thermal contrast than a fresh granite and sandstone • IRT could be a very useful tool to detect changes on rock surface	N/A	Lab/France
Settle [117]	Several types of rocks	• Instrumentation • Physical properties • Theory of thermal surveys and observation • Emissivity, atmospheric and planetary studies	N/A	USA
Michalski et al. [118]	Thermal infrared analysis of weathered granitic rocks with Satellite IR Images	• Deconvolution of the spectra allowed producing maps of quartz, clay and feldspar • Identify weathered granitic rocks	N/A	USA/Mars

31

Table 2.2: Summary of Literature of IRT Application on Evaluation of Rock Characteristics and Properties.

Author(s) & Year	Main Focus	Main Findings/Outcome/Discussions	Season	Site(s) of Case Studies
Vincent & Thomson [34]	Comparison of the theory with experimental ratio of radiance over two bands over 25 silicate rocks for rock mapping	• Gross rock-type discrimination using ratios of radiance for crude geologic mapping of inaccessible geological terrain, both terrestrial and extra-terrestrial by using two or three channels with different ranges at 1000m altitude	N/A	USA
Christensen et al. [35]	Thermal infrared spectra of different materials for comparison to spectra obtained from planetary and Earth-orbiting spacecraft and laboratory measurements	• Creation of library of thermal infrared spectra, including silicate, carbonate, sulphate, phosphate, halide and oxide minerals	N/A	USA/ Mars
Roshankhah [36]	Comprehensive PhD thesis about, not limited to, both thermal emissivity, conductivity and effective stress on different geological materials	• The higher the quartz content of a rock, the higher the thermal conductivity • The thermal conductivity of rocks with fractured or open structure is higher and increases with temperature • Water saturation enhances thermal conductivity	N/A	Lab/ USA
Mineo & Pappalardo [37]	Study on rock porosity by using IRT	• Cooling rate is influenced by voids in rocks, which voids could act as leakage of heat • Possible to estimate total porosity in a 10-min IRT survey	N/A	Italy
Feely & Christensen [107]	Evaluation of rock properties from IR spectroscopy	• Infrared emission spectra collected from large rock samples can be successfully deconvolved to determine the quantitative mineral composition	N/A	USA
Mineo & Pappalardo [108]	Distinction between minerals in the granite based on temperature decay	• Higher emissivity is related with high porosity, dark colour minerals and irregular surface • Emitters range between 0.89 and 1 • Per rock type, per order, sedimentary (high values), metamorphic and igneous, the emissivity range is higher, respectively	N/A	Lab Italy
Pappalardo & Mineo [109]	Study on mechanical properties on basaltic rocks using IRT	• Persistence of vesicles in basaltic rocks can be related to the stronger thermal intensity	N/A	Lab/ Italy
Pappalardo [110]	Evaluation on hydraulic conductivity of rock masses by IRT	• Proposed a non-destructive methodology for assessing hydraulic conductivity • The greater the permeability, the faster the rock mass	Summer, Winter	Italy
Mineo & Pappalardo [111]	Indirect porosity estimation of intact rock specimens using IRT	For basalts: • IRT could be used to characterize the persistence of vesicles • The greatest persistence, the highest the surface temperature of the void For microporous rocks: • IRT could show the occurrence of mechanical cracks • Presence of shallow fossils could be highlighted	N/A	Lab/ Italy
Pappalardo et al. [43]	Study on estimation of cooling rate index of rock masses using IRT	• Rock mass gains heat as long as it is exposed to sunlight • The best IRT output is recorded in night-time • High intensity thermal anomalies could reflect the presence of fractures • Cooling rate indexes of rock masses are directly proportional to the degree of fracturing	Dry and cold season	Italy

Table 2.3: Summary of Literature of IRT Application With Other Technologies.

Author(s) & Year	Main Focus	Main Findings/Outcome/Discussions	Season	Site(s) of Case Studies
Mineo et al. [38]	Study on unstable rock slope combining IRT with geostructural and seismic survey	• Essential to combine different survey technologies to perform a detailed assessment of a slope stability problem • IRT shows the potential to detect source areas for future rockfalls	Dry season	Italy
Guerin et al. [39]	Integrated terrestrial laser scanning (TLS) and IRT techniques to monitor daily deformations of two granitic exfoliating cliffs	• Exfoliated sheet occur where the tem-perature variations are the highest and crack apertures are the largest	Autumn	Yosemite Valley/ USA
Frodella et al. [40]	Analysis on landslide types and processes, combined with TLS and UAS	• IRT revealed thermal anomalies potentially connected to erosion, weathering and instability • Could be used to define preliminary landslide and erosional process esses in sites	Summer, Winter	USA
Grechi et al. [41]	Monitoring of jointed rock mass-with IRT and photogrammetry	• IRT combining with photogrammetry could produce a 3D thermal point clouds • Could be a useful tool to better under-standing of the existing relationships between continuous temperature fluctuations and geomechanical and geo-morphological conditions of jointed rock masses	All year	Italy
Loche et al. [42]	Evaluation on rock compressive strength with time-lapsed IRT and re-bound hammer	• 24-hr time lapse IRT survey on the sample rock blocks was conducted • First five hours of cooling are the most informative time interval for regression analysis • Help in rock and fracture classifications • IRT could also be combined with UAS to characterize the strength of unreachable blocks	Summer	Italy

2.3.7 Limitations of Infrared Thermography

Numerous successful applications of IRT were shown in the previous sections (Section 2.3.5 and 2.3.6), with its advantages of contactless, non-destructive nature and time-effectiveness. However, when adopting IRT in building and slope inspection, there are several limitations discussed in the literature, which are instrumental, environmental and material limitations. The study mainly focuses on the material limitation. Firstly, the characteristics of the materials on the surface including their colours, sizes and textures affect the thermal contrast between the defects and intact area [119–121]. Bansal, Garg and Kothari [119] investigated the effects of different external surface colours of a building, and the results showed that the temperature difference between dark colours and light colours could reach a maximum of 7 ℃during

the heat absorption period.

Secondly, since building or secondary landslide hazard inspection occurs in an outdoor environment, weather conditions on site must always be taken into consideration, since thermal response on the target surface could be affected by various environmental factors such as cloud cover, moisture, and wind [54, 58, 61, 62, 121]. Research conducted by Moropoulou et al. [58] suggested passive IRT inspection in an outdoor environment should be performed in weather with insignificant or no cloud cover, which could ensure sufficient energy transfer from the sunlight to the target.

Thirdly, the resolution of a thermal image (i.e. 640×480 in this study) is not as high as the resolution of a visual image. With this limitation, the distance between the target and the camera should be as close as possible. As each pixel in a thermal image represents a specific area of the target surface, increasing distance between the target and the camera means each pixel represents a larger surface area, and hence loses details because the radiation from that specific area is averaged [61].

Finally, the orientation of the target surface also affects the results of the IRT survey on building and slope [121, 122]. Results from the study in [122] showed that north- and east-facing walls appeared warmer than the west-facing walls in the morning, while the west-facing walls appeared warmer than north- and east-facing walls. This diurnal phenomenon happened because of the solar radiation received at different times and the difference in the angle of solar incidence.

This research investigates the material limitations when adopting the IRT survey in building and secondary landslide hazard inspection, including experiments and field studies of the targets consisting of commonly used wall finish materials and features of natural terrain slope, and suggestions for minimizing the effects of material properties are made based on the results and findings in this study.

2.4 Physical Approach - Thermal Decay Mapping

Based on Eq. (2.7) in Section 2.2.2, γ in the equation of convection heat transfer can be utilized in feature classification because it is a constant which varies according to the material type (i.e. defect in buildings; crack, moisture, vegetation and rock in slopes). The γ value of each pixel in thermal images with different time stamps $\gamma(x, y, t)$ was calculated and normalized in a natural logarithmic base. The retrieved thermal decay gradient was used to replace the original temperature values in the raw thermal images and form a thermal decay map [101]. Research conducted by Pappalardo et al. [43], as mentioned in Section 2.3.6, proposed a similar idea called "Cooling Rate Index" in rock slope monitoring which presented the indexes in selected points only. For building inspection, time-lapse IRT is seldom adopted due to the feasibility of setting a fixed station in the field for a long period of data collection. Hence, the research on the application of thermal decay mapping in building envelopes is in vain. This study performed the calculation in every pixel of a thermal image and formed a Thermal Decay Map based on the calculated thermal decay gradient, and was one of the first attempts of its kind in time-lapse IRT with UAS. Then, thresholding was applied to the resulting thermal decay map for size estimation, which is discussed in the following section.

2.4.1 Thresholding

Thresholding is an image processing technique used to segment the image into homogeneous regions that sort parts of the image containing similar types. This image processing technique is commonly used in different aspects, such as image recognition and machine learning [123]. A threshold value is assigned and used to define each pixel in an image, separating all pixels according to their values into foreground and background. The foreground consists of the pixels with values within the selected range, while the background consists of the pixels with values outside the selected

range. The threshold value could be determined manually or by calculations with
assigned algorithms.

The threshold value (T_h) can be presented in the following equation:

$$T_h = T_h[x, y, p(x, y), f(x, y)] \tag{2.17}$$

where x, y presents the pixel coordinates, $p(x, y)$ represents the local properties
of the pixel (i.e. the intensity level of the neighbour pixel), and $f(x, y)$ represents the
intensity or grey level of the pixel.

To generate a thresholded image, the selected threshold value according to Eq.
2.17 would be applied to the raw image. When the pixel value (x, y) is smaller than
the threshold value T_h, it will be defined as the background (in black). When the
pixel value is equal to or greater than the threshold value T_h, it will be defined as the
foreground (in white).

Since threshold values can be calculated by various algorithms, this study fo-
cused on the application of global thresholding and Adaptive Thresholding on defect
size estimation from the resulting thermal decay map. Global thresholding selects
the threshold value by considering the histogram of the whole image, which works
optimally when the histogram is bimodal. A bimodal histogram contains two peaks
in the histogram, which one is from the object of interest and one is from the back-
ground. These two peaks can be separated by a significant threshold value [124].
The global threshold value can be calculated by several approaches, including the
identification of valleys in the histogram of a greyscale image [125], the calculation
of the median greyscale intensity of the histogram [126], and selecting the threshold
value that allows between-class variance maximization [127]. This study adopted the
thresholding method proposed in [127]. This paper followed the research in [128] to
evaluate whether adding standard deviations (SD) of all the pixel values with the

maxima improves the performance of defect size estimation in the Thermal Decay Mapping method.

Another thresholding used in this study is called adaptive thresholding, which selects the threshold value automatically based on the spatial variations of the entire image. This type of thresholding could solve the problem caused by insufficient and uneven illumination [129]. There are three common approaches in this type of thresholding, which are modelling the background of the image, splitting the entire image into small parts and processing them individually, and determining the threshold value for each pixel based on the grey level of the neighbouring pixels (i.e. local thresholding method). This study used the last approach, which utilizes the mean of the neighbour pixel's local intensity of each pixel. This approach can provide satisfactory results with a comparatively smaller computational load for the analysing machine [129].

2.4.2 Conversion of Pixel Values

For secondary landslide hazard inspection, UAS was used in data collection in the natural terrain part of this thesis. Although the flight path of the UAS was designed and controlled by the use of GPS signals, the GPS signals received on site were unstable because of the varying positions of the UAS to the satellite in each flight for generating time-lapse Thermal Decay Maps. This resulted in shifts in the positions of the UAS, and therefore the thermal images collected by the UAS needed to be geo-registered and corrected to ensure consistent alignments of these thermal images. After the image registration, the pixel values of the exported thermal images were in 8-bit greyscale as no radiometric JPEG is available in our system, a conversion was needed to convert the pixel values back to pixel values in degrees Celsius. There are three approaches to performing the conversion, which are the Maximum-minimum method, the Interquartile Range (IQR) method and the Standard Deviation (SD)

method [101].

Maximum-minimum method

The maximum-minimum method is an objective method which includes all the pixel values from the original images with no selection rule, therefore it might include outlier values in the original image. The conversion formula is shown as follows:

$$Temperature = T_{Min} + \frac{T_{Max} - T_{Min}}{255} \times (PixelValue) \qquad (2.18)$$

where T_{Min} is the minimum temperature value (in ℃) in the original thermal image before image processing, T_{Max} is the maximum temperature value (in ℃) in the original thermal image before image processing, and $PixelValue$ is the stretched pixel value from the exported registered thermal images in 256 scale, since the exported thermal images were in 8-bit greyscale.

Interquartile Range (IQR) method

In the interquartile range (IQR) method, the temperature values at the 1st quartile (25%) and the 3rd quartile (75%) were used for the conversion of the pixel values. This method tried to omit the outliers in the original thermal images to determine a more reasonable range for the pixel conversion. The conversion formula is shown as follows:

$$Temperature = 25\%T + \frac{75\%T - 25\%T}{255} \times (PixelValue) \qquad (2.19)$$

where $25\%T$ is the temperature value (in ℃) at the 1st quartile in the original thermal image before image processing, $75\%T$ is the temperature value (in ℃) at the

3rd quartile in the original thermal image before image processing, and $PixelValue$ is the stretched pixel value from the exported registered thermal images in 256 scale.

Standard Deviation method

The standard deviation (SD) method is a commonly used method in research involving image processing [30, 130]. Outliers were omitted in this method, and a range for pixel conversion was selected based on the standard deviation of the original images. The conversion formula is shown as follows:

$$\text{Temperature} = (T_{Mean} - \sigma_{SD}) + \frac{(T_{Mean} + \sigma_{SD}) - (T_{Mean} - \sigma_{SD})}{255} \times (\text{Pixel Value})$$

(2.20)

where T_{Mean} represents the mean temperature value in the original thermal image before image processing, σ_{SD} represents the SD of the temperature value of the original thermal image before image processing, and $PixelValue$ represents the stretched pixel value from the exported registered thermal images in 256 scale.

The standard deviation (SD) method was used in the conversion in this study, as the research in [101] suggested that this method could provide a thermal decay map with the best contrast of the features among the others.

2.5 Statistical Approach - Machine Learning

2.5.1 Background of Machine Learning

Machine learning is a popular research topic in the field, which can handle enormous and troublesome datasets simultaneously. For detecting defects on building envelopes and slopes, different attributes such as thermal contrast between the

defect area and intact area can be utilized for machine training. Many classification algorithms can be used in machine learning. The advantage of these classification models is that they offer user-friendly optimization and generalization when training with new data. With the aid of machine learning, thermal anomalies appearing on thermal images can be detected automatically without human bias, which is the current demerit of qualitative thermal analysis in the field. As mentioned in Section 2.3.5, the current trend in the research field focuses on image-based defect analysis adopting deep learning, which can be affected by the preparation of the raw thermal images (i.e. selecting appropriate temperature span and colour palette). The second approach of this study is to adopt machine learning in thermal data analysis, which utilizes the temperature values stored in every pixel of a thermal image and the time variable in a time-lapse IRT survey, instead of processing in an image-based approach.

There are different types of machine learning, which include unsupervised machine learning and supervised machine learning (Fig. 2.6). Unsupervised machine learning instructs the machine to perform pattern recognition in the input data without prior knowledge like groups or classes, while supervised machine learning focuses on the prediction of the labelled data which each data point is labelled with a class label. [131]. In this study, supervised machine learning is selected as thermal data analysis involves many uncertainties such as weather conditions and emissivities of the materials, and the number of datasets is insufficient for adopting unsupervised machine learning. Classification is performed for the sake of diagnosis of different states of materials.

2.5.2   Logistic Regression (LR)

Logistic regression is one of the classification algorithms in supervised machine learning, and it is commonly used in solving binary classification problems [132]. In this study, logistic regression is adopted since there are only two possible outcomes
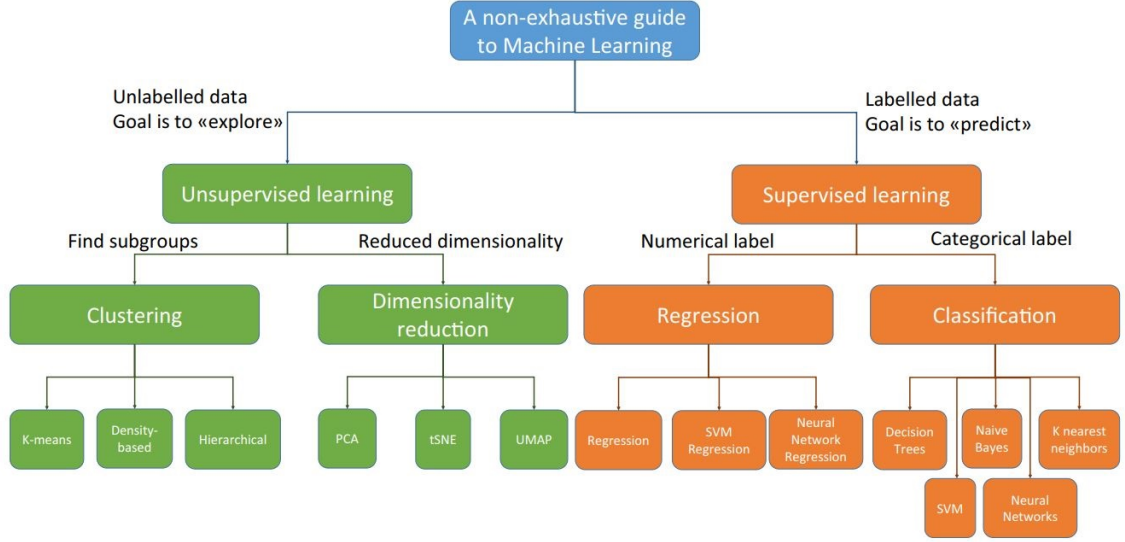
Figure 2.6: An overview of different machine learning algorithms. [131]

in defect detection, which are defects and intact areas in building envelopes. In the training dataset, defects are labelled as 1 and intact areas are labelled as 0. For detection in natural terrain, several features such as vegetation and rocks are selected and labelled for constructing the training dataset, which the details are summarized in Chapter 6. As logistic regression is modified from linear regression, the sigmoid function is applied to ensure the prediction lies between 0 and 1 (Eq. 2.21).

$$P = \frac{1}{1 + e^{-y_h}} \tag{2.21}$$

where P represents the probability of successful prediction and y_h is the hypothesis function.

Supervised machine learning is adopted in this study, as the detection of thermal anomalies on buildings and slopes cannot be judged simply by the temperature values and performed by the naked eye. Supervised machine learning for feature classification in building envelopes and slopes is hence preferred over unsupervised machine learning, in which the data in the training dataset is labelled according to

the ground truths.

2.5.3   Optimisation and Accuracy

Feature Scaling

Feature scaling, which is a technique used in data preprocessing, is used to normalize the values of variables or features in a dataset to the same scale, and it is an important component which ensures the application of machine learning effectively [133]. Three commonly used rescaling methods are introduced in the following section, which are the min-max scaler, standard scaler and robust scaler.

Min-max normalisation, which is presented in Eq. 2.22, is a straightforward and commonly used algorithm for feature rescaling [134]. This algorithm based on a given range, which is normally determined by the maximum and minimum value in the feature set, transforms each variable or feature so that these values are set between 0 and 1.

$$x_{scaled} = \frac{x_i - min(x)}{max(x) - min(x)} \tag{2.22}$$

This rescaling method has one disadvantage which is affected by the effect of outliers, however this rescaling method could scale down these outliers linearly into a fixed range.

Another rescaling method is called the standard scaler, which calculates the standard score (i.e. z-score) of the training set [135] (presented in Eq. 2.23). This rescaling method is suitable when the data in the training set is normally distributed.

$$x_{scaled} = \frac{x_i - mean(x)}{SD(x)} \tag{2.23}$$

where SD stands for standard deviation.

Robust scaler, which is named "robust" as it is robust to outliers by using statistics, based on the quantile range (i.e. Interquartile Range (IQR)) to rescale the data after removing the median (presented in Eq. 2.24) [136]. Such IQR is a range between 1st quartile (Q_1) and 3rd quartile (Q_3).

$$x_{scaled} = \frac{x_i - Q_1(x)}{Q_3(x) - Q_1(x)} \tag{2.24}$$

Regularisation

Overfitting can be troublesome in model training in case the hypothesis function becomes too complex when attempting to achieve a lower training error. To avoid overfitting in the training model, regularisation is applied. Two regularisation techniques called the Lasso and Ridge regularisation are presented in Eq. 2.25 and 2.26 respectively [137]. These two regularisation techniques make use of the L1 and L2 norms respectively. The L1 norm, which is known as the Taxicab distance, is the sum of the rectified coordinates of a vector. The L2 norm (i.e. the Euclidean distance) is the shortest distance between two vectors.

$$Cost = \sum_{i=0}^{N} (y_{oi} - \sum_{j=0}^{M_o} x_{oij} W_{oj})^2 + \lambda_o \sum_{j=0}^{M_o} |W_{oj}| \tag{2.25}$$

$$Cost = \sum_{i=0}^{N} (y_{oi} - \sum_{j=0}^{M_o} x_{oij} W_{oj})^2 + \lambda_o \sum_{j=0}^{M_o} W_{oj}^2 \tag{2.26}$$

where y_o represents the predicted outcome, x_o represents the actual outcome, M_o represents the total number of instance or sample, N represents the number of coefficients, W_o represents the weight and λ_o represents the strength of regularisation.

In the first half of Eq. 2.25 and 2.26, these two regularisation techniques share the same cost function. However, the regularisation terms (i.e. the norm for penalisation) of these two techniques are different (the second half of Eq. 2.25 and 2.26). The characteristics of the two techniques are the cause of this difference.

Since the norm is an absolute value of the weight parameter, the cost increases linearly when the L1 norm is applied. However, because of the nature of absolute value, a closed-form solution is unavailable which makes regularisation applying the L1 norm more computationally expensive. The automatic feature selection in the dataset with high dimensions is the key advantage of adopting absolute value, as regularisation using the L1 norm can diminish those coefficients of the less important features (i.e. sparse features which are mostly zero values) to zero.

Since the norm is a squared value of the weight parameter, the cost linearly increases exponentially when the L2 norm is applied. This regularisation has a closed-form solution as the norm is a squared value, which means the regularisation is less computationally expensive, and hence cannot diminish sparse features to zero.

Minimisation of the Cost/Loss Function

For determining the parameters of the hypothesis with minimum errors for prediction, minimising the quadratic/cost function can be carried out through gradient descent, which is presented in Eq. 2.27 [138]. The cost refers to the error between the predicted and actual outcomes. The global minima (i.e. the least error) are searched by the gradient descent algorithm, which iterates at a user-defined learning rate. Since there are different solvers, during the selection of suitable solvers, one should consider the size of the dataset, the number of output labels, and the computational complexity.

$$x^{k+1} = x^{(k)} - \alpha_k \bigtriangledown f(x^{(k)}) \tag{2.27}$$

where α_k is the learning rate or step size, $x^{(k)}$ is the initial starting value of the parameter in the hypothesis, and $\bigtriangledown f(x^{(k)})$ is the gradient, or the partial differentiation of the cost function.

K-fold Cross-Validation

Cross-validation can be used to evaluate the ability of a classifier on unseen data, which a standard approach is using a technique called stratified k-fold cross-validation [132]. The standard approach involves dividing the dataset into several folds, and each fold will take turns to become the test set. The rest groups (i.e. k-1) serve as the training set. The whole dataset will be cross-validated for k times. This approach allows efficient use of limited data. The nature of the datasets determined the values of k, which range from 5 to 10 [139]. Calculation of the training and cross-validation accuracy is performed in each fold of validation.

Cross-validation should be carried out if new training data is added or if there are changes in the parameters of the classifier. To optimise the parameters of the classifier, a bias-variance decomposition of the classifier can be performed, which is explained in the next section.

Bias-Variance Decomposition

Real-world cases are full of uncertainties, and hence errors are always present in a model. When the prediction model has a high bias, this will result in poor performance in application to unseen data. The best fit can be determined by bias-variance decomposition [140]. This method chooses an appropriate degree of complexity for the model which has the smallest bias and variance.
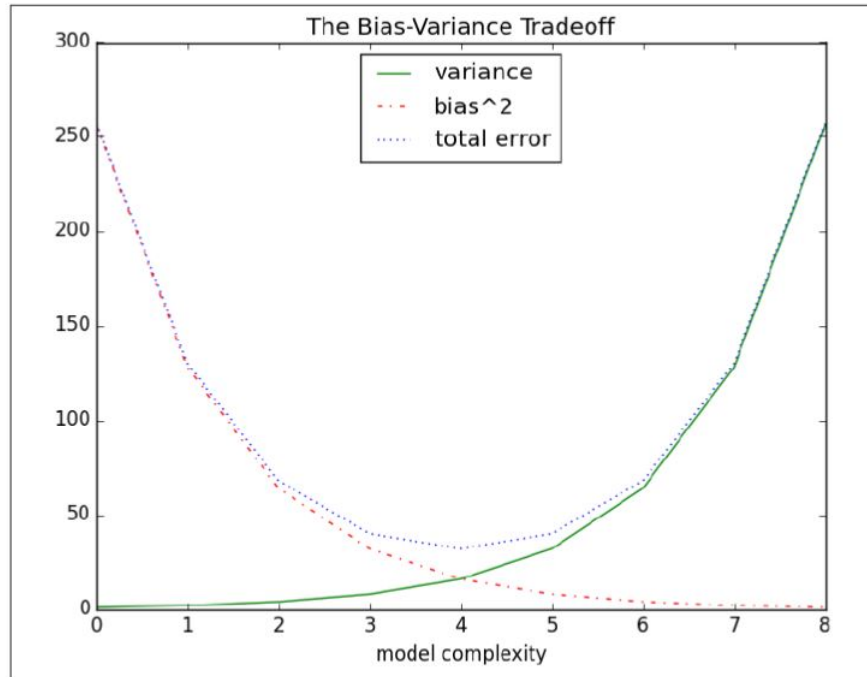
Figure 2.7: Bias-variance tradeoff [140]

From Fig. 2.7, increasing the complexity leads to decreasing error, which is because the increasing complexity of the decision boundary enables more data capturing of data with the same target label. This trend ends when the least error is achieved. Afterwards, the error will gradually increase as the decision boundary becomes too complex and cannot accommodate unseen data any more.

Accuracy Matrix

To evaluate the logistic regression model, a method called the Confusion Matrix can be used. This confusion matrix consists of four types of information, which could be used to assess the performance of a classification model. Refers to the cases in this study (i.e. feature classification on building and slope), the defect can be treated as (positive or 1) and the intact area as (negative or 0) for building inspection, while correctly predicted features can be treated as positive and wrongly predicted features

as negative for feature classification in slope. The four types of information in a confusion matrix are as follows:

True Positive (TP): the actual value of the class is positive, and the prediction returns positive.

True Negative (TN): the actual value of the class is negative, and the prediction returns negative.

False Positive (FP): the actual value of the class is negative, but the prediction returns positive. It is also known as Type I error.

False Negative (FN): the actual value of the class is positive, but the prediction returns negative. It is also known as Type II error.

Utilizing these 4 types of information in a confusion matrix (TP, FP, TN and FN), different representations of error could be derived, which are presented as follows:

$$Accuracy = \frac{TP + TN}{TP + FP + TN + FN} \tag{2.28}$$

$$Precision = \frac{TP}{TP + FP} \tag{2.29}$$

$$Recall = \frac{TP}{TP + FN} \tag{2.30}$$

$$\text{F1-score} = 2 \times \frac{Precision \times Recall}{Precision + Recall} \tag{2.31}$$

Precision and recall are metrics that can be used to evaluate a model's performance, which precision shows the accuracy of positive predictions and the proportion

of correctly predicted values among all the items that are labelled as positive predictions. Recall, which is also called sensitivity, measures the completeness of positive predictions which shows the proportion of actual positives that were correctly predicted by the classification model. F1-score is a useful metric when imbalanced datasets are used, since this metric provides a balanced measure of the classification performance of a proposed model.

Only binary classification is considered in this study, in which the ground truth of the samples of the building's external wall is used to assess the accuracy of the prediction model.

Chapter 3

Methodology

3.1 Chapter Overview

This chapter first introduces the workflows for defect/feature classification in this study, which are the Thermal Decay Mapping method and machine learning method. The equipment and the test specimens used in this study are then summarized. Field data, including case studies, are discussed at the end of this chapter.

3.2 Test Methods

3.2.1 Physical approach - Thermal Decay Mapping

Problem Statement

Several limitations of IRT were discussed in Section 2.3.7, including results can be affected by the materials' characteristics, the outdoor weather conditions, the resolution of the thermal images captured, and the orientation of the target. Furthermore,

in traditional snapshot IRT for building inspection, the detectability of the suspected defects depends on the adjustment of a suitable temperature span in the thermal images. Suspected defects can be hidden or exaggerated by an unsuitable choice of temperature span (Fig. 3.1). Fortunately, the updated test method for inspecting external wall debonding/delamination by IRT published by Hong Kong Concrete Institute [48], contributed by the author of this thesis, provided a guideline for the operators in choosing a suitable temperature span of a thermal image. According to the test method, the maximum and minimum temperatures within the ROI should be used as the range of the temperature span. However, there is another factor affecting the detectability of the suspected defects yet to be addressed, which is the timing for capturing the thermal image for inspection. The decision on the optimal time for capturing a thermal image depends on the experience of the operators. If a thermal image is captured at a time when insufficient solar radiation is absorbed by the building envelope, this results in insufficient thermal contrast between the defects and the intact area, and lowers the detectability of the suspected defects. In this study, this limitation can be eliminated by adopting the time-lapse IRT and Thermal Decay Mapping method. Fig. 3.2 shows the thermal image collected by snapshot IRT without any alterations and the Thermal Decay Map generated by the proposed method in this study. Although the thermal image collected by snapshot IRT could show the bottom row of defects clearly, the upper row of defects was affected by the shadow of an air duct and was hard to detect with the naked eye. The Thermal Decay Map could eliminate the shadowing effect and show all six embedded defects clearly with the aid of adding 2 SD, which the number of SD to be added in image enhancement will be discussed in a later section. This shows that adopting the Thermal Decay Mapping method can improve the performance in defect identification since there is no human bias in the choice of temperature span in a thermal image.

(a) Defects are hidden

(b) Defects are exaggerated
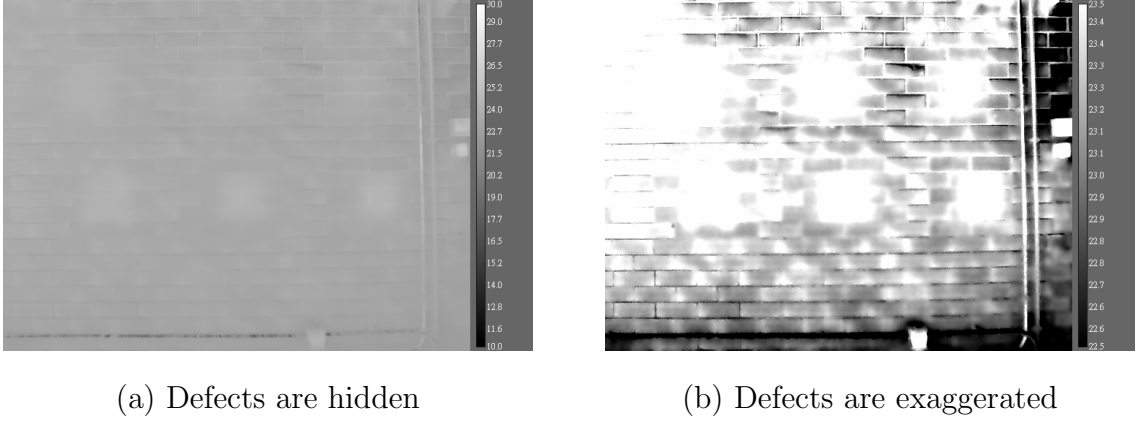
Figure 3.1: Unsuitable choice of temperature span of a thermal image on defect analysis.

(a) Raw thermal image by snapshot
IRT

(b) Thermal Decay Map (2SD)
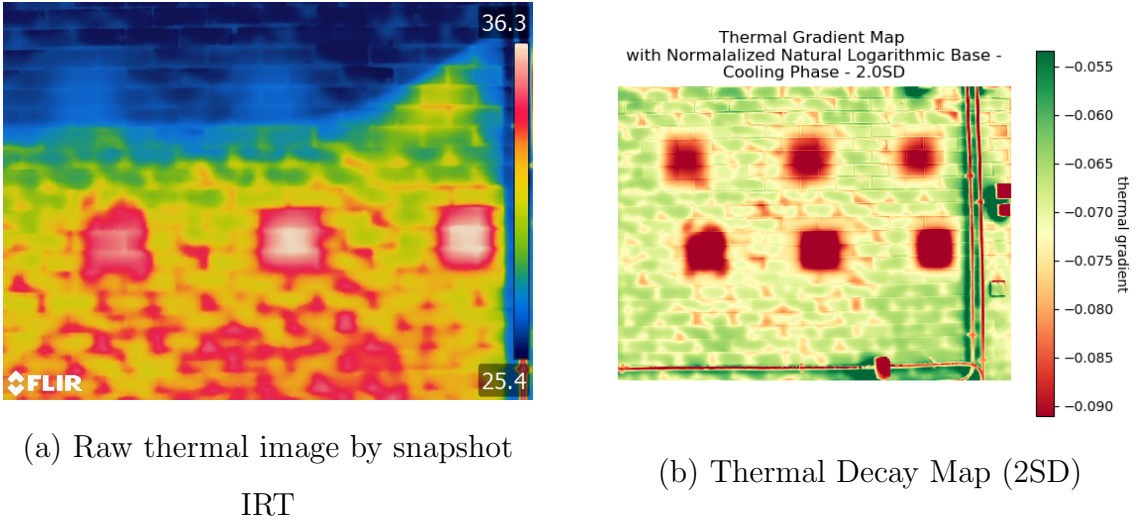
Figure 3.2: Raw thermal image and Thermal Decay Map (2SD) of the same sample wall in PolyU Position A dataset.

General Workflow

The general workflow and methodology framework for the Thermal Decay Mapping method is shown in Fig. 3.3, which consists of two main components including the Thermal Decay Mapping part and the Defect Size Estimation part.

In the Thermal Decay Mapping part (the left part in Fig. 3.3), the proposed

Methodology
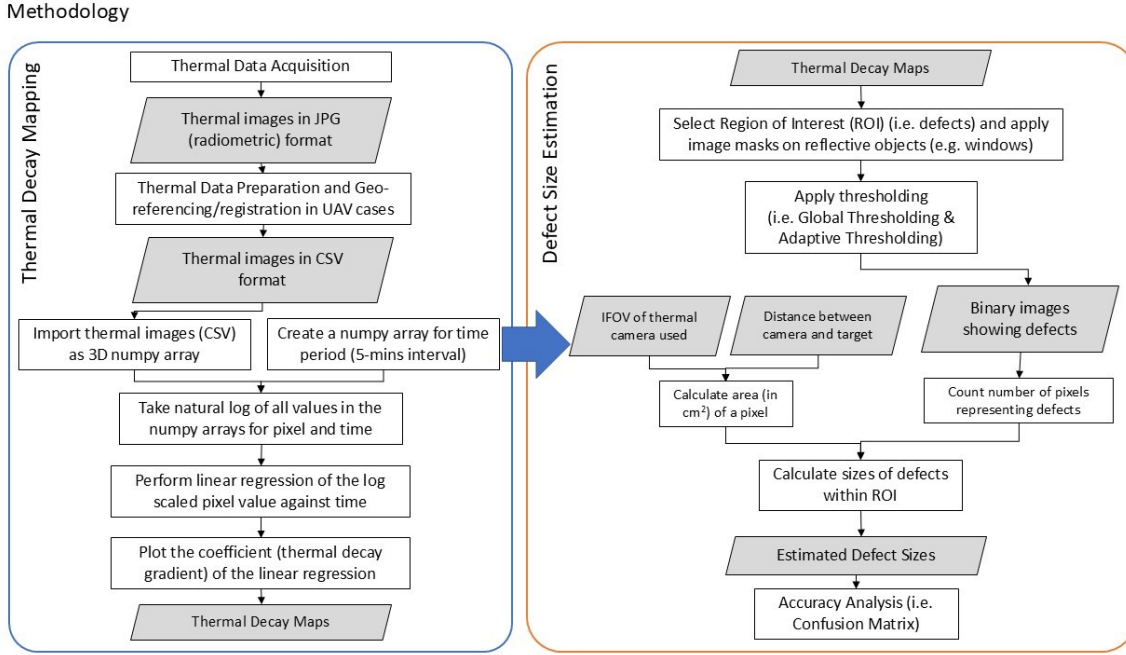
Figure 3.3: General workflow of the Thermal Decay Mapping method.

workflow in this study is modified from the point-based feature analysis in [44] and further qualitative feature classification process for the geological and geotechnical study presented in [101]. This study follows the previous research to construct a thermal decay map from the log-scaled gradient of the pixel-to-pixel temperature regression of the time-lapse IRT images for building and secondary landslide hazard inspection. The program codes are summarized in Appendix B.

Thermal images of the targets (i.e. building envelopes and rock slope surfaces) were first collected, and the details of these test specimens are summarized in Section 3.4. Since the dedicated program developed in this study uses the Python programming languags, preparation of these thermal images is necessary as these thermal images need to be imported as a NumPy array using the NumPy package in the program. In general, the original format of these thermal images is in radiometric JPEG format. To be imported as NumPy arrays, these thermal images were saved in CSV format instead. For secondary landslide hazard inspection, UAS was used in

data collection. Although the flight path of the UAS was designed and controlled by the use of a GPS signal, the GPS signal received on site was unstable because of the unstable positions of the UAS relative to the satellite in each flight. This resulted in shifts in the positions of the UAS, and therefore the thermal images collected by the UAS needed to be geo-registered and corrected to ensure consistent alignments of these thermal images. For the image registration, ArcGIS Pro was used, and all of the thermal images were referenced and aligned to the first thermal image (T_0) in the dataset. First Order Polynomial (Affine) transformation was applied to the registered thermal images. The registered thermal images were then resampled and exported in JPEG format. Since the pixel values of the exported thermal images after image registration were in 8-bit greyscale because the temperature values in the radiometric IR images were lost, the SD method was used to convert the pixel values back to pixel values in degree Celsius (discussed in Section 2.4.2). A median filter with a kernel size of 3×3 was applied to the processed images to minimize the local fluctuations caused in the image registration process.

A three-dimensional (3D) (x, y, t) NumPy array was created, which combines the thermal images in CSV format and the corresponding timestamps (in minutes) in chronological order. The first two dimensions of the 3D NumPy array are the width and length of the thermal images (i.e. resolution of the thermal images), and the third dimension is the corresponding timestamps. Another one-dimensional (1D) NumPy array was generated according to the time when the thermal images were captured (i.e. in 5-minute intervals). The values in the two NumPy arrays were normalized in natural logarithmic base, and the thermal gradient in each pixel was retrieved by logarithmic fitting since this regression fitting has the highest R2 value among other regression models [44]. The coefficient (i.e. thermal decay gradient) of the linear regression was plotted, which results in an array of thermal decay gradients which was visualized as a Thermal Decay Map using the matplotlib package in Python. In the Thermal Decay Map, the value in each pixel represents the change in temperature

over a time period. The "RdYlGn" colour map was used to represent the larger gradient in red and the smaller gradient in green. The resulting Thermal Decay Map was then used for feature classification, which fulfilled the thermal decay analysis part in Objective 1. Further discussion regarding the factors affecting the detectability of subsurface defects and other features on buildings and slopes is discussed in Chapter 4.5 and 5.5 respectively, which copes with Objective 2 in this study.

In the Defect Size Estimation part (the right part in Fig. 3.3), the Thermal Decay Map created was imported into a dedicated Python program. Since there are unwanted features (i.e. windows) in building envelopes, an image mask was applied to eliminate unwanted features and a region of interest (ROI) was selected. Then, thresholding was applied to the masked image. In the global thresholding method, a threshold value was automatically calculated by Otsu's thresholding method [127]. In the adaptive thresholding method, three block sizes, which means the size of the neighbourhood area, were selected for the automatic threshold calculation. The selected block sizes, which are IFOV-dependent, are as follows:

- 3×3: the smallest block size can be used in the package;

- 25×25: the size of the embedded defect in the sample wall described in Section 3.4.1;

- 479×479: the width of a thermal image captured by FLIR T650sc.

After applying the thresholding, filtering was applied to eliminate unrelated small objects, and binary images were produced. Since only the building dataset had ground truth data, the resulting binary images of the target wall were then analysed by calculating the confusion matrix with the ground truth, including the calculation of the numbers of TP, TN, FP and FN (as discussed in Section 2.5.3), to fulfil Objective 3 in this study. These four variables represent the following results:

- TP: Correct detection of defects;

- TN: Correct detection of intact area;

- FP: Incorrect detection of defects;

- FN: Incorrect detection of intact area.

Different representations of the error of the defect identification from adopting the Thermal Decay Mapping method were calculated according to the equations listed in Section 2.5.3. Size estimation of the detected defects/features was performed by counting the number of pixels in white in the binary image, and scaling the pixel resolution to actual size through IFOV calculation or scaling the pixel to a known size in any IR images.

For the slope dataset, the performance of the feature classification using the Thermal Decay Mapping method was evaluated by the comparison between the findings in the GEO reports published by the HKSAR government, previous research conducted in [44, 101], visual images and the original thermal images.

3.2.2 Statistical Approach - Machine Learning

The general workflow and methodology framework for the Machine Learning method is shown in Fig. 3.4, which consists of two main components including the training part and the testing part. The proposed workflow in this study is modified from the research on defect diagnosis in reinforced concrete structures using ground penetrating radar and machine learning in [141]. The program codes are summarized in Appendix B.

In the training part (the left part in Fig. 3.4, thermal images of the targets (i.e. building envelopes and rock slope surfaces) were first collected, and the details of these test specimens are summarized in Section 3.4. The thermal data preparation including the conversion from radiometric JPEG format to CSV format was the same

Methodology
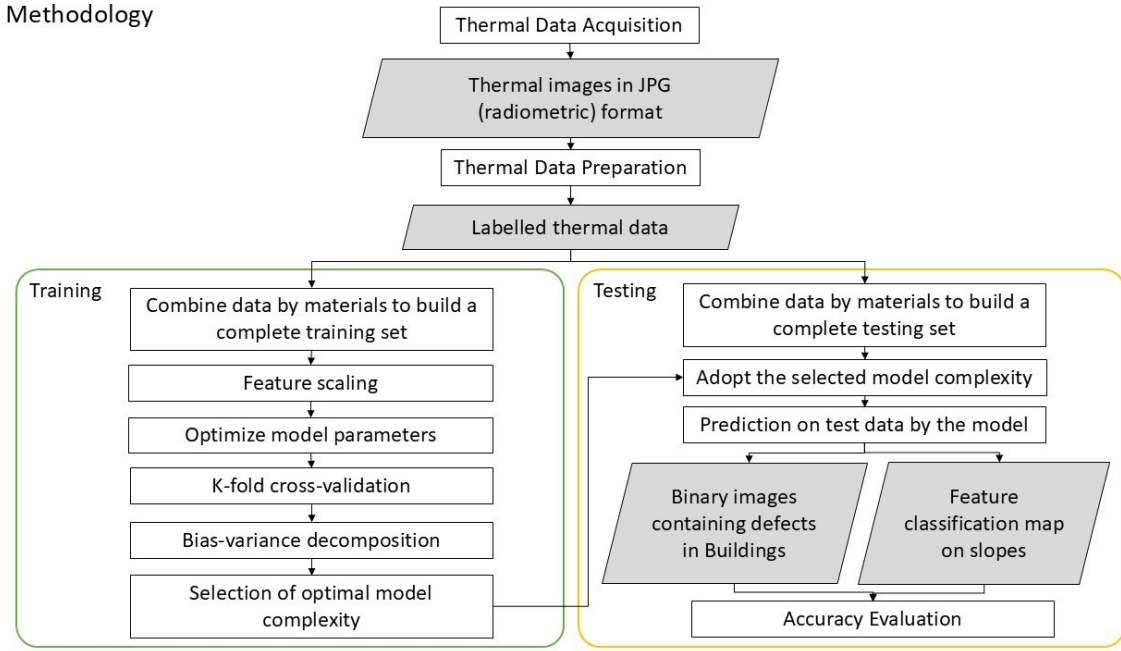
Figure 3.4: General workflow of the Machine Learning method.

as described in Section 3.2.1. Pixel-based features were extracted from the thermal data for labelling.

For building inspection, thermal contrasts between the defects and the intact area in the heat absorption period and the heat dissipation period were used as the two features for classification. The minimum temperature detected within the ROI was used as the reference temperature. The thermal contrast value of every pixel within the ROI was calculated by subtracting the reference temperature from the temperature value in each pixel. Further discussion on selecting which sequences of thermal images in the whole dataset is conducted in Chapter 6. In the training dataset, the pixels in the defects were labelled as "1", while the pixels in the intact area were labelled as "0".

For secondary landslide hazard inspection, thermal contrasts between the area showing thermal anomalies and the intact area (i.e. area without thermal anomalies, like vegetation) in the heat absorption period and the heat dissipation period were

used as the selected features for classification (Fig. 3.5). For example, in Fig. 3.5, the thermal contrasts between the intact rocks and the suspected water seepage on the slope form very thin line patterns in the thermal image, which indicates the potential of using thermal contrasts for training a model. The minimum temperature detected within the ROI was used as the reference temperature. The thermal contrast value of every pixel within the ROI was calculated by subtracting the reference temperature from the temperature value in each pixel. In the training dataset, the pixels in the area showing thermal anomalies were with labels ranging from 1 to 4, which represent fresh ash tuff with two weathering grades, basalt and faults respectively, while the pixels in the intact area were labelled as "0". Further discussion on selecting which sequences of thermal images in the whole dataset and how to define the label number of a pixel is conducted in Chapter 6.
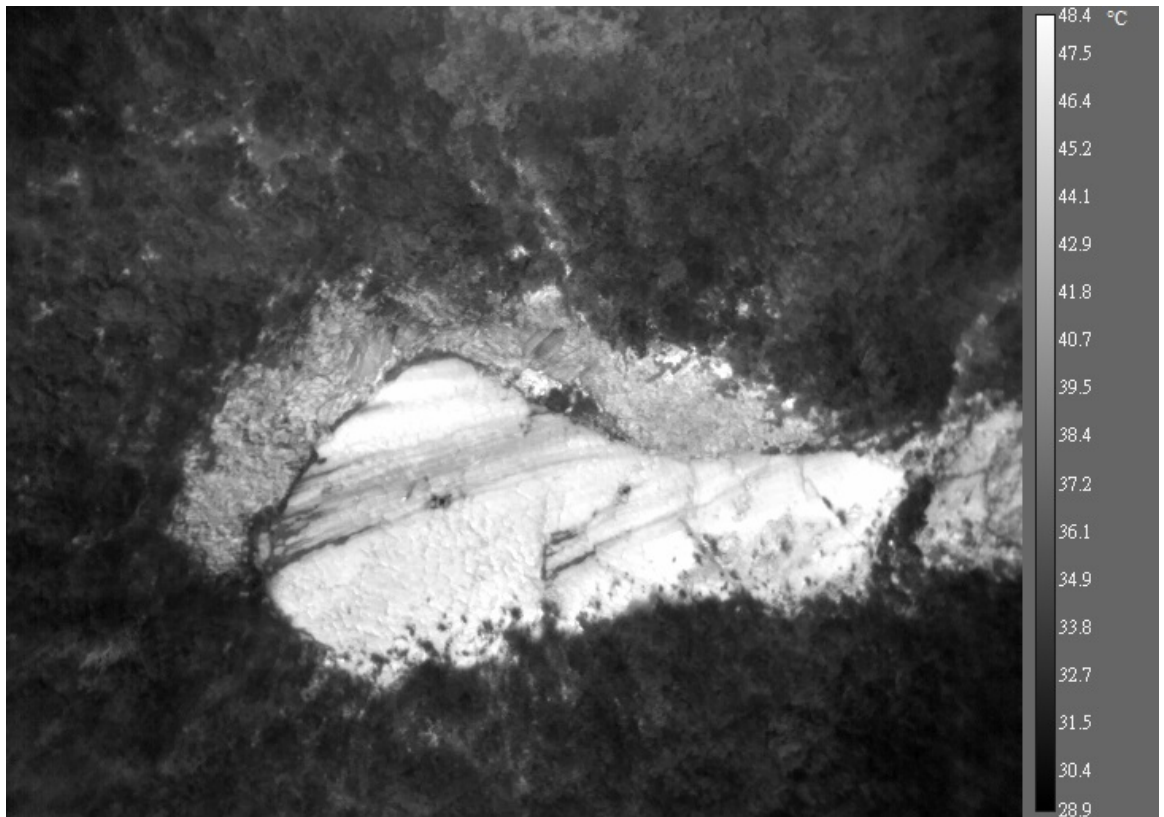
Figure 3.5: Example thermal image showing thermal contrasts of different features.

Feature scaling was performed on the dataset with the labelled thermal data, and cross-validation was performed on the model developed using the prepared training set. The degree of generalisation of the classification model was then determined by observing the bias-variance decomposition. The model with the best generalisation was selected and the corresponding parameters were then used in the testing part.

In the training part, the optimal model complexity obtained in the training part was adopted and the prediction was performed on the testing dataset by the selected model. The accuracy of the results (i.e. binary images containing defects in the building inspection part, and feature classification map in the secondary landslide hazard inspection part) was then evaluated through the calculation of a confusion matrix, which used the same procedures as described in Section 3.2.1. After the accuracy evaluation, the conclusion can be drawn whether Objectives 1, 2 and 3 have been achieved by the machine learning method.

3.3 Equipment

The thermal cameras and the UAS used in this study are summarized in Tables 3.1 and 3.2, which fulfilled the requirements listed in HKCI TM1 [48].

Table 3.1: Specifications of the thermal camera used.

Model	Lens (mm)	Frequency (Hz)	Resolution	Sensitivity (mK)	FOV	IFOV (in mrad)
FLIR T650sc	13.1	30	640×480	<20	$45° \times 33.7°$	1.226
Zenmuse XT2	13	9	640×512	50	$45° \times 37°$	1.308

3.4 Test Specimens

This section summarizes the test specimens used in this study, including 2 sample walls and an external wall of a building for building inspection, and 2 selected

Table 3.2: Specifications of the UAS used.

Model	Max Takeoff Weight (kg)	Hovering Accuracy (m)	Max Angular Velocity (°/s)	Max Speed (Dual Downward Gimbals) (kph)	Max Wind Resistance (m/s)
DJI M210	6.14	Vertical: ±0.5, Downward Vision System enabled: ±0.1 Horizontal: ±1.5, Downward Vision System enabled: ±0.3	Pitch: 300; Yaw: 150	S Mode: 64.8; P Mode: 61.2; A Mode: 61.2	12

rock slopes for secondary landslide hazard inspection.

3.4.1 Experimental Setup - Building Wall Finishes

Training Set

To study the effects of different material properties on defect identification of the proposed methods, a sample concrete wall was constructed, with dimensions of 1160 mm (L) x 1900 mm (W) x 2000 mm (H), and divided into 8 types of finishes. In each finish type, 5 low-density polystyrene foam plates with a 7.5 cm diameter were fixed before laying render and various mosaic and ceramic tile composites. The cover depths of polystyrene foam plates were 5, 5, 8, 15 and 17 mm respectively (Fig. 3.6). Only Defects A to D were used in this study since the remaining 5 mm defect in the render section is blocked by a metal wire which is not suitable for data comparison. 7 sections of the concrete panel were covered with 3 mosaic tile composites and 4 ceramic tile composites in different colours and textures which are commonly used tile composites in Hong Kong and Asia, and the remaining section was covered with render as shown in Fig. 3.7. Data was collected on multiple days and locations, and used as the testing sets in the Thermal decay mapping method and the training sets in the machine learning method respectively.
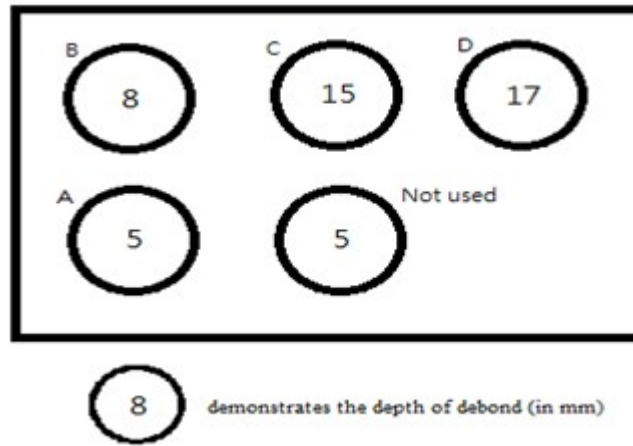
Figure 3.6: Embedded debonds with various cover depths in each section.
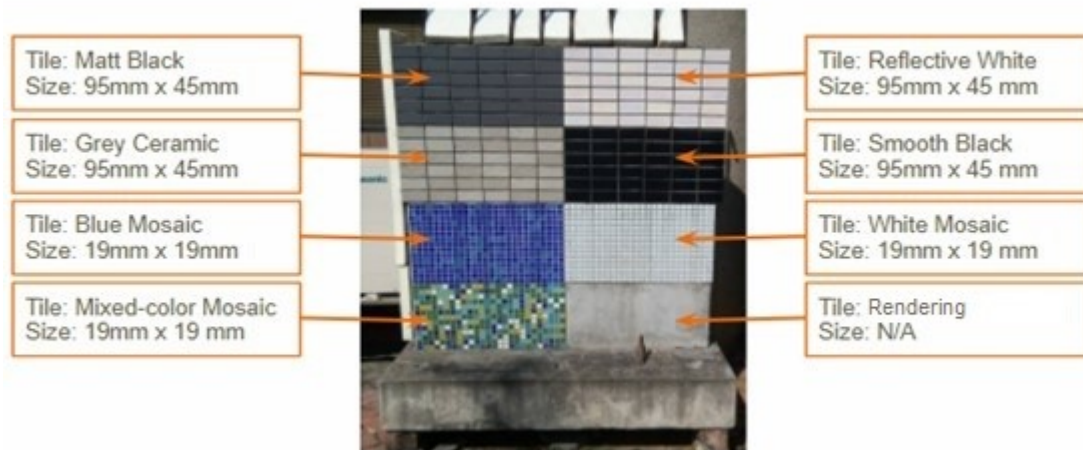
Figure 3.7: Sample concrete wall with various mosaic tile and ceramic tile composites.

The emissivity values of each wall finishing material were determined through an in-house experiment conducted according to ASTM E1933-14 [142] and described as follows. In the experiment, the temperatures of a black tape, acting as a black body with an emissivity value of 0.95, and the different wall finishing materials were collected by taking thermal images with FLIR T650sc handheld infrared camera (whose specifications are listed in Table 3.1. The samples of wall finishing materials were heated up using an active heat source (flash heads with Elinchrom Digital RX 2400

generator in full power (2400 Ws)). The thermal images collected were then imported into the manufacturer's software "FLIR Tools" to determine the emissivities of the selected wall finishing materials by adjusting the emissivity value to let temperatures of wall finishing materials shown change to the temperature values shown at the black tape (i.e. temperature close to the black body). The temperature values of the wall finishing materials and the black tape were summarized in Table 3.3. These temperature values were used in the calculation of emissivity using Eq. 3.1. Note that this emissivity value is an approximation only because the black tape used in the experiment is not a real black body.

$$\varepsilon_g = (\frac{T_g}{T_B})^4 \qquad (3.1)$$

Where ε_g is the emissivity value of the testing materials, T_g and T_B are the temperature values of the testing materials and the blackbody (i.e. the black tape) respectively. The emissivity values of selected wall finishing materials in Table 3.3 were sorted into three main groups: Group 1 - Rendering with the highest emissivity, Group 2 - High Emissivity Materials (0.85 - 0.88) and Group 3 - Low Emissivity Materials (0.51 - 0.73).

In this study, there were 2 datasets using the sample wall mentioned above, which were collected at Shek Mun and Ping Che respectively, The details of these 2 datasets are discussed in the following sub-sections.

Table 3.3: Temperature Values of Various Wall Finishing Materials Recorded

Group	Material	Temperature value of materials (℃)	Temperature value of materials (℃)	Emissivity value calculated according to Eq. 3.1
1	Rendering	34.5	35.0	0.94
2	Blue Mosaic	33.9	35.0	0.88
2	Smooth Black	33.7	35.0	0.86
2	Matt Black	33.6	35.0	0.85
3	Grey Ceramic	32.3	35.0	0.73
3	Reflective White	31.6	35.0	0.66
3	White Mosaic	30.3	35.0	0.56
3	Mixed Mosaic	29.6 - 33.7	35.0	0.51 - 0.86

First Dataset - Shek Mun (2018)

The first dataset was collected in 2018, and the sample wall was put in the Hong Kong Polytechnic University's (PolyU) Road Lab in Shek Mun of Hong Kong (Fig. 3.8). It was arranged to face exactly towards the East to be exposed to direct and natural sunlight in the morning for simulating perfect heat absorption and dissipation in the morning and in the evening, respectively. To capture thermal images of the sample wall, the thermal camera FLIR T650sc, whose specifications are listed in Table 3.1, was used and it was mounted on a tripod in a fixed position to ensure the area capturing in each thermal image is the same (Fig. 3.9). The distance between the thermal camera and the target surface was 2.5 m, with a spatial resolution (IFOV) of 0.0939 cm^2. Thermal images of this sample wall were captured every 5 min from 8:30 to 21:00 to evaluate the difference in temperature through a time-lapse analysis. Data was collected on three different sunny days with similar weather conditions, and the weather on each survey day is summarized in Table 3.4 [143–147].

Figure 3.8: Location of experiment site in Shek Mun. (Base map retrieved from Google Map [148])

Remarks: The PolyU's Road Lab was located at the marked position. The land lot was resumed by the HKSAR government, and a subsidised-sale public housing called Yu Tak Court was built at this site.

Figure 3.9: Experiment set-up facing East in Shek Mun.

Table 3.4: Weather summary for each survey day in First Dataset

	Day 1 11 Jan 2018 (Sunny)	Day 2 6 Feb 2018 (Sunny)	Day 3 22 Mar 2018 (Sunny)
Average Temperature	12.1℃- 16.1℃	7.9℃- 14.2℃	16.2℃- 24.1℃
Humidity	37% - 48%	40% - 66%	50% - 71%
Average Ambient Gamma Radiation (in microsievert (MS))	0.12	0.12	0.12MS
Cloud Coverage	37%	48%	9%
Wind Speed*	31km/h	32.2km/h	18.9km/h

Remarks(*): The wind speed listed above is the official record from the Hong Kong Observatory, and it was recorded from Waglan Island which is for reference only.

Second Dataset - Ping Che (2021)

The second dataset was collected in 2021, when the sample wall was moved to an outdoor site in Ping Che, Fanling, Hong Kong (Fig. 3.10). It was arranged to face towards the South to observe the heat absorption and dissipation in the morning and the evening respectively when the target surface was not exposed to direct natural sunlight compared to the first dataset. To capture thermal images of the sample wall, the thermal camera FLIR T650sc, whose specifications are listed in Table 3.1, was used and it was mounted on a tripod in a fixed position to ensure the area capturing in each thermal image is the same (Fig. 3.11). The distance between the thermal camera and the target surface was 2.8 m, with a spatial resolution (IFOV) of 0.118 cm^2. Thermal images of this sample wall were captured every 5 min from 9:45 to 17:45 to evaluate the difference in temperature through a time-lapse analysis. Data was collected on two different sunny days with similar weather conditions, and the weather on each survey day is summarized in Table 3.5 [146, 149–151].
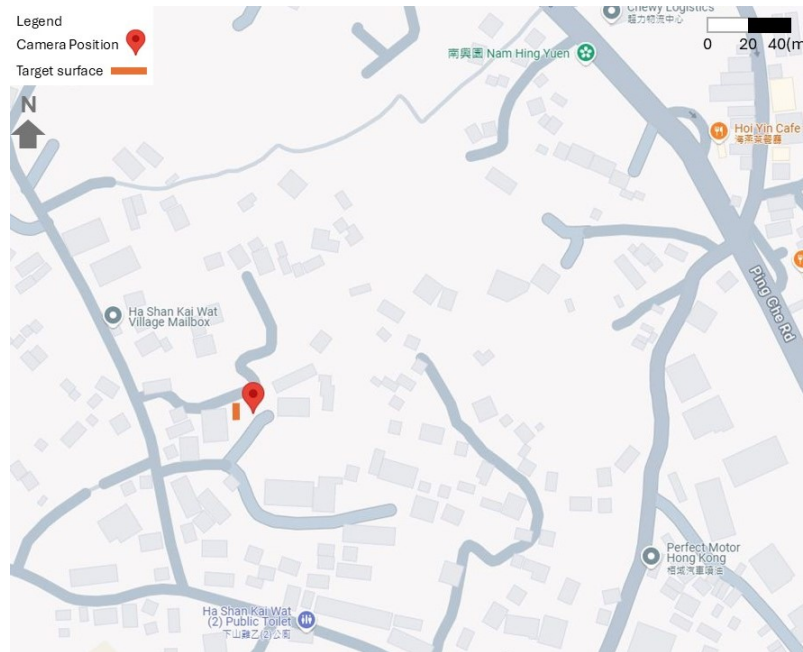
Figure 3.10: Location of experiment site in Ping Che. (Base map retrieved from Google Map [152])

Figure 3.11: Experiment set-up facing South in Ping Che.

Table 3.5: Weather summary for each survey day in Second Dataset

	Day 1 12 Nov 2021 (Sunny)	Day 2 10 Dec 2021 (Sunny)
Average Temperature	20.0℃- 25.7℃	18.6℃- 23.7℃
Humidity	42% - 61%	59% - 82%
Average Ambient Gamma Radiation (in microsievert (MS))	0.10	0.10
Cloud Coverage	54%	30%
Wind Speed*	1.5km/h	1.6km/h

Remarks(*): The wind speed listed above were recorded by wind speed meter on site.

Testing Set

To validate the prediction results by the machine learning method, another sample wall with ground truths was constructed at the rooftop of the Industrial Centre on PolyU's campus, which faces Northwest (Fig. 3.12). 10 low-density polystyrene foam plates with an area of 400 cm^2 were embedded in the sample wall. 6 of them were covered with reddish-brown wall tiles and rendering while 4 of them were covered with rendering only (Fig. 3.13). The thickness of the foam plates used in each debond and their corresponding cover depths are summarized in Table 3.6. To capture thermal images of the sample wall, the thermal camera FLIR T650sc, whose specifications are listed in Table 3.1, was used and it was mounted on a tripod in a fixed position to ensure the area capturing in each thermal image is the same (Fig 3.14). The distances between the thermal camera and the target surface were 2.8625 m, with a spatial resolution (IFOV) of 0.123 cm^2, at Position A and 3.406 m, with a spatial resolution (IFOV) of 0.174 cm^2, at Position B. The experiments were conducted in a 24-hour cycle, in which thermal images of the sample wall were taken once every 5 minutes, to evaluate the difference in temperature through a time-lapse analysis. Data was collected on two different sunny days with similar weather conditions, and

66

the weather on each survey day is summarized in Table 3.7 [153].

Figure 3.12: Location of sample wall in PolyU. (Base map retrieved from Google Map [154])

(a) Position A

(b) Position B

Figure 3.13: Embedded debonds on PolyU's sample wall.

Figure 3.14: Experiment set-up in PolyU.

Table 3.6: Details of embedded debonds on the sample wall

Debond	Foam Thickness (mm)	Cover Depth (mm)
A	12	15
B	6	15
C	3	15
D	12	23
E	6	29
F	3	32
G	6	19
H	1	24
J	12	13
K	3	22

Table 3.7: Weather summary for each survey day in Testing Dataset

	Day 1 Position A (Sunny)	Day 2 Position B (Sunny)
Starting time	3 Feb 2021 9:35 am	20 Apr 2021 9:24 am
Ending time	4 Feb 2021 9:10 am	21 Apr 2021 9:19 am
Average Temperature*	15.8℃- 23.6℃	23.4℃- 24.5℃
Humidity*	63%	73%
Wind Speed*	11.4 - 16.5km/h	19.5 - 31.7km/h
Total bright sunshine	10.2 hours	10.8 hours

Remarks(*): The average temperature, humidity and wind speed listed above were recorded by data logger and wind speed meter on site.

3.4.2 Experimental Setup - Rock Slope

Two sites were selected for conducting the time-lapse IRT study for secondary landslide hazard inspection. The details of the 2 assigned sites are summarized in Table 3.8. The weather on the survey day in each site is summarized in Table 3.9 [146, 151, 155–157]. The dataset collected in Site 2 was used as the training set, and the dataset collected in Site 1 was used as the testing set. The details of each dataset are summarized in the following sub-sections.

Table 3.8: Summary of site details

Site	Details
Site 1	Natural terrain above Sai Wan Road at Sai Kung
Site 2	East Dam of High Island Reservoir (Slope Nos. 8SE-D/C6 and 8SE-D/C7)

Table 3.9: Weather summary for each survey day in each site

	Site 1 9 Sept 2021 (Sunny)	Site 2 11 Jul 2022 (Sunny)
Average Temperature	27.8℃- 33.5℃	28.5℃- 35.1℃
Humidity	65% - 81%	57% - 86%
Average Ambient Gamma Radiation (in microsievert (MS))	0.12	0.11
Cloud Coverage	66%	30%
Wind Speed*	10.4km/h	9.2km/h

Remarks(*): The wind speed listed above is the official record from the Hong Kong Observatory, and it was recorded from Waglan Island which is for reference only.

Training Set

Site 2 is located at the UNESCO Global Geopark in High Island Reservoir, Sai Kung of Hong Kong, which is in the eastern part of Hong Kong (Fig. 3.15). The target rock slope is selected due to the presence of unique hexagonal rock columns and a basaltic dyke protruding through fine ash tuff (Fig. 3.16). The emissivities of basalt dyke and fine ash tuff are 0.94 and 0.975 respectively [108]. Ground-based IRT was adopted in the data collection to ensure pixel-to-pixel comparison. The thermal camera (model: FLIR T650sc, whose specifications are listed in Table 3.1) was arranged to face towards the target surface perpendicularly. The distance between the thermal camera and the target surface was 24.78 m, with a spatial resolution (IFOV) of 9.23 cm^2. Data was collected on three different sunny days with similar weather conditions, and the weather on each survey day can be referred to Table 3.9.

Figure 3.15: Location of target rock slope in Site 2. (Base map retrieved from Google Map [158])

Figure 3.16: Target rock slope in Site 2.

Testing Set

To validate the prediction results by the Thermal Decay Mapping method and machine learning method, Site 1 was selected, where a severe landslide had occurred. Site 1 is located in the natural terrain above Sai Wan Road in Sai Kung, Hong Kong, where several landslides occurred in May 2016 (Fig. 3.17). This site was suggested by the government in the previous research on evaluating thermal decay analysis on natural terrain by adopting a time-lapse IRT survey with UAS [44]. The target rock slope was selected since representative landslides occurred at the site, and human access to the site was troublesome. Referring to the GEO report published by the Geotechnical Engineering Office of the HKSAR government [159], a severe rainstorm occurred on 21 May 2016, which caused several landslides along Sai Kung Sai Wan Road. The main survey area selected was the source area of the largest landslides reported at Site 1, which the detached source volume was assumed to be 2100 m^3. This landslide caused the closure of Sai Wan Road for several months. The main type of rocks in Site 1 is columnar jointed fine ash tuff [160] (the same type of rocks in the training set), and there is no fault located in the neighbouring region of the selected site [161]. There were no signs of instabilities before the occurrence of the landslide on 21 May 2016, and no inspection could be performed until 31 May 2016 when the debris blocking Sai Wan Road was cleared [159]. Hence, a UAS IRT survey has the benefits of remote natural terrain inspection when there is no direct access to the survey area. Since this study adopted a UAS IRT survey at Site 1, the design of the flight path is presented in Fig. 3.18 (which is modified from Fig. 3 in [44] as only Slope A was used in this study). Visual inspection and 3D terrain modelling by photogrammetry were also conducted in this study.

Since the whole area could not be captured in one thermal image when considering the resolution of a thermal image, the survey area was divided into two parts, which were Part 1 and Part 2 (shown in Fig. 3.18). A UAS (model: DJI M210) was equipped with a thermal camera (model: Zenmuse XT2), whose specifications are
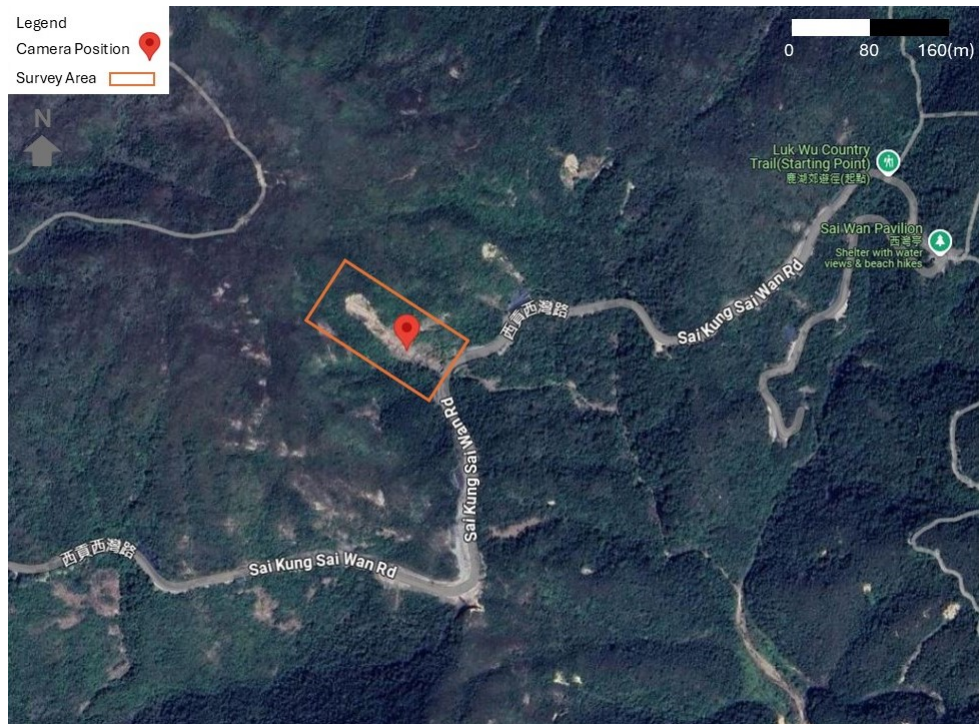
Figure 3.17: Location of target rock slope in Site 1. (Base map retrieved from Google Map [162])
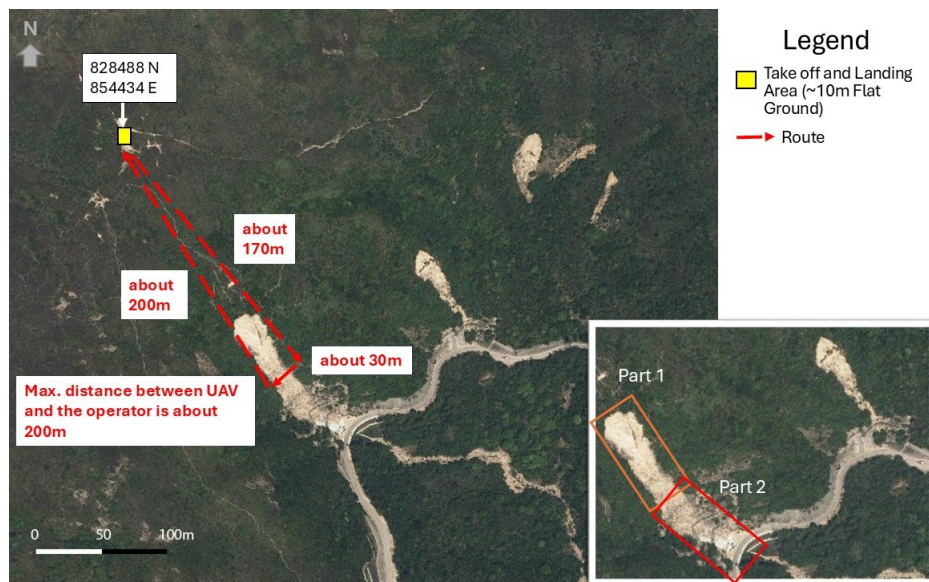
Figure 3.18: Designed flight path for slope inspection in Site 1. [44]

listed in Table 3.2 and Table 3.1 respectively. The thermal camera was arranged to face towards the target surface perpendicularly. The distances between the thermal camera and the target surface in Part 1 and Part 2 were both at 115 m, with a spatial resolution (IFOV) of 226 cm^2. Data was collected on a survey day with fine weather conditions, and the weather on the survey day can be referred to Table 3.9.

3.4.3 Chapter Summary

This study proposed two approaches to perform defect identification on building envelopes and feature classification in natural terrain, which were the physical approach (the Thermal Decay Mapping method), and the statistical approach (the machine learning method). The general workflows of these two proposed methods were summarized in this chapter, which aimed to fulfil the three objectives proposed in this study. Objective 1 is to classify subsurface defects in building structures, and features like rocks, cracks/fractures and vegetation in natural terrain. Objective 2 involves a discussion of different factors affecting the detectability of features by these two proposed methods. The performance of these two proposed methods was then assessed by the calculation of a confusion matrix, which fulfilled Objective 3 in this study.

To sum up, this study shows the potential of adopting the Thermal Decay Mapping method and the machine learning method in different scenarios, including building inspection and secondary landslide hazard monitoring. The IRT surveys in the current practice only provide qualitative results like number of suspected defects of the target surface, which do not reflect the true severity of the defects and the structural health of the target. Therefore, quantitative analysis shall be performed, and this study proposes novel approaches when compared to other quantitative analyses in the research field. Thermal decay coefficients of the target surface, and the thermal contrasts between the thermal anomalies and the intact area of the target

were utilized in the Thermal Decay Mapping method (TDMM) and the machine learning method respectively. The results including binary images containing defects and feature classification maps could be used for feature size estimation, which is believed to be an improvement in both building external wall diagnosis and secondary landslide hazard monitoring. The performance and the factors affecting the accuracy of the two proposed methods will be discussed in the coming chapters. A series of experiments and validation using the test specimens and methodologies described in this chapter will be executed to fulfil the four objectives of this study.

Chapter 4

Thermal Image Processing by Physical Approach (Thermal Decay Mapping) - Building Inspection

4.1   Chapter Overview

This chapter summarizes the results of defect classification on building envelopes by adopting the Thermal Decay Mapping method. The characteristics of each dataset such as histograms and temporal plots of the wall finish materials used are presented. Results and discussions for building inspection are summarized, including the factors affecting the defect classification results, and the accuracy of performance on different materials.

4.2 Thermal Data Preparation

Following the general workflow summarized in Section 3.2.1, the first step is thermal data preparation. Since the Thermal Decay Mapping method studies the temperature distribution of the target surface in the heat dissipation period, it is necessary to examine the temporal plot of all the features on the target surface to determine the starting frames to be adopted in data processing. The datasets used in this chapter included datasets collected in Shek Mun, Ping Che and PolyU for building inspection, which the details were described in Section 3.4.1.

The dataset collected on Day 1 in Shek Mun dataset was used for the discussion in this section. The temporal plots of all wall finishes in Day 1 dataset were presented in Fig. 4.1 and 4.2. Two peaks can be observed in each temporal plot. The first peaks (i.e. the temperature curves hit its maximum temperatures at the first time), indicated by orange arrows in the figures, occurred at the frame numbers ranging from 27 to 33 (i.e. 10:30 am to 11:05 am), which were in the heat absorption period since the sample wall was arranged to face towards the East and the sample wall was heated up in the morning session. After the occurrence of the first peaks, heat dissipation occurred. However, second peaks (i.e. the temperature curves hit their second maximum temperatures after slightly cooling down), indicated by blue arrows in the figures, could be observed at the frame numbers ranging from 81 to 90 (i.e. 3:05 pm to 3:50 pm). This can be explained by the characteristics of the sample wall, which the thickness of the sample wall is 380mm. The sample wall was located in an outdoor environment where no building or object was put behind the sample wall. Hence, the back of the sample wall which was facing West was heated up by solar radiation, which caused the second peaks and the temperatures were not as high as in the first peaks.

To study the thermal behaviours between the defect area and the intact area, histograms were selected from each group in Shek Mun Day 1 dataset and presented
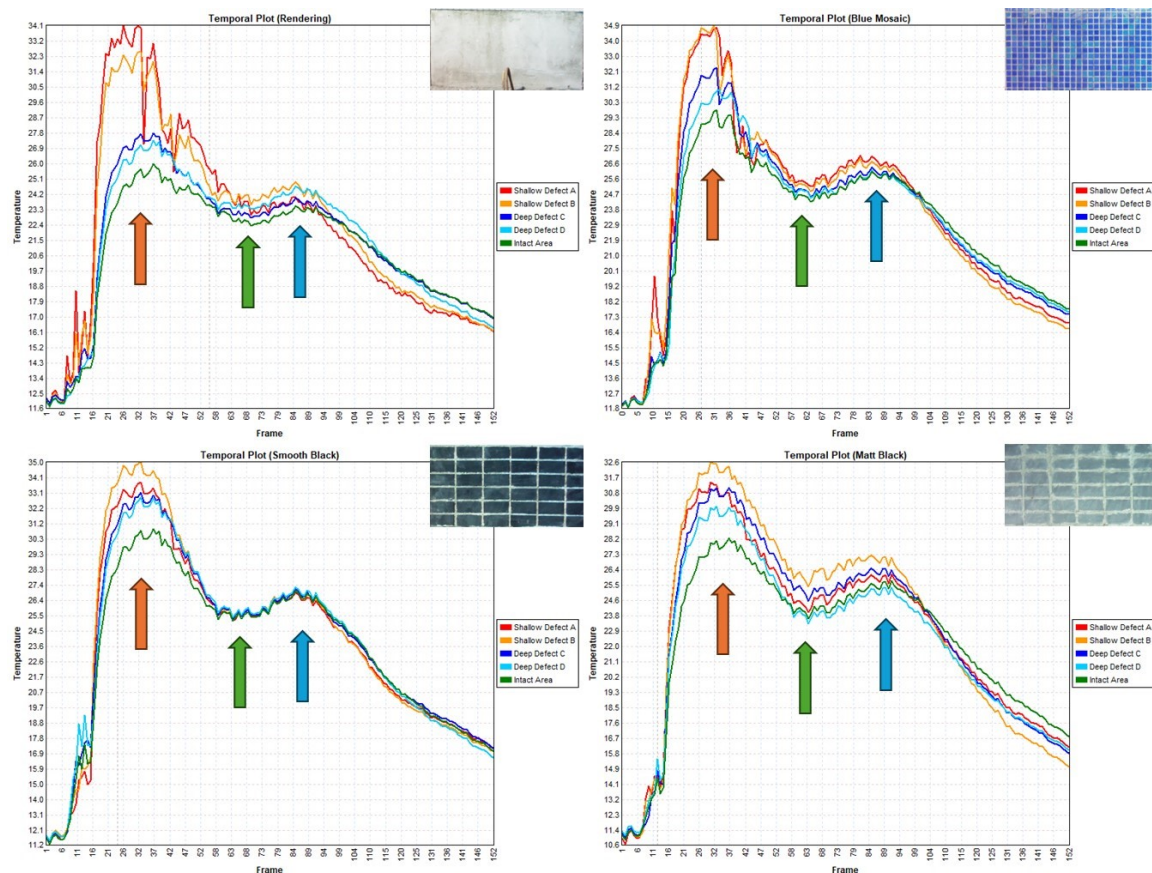
Figure 4.1: Temporal plots of wall finishes in highest emissivity group (Group 1 - Rendering) (top left-handed corner) and high-emissivity group (Group 2 - Blue Mosaic, Smooth Black and Matt Black) in Shek Mun Day 1 dataset.

Remarks: • Frame in this plot can be converted to time, in which the starting time was 8:23 am, and the images were taken at 5-min intervals. • Orange arrows indicate the first peaks; green arrows indicate the troughs between the first peaks and the second peaks; blue arrows indicate the second peaks.

in Fig. 4.4. The embedded defects were sorted into two groups based on their cover depths (Fig. 3.6), which were shallow defects (Defects A (5mm) and B (8mm)), and deep defects (Defects C (15mm) and D (17mm)). In the histograms, the colour representation of shallow defects, deep defects and the intact area are red, yellow and green respectively. During the heat absorption period, both shallow defects and deep defects can be separated from the intact area, where a part of the deep defects overlaps with the intact area. The distributions of shallow defects and deep defects overlap each other in Group 2 and 3 materials. This shows the potential of defect identification

78
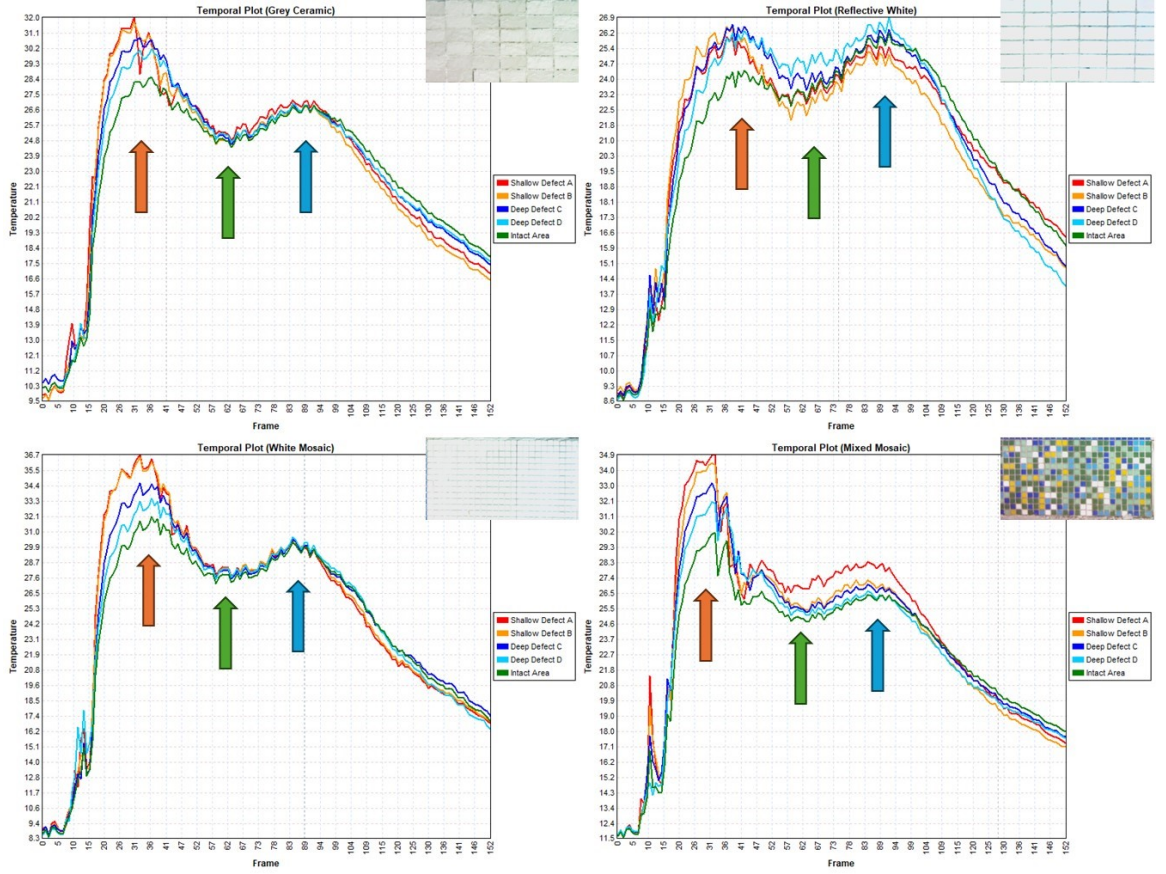
Figure 4.2: Temporal plots of wall finishes in lower emissivity group (Group 3 - Grey Ceramic, Reflective White, White Mosaic and Mixed Mosaic) in Shek Mun Day 1 dataset.

Remarks: • Frame in this plot can be converted to time, in which the starting time was 8:23 am, and the images were taken at 5-min intervals. • Orange arrows indicate the first peaks; Green arrows indicate the troughs between the first peaks and the second peaks; Blue arrows indicate the second peaks.

by using IRT since the distribution of the defects and the intact area allows feature segmentation. However, during the heat dissipation period, the distribution of both shallow defects and deep defects overlaps with the intact area. The thermal contrast between the defects and the intact area in the heat dissipation period, which depends on the rate of cooling in the defective area and the intact area, is not as significant as that in the heat absorption period when there is a passive heat source (i.e. sunlight) to generate the thermal contrast. Therefore, this means that defect identification in the heat dissipation period will be difficult as there is no significant boundary to separate

79

the defects from the intact area. This results in the limitation of adopting snapshot IRT as the timing for capturing a single thermal image in normal practice seriously affects defect identification. Time-lapse IRT utilizes all the thermal images captured in a specific period to increase the possibility of successful defect identification in the target surface. Therefore, as the temperature distribution of the target surface in the heat dissipation period is the main focus of the Thermal Decay Mapping method, thermal images within the first peaks (orange arrows in Fig. 4.1 and 4.2) and the trough between the first peak and the second peak (green arrows in Fig. 4.1 and 4.2), which appeared between Frame 62 (1:33 pm) to 69 (2:08 pm) in each dataset collected in Shek Mun were used for producing thermal decay maps in later session, which the summary of the thermal images used is summarized in Appendix A. Fig. 4.3 shows the corresponding thermal images taken at the first peaks, the trough between the first peaks and the second peaks, and the second peaks respectively. For the datasets collected in Ping Che and PolyU, since the back of the sample wall was blocked by other objects, faced South (Ping Che), and did not heat up by solar radiation, there was only 1 peak (Fig. 4.5). Therefore, thermal images within the heat dissipation period, starting from the peak to the end of the whole period in the dataset were used for producing thermal decay maps in later sections.

(a) First Peak (Orange arrow) (b) Trough between First Peak and Second Peak (Green arrow) (c) Second Peak (Blue arrow)
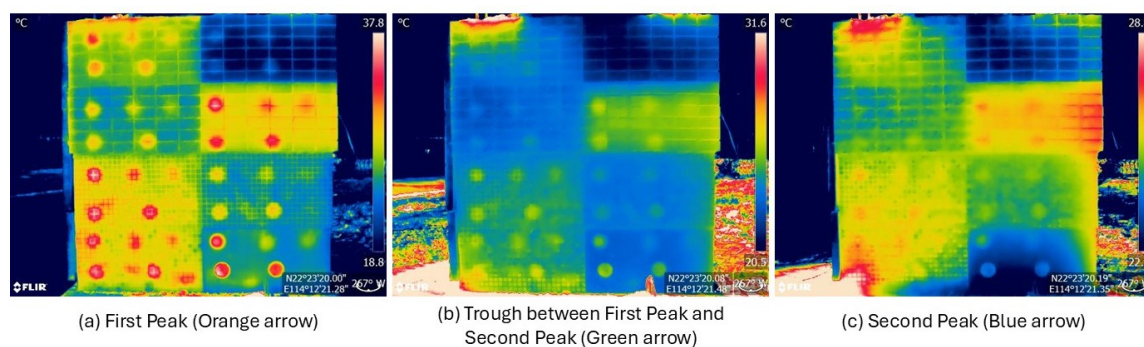
Figure 4.3: Thermal images taken at the first peaks, the troughs between the first peaks and the second peaks, and the second peaks.

Remarks: The location of the first peaks, the troughs between the first peaks and the second peaks, and the second peaks are marked by orange, green and blue arrows in Fig. 4.1 and 4.1 respectively.
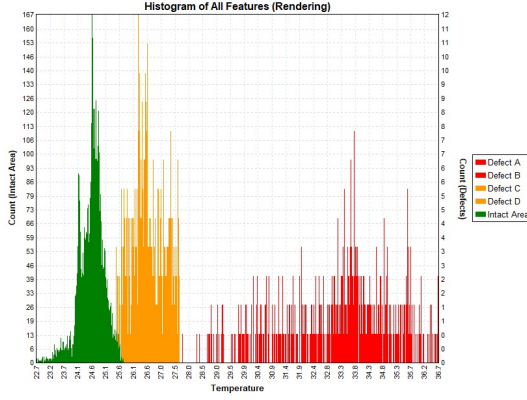
(a) Group 1 Material in the heat absorption period
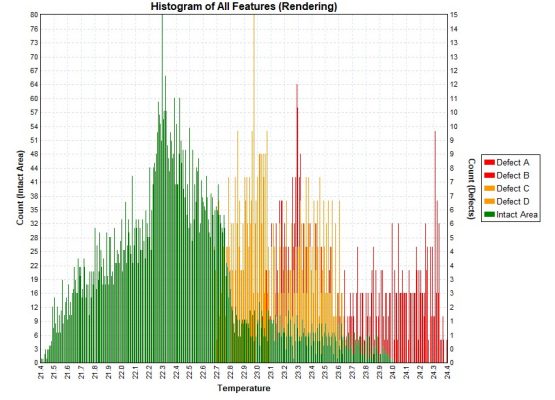
(b) Group 1 Material in the heat dissipation period
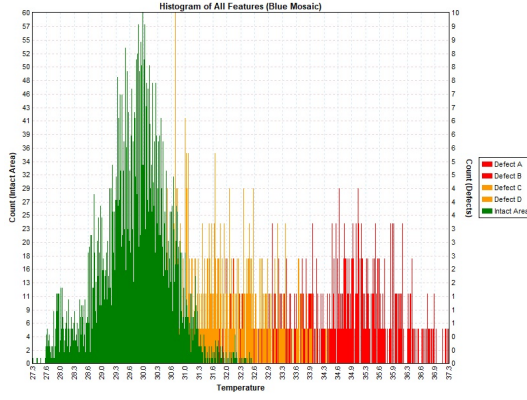
(c) Group 2 Material (Blue Mosaic) in the heat absorption period
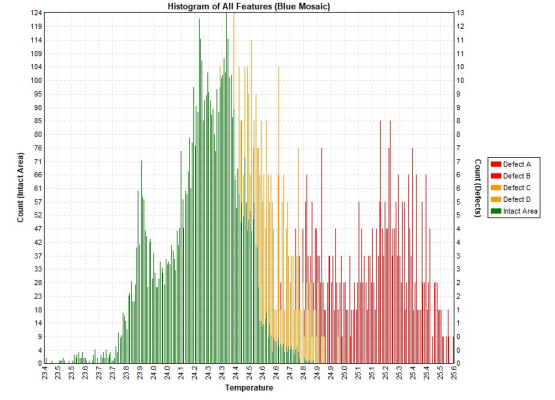
(d) Group 2 Material (Blue Mosaic) in the heat dissipation period
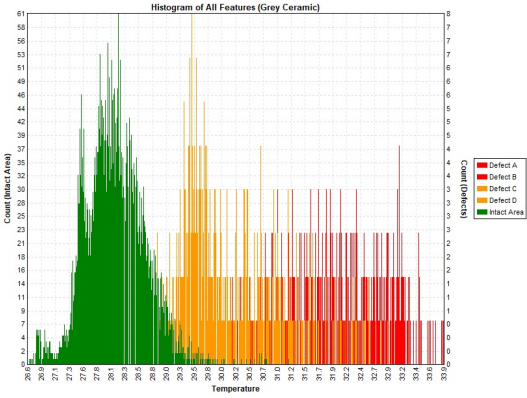
(e) Group 3 Material (Grey Ceramic) in the heat absorption period
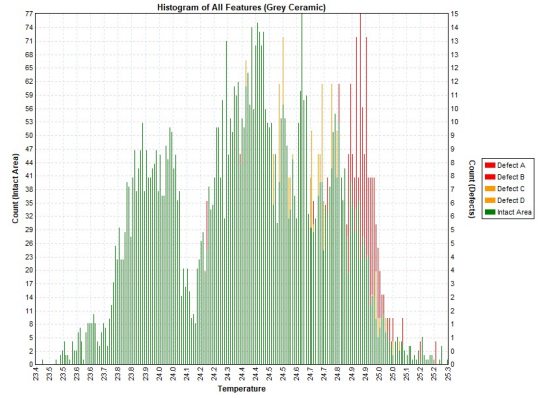
(f) Group 3 Material (Grey Ceramic) in the heat dissipation period

Figure 4.4: Selected histograms from each group in Shek Mun Day 1 dataset.

(a) Group 1 in Ping Che Day 2 dataset

(b) PolyU Position A dataset
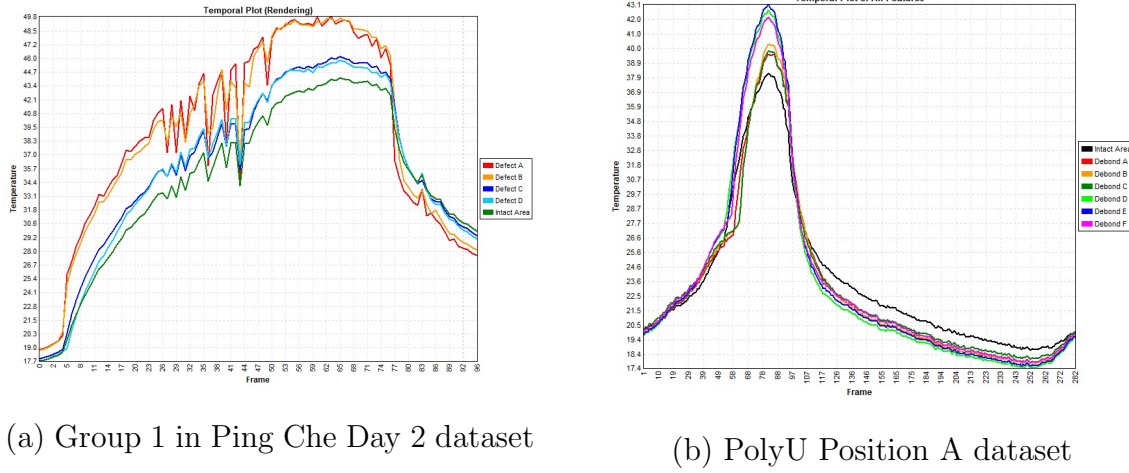
Figure 4.5: Temporal plots of wall finishes in Group 1 in Ping Che Day 2 dataset and PolyU Position A dataset.

Remarks: Frame in this plot can be converted to time, in which the starting times were 9:46 am (Ping Che) and 9:35 am (PolyU), and the images were taken at 5-min intervals. In the plot of PolyU Position A dataset, the sudden drop in the temperature curves occurred since the vision was blocked by the fabric of the tent.

4.3   Producing Thermal Decay Map

After selecting the suitable range of thermal images in each dataset, these thermal images in CSV format were imported into an in-house Python program for the creation of the Thermal Decay Map. The selected period and the number of thermal images used in each dataset for building inspection are summarized in Appendix A, and the source code is summarized in Appendix B. Since different wall finishes have their own physical and thermal properties, thermal decay maps were created in each wall finish material separately, and the ranges of thermal images were selected based on the types of wall finish material for building inspection. The resulting Thermal Decay Maps in each dataset are used in the discussion in Section 4.5.

4.4 Defect Classification

Adaptive thresholding and Otsu's thresholding, introduced in Section 3.2.1, were applied to the results to generate binary images showing defects. The resulting Thermal Decay Map in PolyU Position A dataset was used for an example in this section, and the ground truth image is presented in Fig. 4.8. For adaptive thresholding, since the embedded defects in the sample wall used in Shek Mun and Ping Che, and the embedded defects in the sample wall constructed in PolyU were in different sizes, the selected block sizes in each dataset are summarized in Table 4.1. Since the embedded defects were in different cover depths and resulted in the difference in thermal contrast between each defect and the intact area, the Thermal Decay Map and the ground truth image were cropped according to the location of each embedded defect, and then thresholding was applied to each embedded defect individually.

(a) Thermal Decay Map (b) Ground Truth
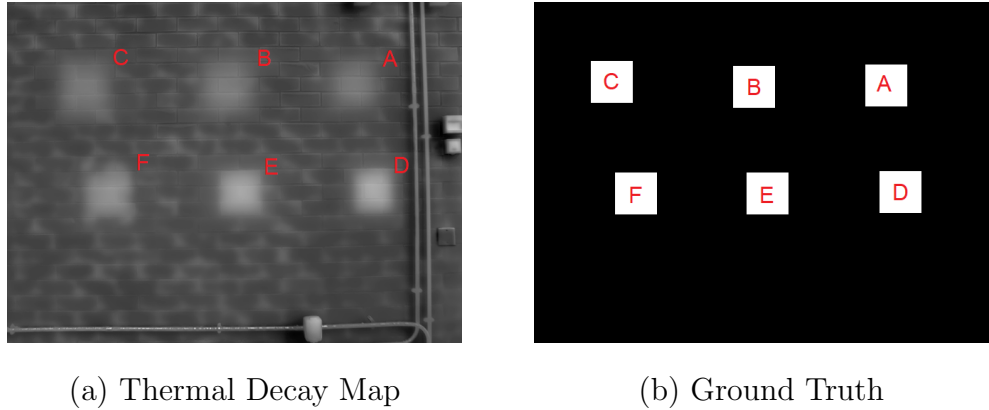
Figure 4.6: Thermal Decay Map and ground truth image of PolyU Position A Dataset.

Table 4.1: Selected Block Sizes for Adaptive Thresholding

Location of the dataset	3×3	25×25	57×57	479×479
Shek Mun	✓	✓		✓
Ping Che	✓	✓		✓
PolyU	✓		✓	✓

After generating a binary image, the binary image was then compared with the ground truth image, and a confusion matrix was calculated (discussed in Section 3.2.1) based on the comparison image. The binary images of each embedded defect in PolyU Position A dataset using Otsu's Thresholding and the comparison image are shown in Fig. 4.7. In the comparison image, the colour representation of TP, TN, FP and FN are white, black, green and blue respectively. Results in each dataset and further discussion are presented in Section 4.5.
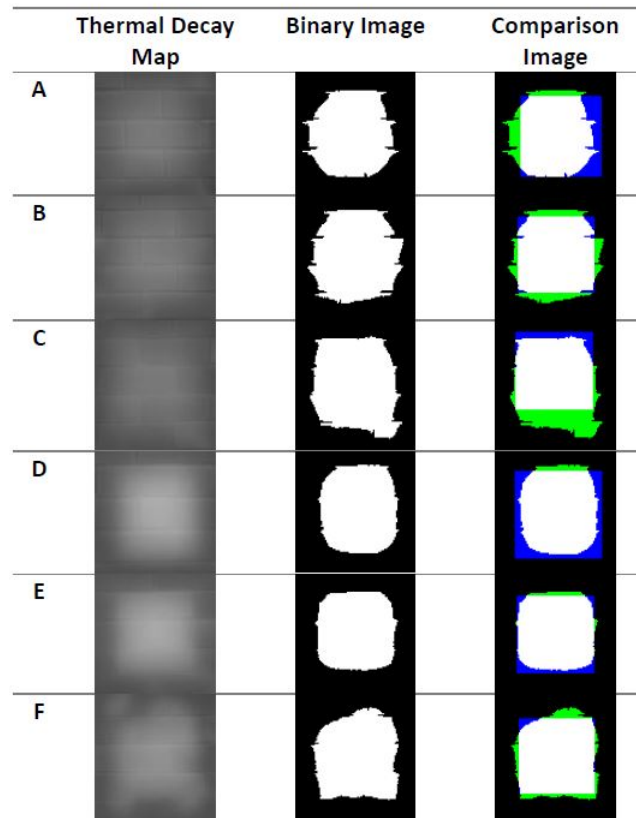
Figure 4.7: Summary of binary images and comparison images in PolyU Position A dataset.

4.5   Results and Discussions

Based on the results from the calculation of confusion matrix based on the comparison between the binary images generated from the Thermal Decay Maps and ground truth images of all datasets, various factors affecting the accuracy of the Thermal Decay Mapping method are summarized in the following subsections.

4.5.1   Performance of Thresholding Methods

To evaluate the performance of adaptive thresholding and Otsu's thresholding in this study, Shek Mun Day 1 dataset, in which one material was selected from each group, was selected for the discussion in this subsection. The comparison images between the binary images generated from the Thermal Decay Maps without enhancement and the ground truths in selected wall finish materials in Shek Mun Day 1 dataset are summarized in Fig. 4.8. The key point in defect size estimation is that the estimated size is in the correct shape, otherwise, the estimated value does not represent the true size correctly. From the figure, the binary results generated by adaptive threshold with 3×3 block size were highly affected by the patterns in the wall finishes materials (i.e. gaps between consecutive tiles), and hence the sizes of the defects embedded in light-coloured tiles from Group 3 would be underestimated (which the pixels within the defects were marked as false negative in blue colour) because of the emissivity. Binary results generated by adaptive threshold with 479×479 block size showed over-estimation in the sizes of the defects (in which the pixels outside the defects were marked as false positive in green colour) when the block size 479×479 was too large.

Accuracy and F1-score calculated from the comparison between the binary results generated by the proposed thresholding methods without applying SD enhancement and the ground truth are summarized in Table 4.2. The accuracy calculated

here is the pixel accuracy of the defect prediction, whether each pixel could successfully return the correct label (i.e. defect (in white colour) or no defect (in black colour). The accuracies and F1-scores of defect detection using adaptive thresholding with block size 25×25 are the highest among other adaptive thresholds with block sizes 3×3 and 479×479, and Otsu's threshold. However, this is because the sizes of the embedded defects were known in this study, and hence a suitable block size (25×25) could be applied, a matter of IFOV which is a variable in any survey. This could not be achieved in real cases as the sizes of the suspected defects are normally unknown. Therefore, Otsu's thresholding was selected in defect detection for the discussion in later sections of this chapter, since its accuracy is the second highest among the others, which are in ranges between 0.81 to 0.90, 0.80 to 0.85, and 0.72 to 0.84 for selected wall finish materials in Group 1, 2 and 3. Otsu's thresholding is the best choice because it eliminates the effects of changing kernel sizes on the accuracy and F1 score.

(a) Thermal Decay Map   (b) Ground Truth
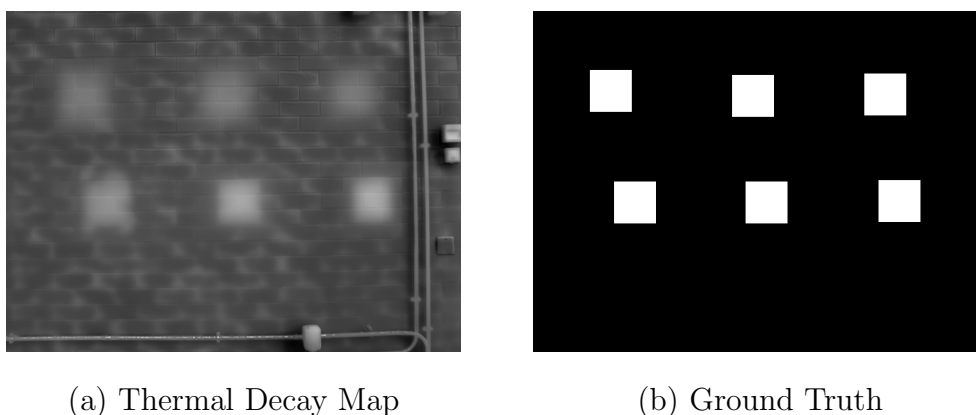
Figure 4.8: Binary images showing the prediction of PolyU Position A Dataset.

Table 4.2: Accuracy and F1-score of Defect Identification Using Proposed Thresholding on Selected Wall Finish Materials

Group	Material	Defect	Adaptive (3x3)		Adaptive (25x25)		Adaptive (479x479)		Otsu	
			Accuracy	F1-score	Accuracy	F1-score	Accuracy	F1-score	Accuracy	F1-score
1	Rendering	A	0.7421	0.7887	0.8981	0.9215	0.8492	0.9026	0.8558	0.8851
		B	0.7556	0.7796	0.8967	0.9038	0.6789	0.7854	0.8267	0.8271
		C	0.6177	0.6767	0.8729	0.8877	0.6510	0.7595	0.8177	0.8205
		D	0.6394	0.7315	0.8322	0.8699	0.6481	0.7661	0.9041	0.9163
2	Smooth Black	A	0.6056	0.5878	0.8966	0.9050	0.6218	0.7505	0.8341	0.8293
		B	0.6471	0.6554	0.8851	0.9022	0.7172	0.8113	0.8356	0.8464
		C	0.5125	0.5366	0.8552	0.8631	0.6115	0.7393	0.8083	0.7969
		D	0.5828	0.6559	0.7977	0.8412	0.6483	0.7757	0.8149	0.8332
3	White Mosaic	A	0.5565	0.5959	0.8859	0.9066	0.7241	0.8188	0.8252	0.8411
		B	0.5792	0.6061	0.8560	0.8744	0.6362	0.7645	0.8047	0.8066
		C	0.6042	0.5957	0.8292	0.8479	0.5990	0.7332	0.8406	0.8428
		D	0.5558	0.5024	0.6797	0.6783	0.6580	0.7220	0.7619	0.7179

4.5.2 Physical and Thermal Properties of Wall Finish Materials

Unlike concrete bridge deck inspection, inspection on external walls of a building involves numerous kinds of wall finish materials, including rendering and ceramic tiles. In this study, a sample wall with 8 different wall finish materials was constructed. These 8 types of wall finish materials are in different sizes, colours and textures, which the details were summarized in the previous section (Section 3.4.1). Shek Mun Day 1 dataset was selected for the discussion in this subsection as the sample wall was arranged to face towards the East which received direct solar radiation.

The Thermal Decay Maps of each wall finish material in Shek Mun Day 1 dataset are summarized in Fig. 4.9. From the thermal decay maps, shallow defects (i.e. Defects A and B) can all be identified by the naked eye, while deep defects (i.e. Defects C and D) are much clearer in Group 1 and 2 materials. Group 1 consists of rendering only, and Group 2 consists of Blue Mosaic tiles, Smooth Black tiles and

Matt Black tiles. Accuracy and F1-score calculated from the comparison between the binary results generated by Otsu's Thresholding without applying SD enhancement and the ground truth are summarized in Table 4.3. The accuracies of all four defects in Group 1 are in a range between 0.81 and 0.90, while the accuracies of all four defects in Group 2 and 3 are in ranges between 0.71 and 0.89, and between 0.61 and 0.84 respectively.

Table 4.3: Accuracy and F1-score of Defect Identification on Different Types of Wall Finish Materials

Group	Material	Defect	Accuracy	F1-score	Group	Material	Defect	Accuracy	F1-score
1	Rendering	A	0.8558	0.8851	3	Grey Ceramic	A	0.8287	0.8386
		B	0.8267	0.8271			B	0.8333	0.8181
		C	0.8177	0.8205			C	0.7488	0.7549
		D	0.9041	0.9163			D	0.6232	0.6030
2	Blue Mosaic	A	0.7615	0.7887	3	Reflective White	A	0.7461	0.7550
		B	0.8583	0.8412			B	0.8078	0.8265
		C	0.8023	0.8063			C	0.7146	0.6819
		D	0.7702	0.7564			D	0.6086	0.6829
2	Smooth Black	A	0.8341	0.8293	3	White Mosaic	A	0.8252	0.8411
		B	0.8356	0.8464			B	0.8047	0.8066
		C	0.8083	0.7969			C	0.8406	0.8428
		D	0.8149	0.8332			D	0.7619	0.7179
2	Matt Black	A	0.8857	0.8599	3	Mixed Mosaic	A	0.7763	0.8317
		B	0.8276	0.8072			B	0.7705	0.7789
		C	0.7360	0.7784			C	0.7292	0.7666
		D	0.7132	0.7483			D	0.7631	0.7756

In the part with Group 1 materials, the surface above the embedded defects was rendering only and without any wall tiles, where k_x, k_y, and k_z in Eq. 2.3 are the same and the host materials are thermally homogeneous in all directions except for the defect. Hence it resulted in high thermal contrast between the defect area and the intact area. Group 2 materials are materials in dark colours, hence they had higher emissivities than Group 3 materials which are light-coloured materials. The thermal conductivity of cementitious render is 1.16 W m^{-1} K^{-1} [49] and that of

ceramic tiles is between 0.6 and 1.7 W m^{-1} K^{-1} [163]. According to Eq. 2.3, a higher value for thermal conductivity k allows greater heat transfer through the medium. Hence, more heat can be transferred through a mosaic-covered wall than through a ceramic-covered wall. A similar phenomenon, which occurs for the same reason, can be seen when White Mosaic tiles and White Ceramic tiles in Group 3 are compared, with the accuracy of defect detection in White Mosaic tiles having a higher range (0.76 to 0.83) than that in White Ceramic tiles (0.61 to 0.75).

Comparing Group 2 (dark-coloured tiles) with Group 3 (light-coloured tiles), the latter gives a lower emissivity and higher reflectance than the former. According to Eq. 2.11, this makes Group 3 materials reflect more incident radiation than those in Group 2. In other words, dark colours with higher thermal absorptivity as a result of higher emissivity absorb more incident radiation, producing a hotter surface temperature and therefore a larger thermal contrast [164], which in turn favours defect detection. Hence, the accuracy of defect detection in Group 2's dark-coloured walls is generally higher than in light-coloured walls.

The embedded defects on the sample wall were divided into two groups, including shallow defects (Defect A (5mm) and B (8mm)) and deep defects (Defect C (15mm) and D (17mm)). From Table 4.3, the accuracies of defect detection in shallow defects were all greater than 0.74. For the deep defects, the accuracy of defect detection was relatively low, falling within a range from 0.60 to 0.84, except for Group 1 material (i.e. rendering). This phenomenon was addressed in the previous subsection.

(a) Rendering (0.5SD)

(b) Blue Mosaic Tiles (1.5SD)

(c) Smooth Black Tiles (1.5SD)

(d) Matt Black Tiles (1.5SD)

(e) Grey Ceramic Tiles (1.5SD)

(f) Reflective White Tiles (1.5SD)

(g) White Mosaic Tiles (1.5SD)

(h) Mixed Mosaic Tiles (1.5SD)
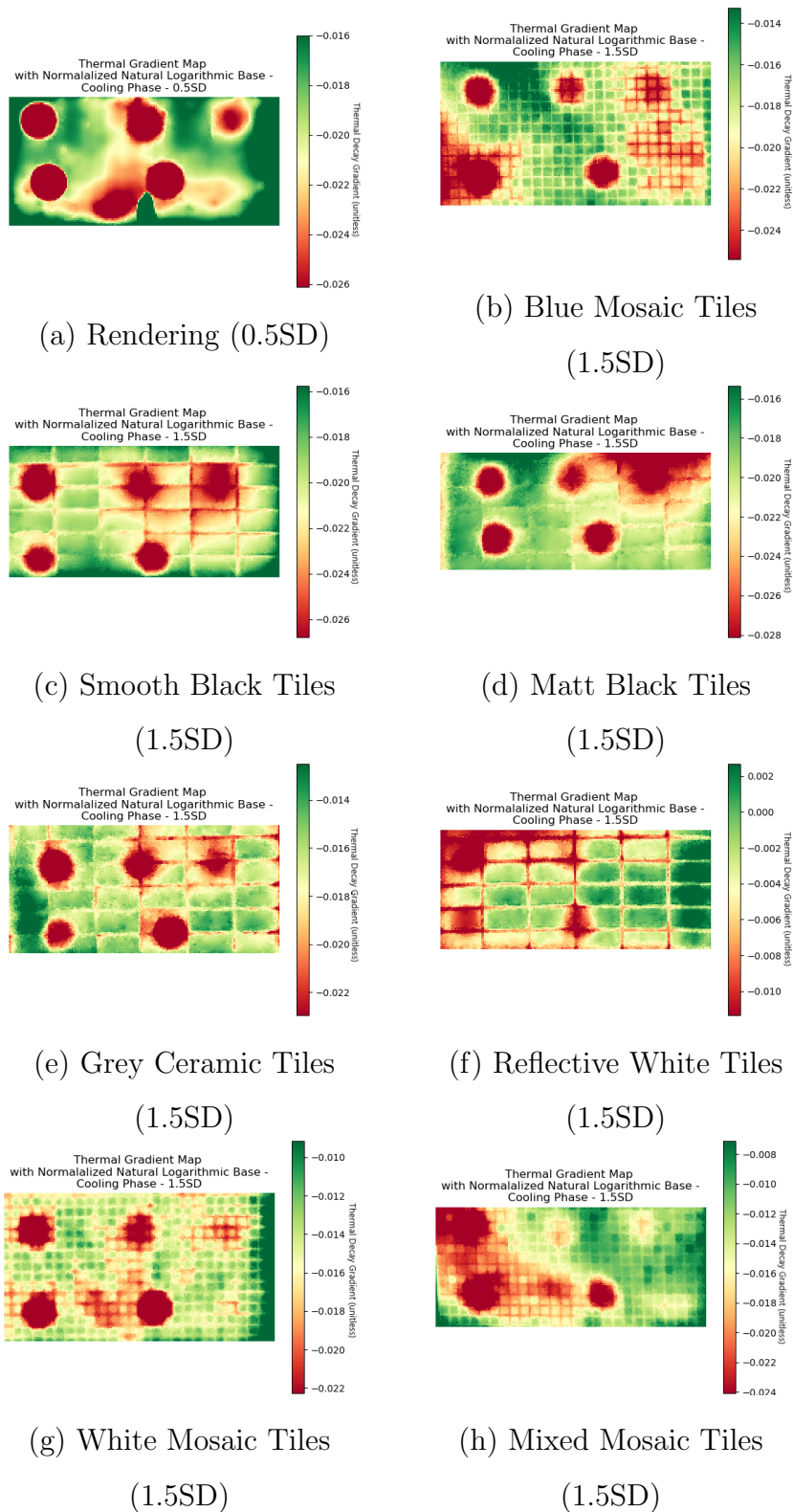
Figure 4.9: Thermal Decay Map of each wall finish materials with SD enhancement in Shek Mun Day 1 dataset.

Overall, defect detection at shallower cover depths had a higher accuracy than that for defects in deep cover depths. There could be two reasons accounting for this phenomenon. Firstly, when the distance between the wall surface and the defect area increases, the heat energy of the incident radiation experiences greater thermal absorption by the material composites due to the longer path length z in Eqs. 2.2 and 2.3. Secondly, the incident radiation experiences omnidirectional dispersion along the lateral x and y directions at different rates of thermal transfer k_x and k_y in Eqs. 2.2 and 2.3. Hence the defects at shallower cover depths accumulated more heat energy than those at greater cover depths due to the relatively limited impact of the above negative effects. The shallow defects thus acquired a hotter temperature (i.e. a higher thermal contrast), which enhanced their detectability by the infrared camera and also favoured defect detection according to Eqs. 2.10 and 2.11, respectively.

4.5.3 Orientation of Building

The orientation of the target surface determines the starting frame when adopting the Thermal Decay Mapping method. The sample wall in Shek Mun dataset was arranged to face towards the East, and therefore the heat absorption period and the first peak occurred in the morning session (Fig. 4.1 and 4.2). The occurrence of the second peak was explained in the previous section (Section 4.2). Although the sample walls in Ping Che and PolyU were arranged to face towards the South and Northwest respectively, the first peak occurred in the afternoon session (Fig. 4.5). This shows a shift of the heat absorption period and the first peak.

The summary of the resulting Thermal Decay Maps and the comparison images of Group 1 material in selected datasets is presented in Fig. 4.10. Table 4.4 summarizes the accuracies and F1-scores calculated from the comparison between the binary results on Group 1 material (i.e. rendering) generated by Otsu's thresholding methods without applying SD enhancement and the ground truth. The accuracies and

F1-scores of defect detection on rendering are all above 0.8, which are independent of the cover depths of the defects.
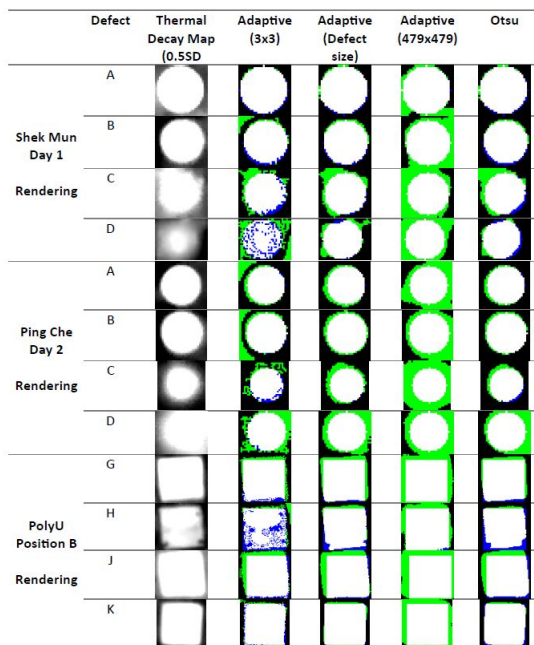
Figure 4.10: Thermal Decay Maps and comparison images of Group 1 material (Rendering) in selected dataset.

Remarks: Details of the cover depths of the embedded defects can refer to Fig. 3.6 and Table 3.6.

Table 4.4: Accuracy and F1-score of Defect Identification on Rendering

Group	Material	Defect	Accuracy	F1-score
Shek Mun	Rendering	A	0.8558	0.8851
Day 1		B	0.8267	0.8271
(Facing East)		C	0.8177	0.8205
		D	0.9041	0.9163
Ping Che	Rendering	A	0.9029	0.8889
Day 2		B	0.8395	0.8163
(Facing South)		C	0.9011	0.8639
		D	0.8161	0.8396
PolyU	Rendering	G	0.8776	0.9091
Position B		H	0.8551	0.8941
(Facing Northwest)		J	0.8128	0.8589
		K	0.9203	0.9409

4.5.4 Enhancement by Pixel's Standard Deviation (SD method)

Although the accuracies and F1-scores of defect detection on different wall finish materials using the Thermal Decay Maps without any alteration are all above 0.8, they can be improved by enhancing the original Thermal Decay Maps by the SD method. In the original Thermal Decay Map, the values of the maximum and minimum thermal decay gradient within the ROI are used as the range of colour representation. Standard deviation (SD) of all the thermal decay gradients within the ROI can be added to both the maximum and minimum thermal decay gradient values as the range of colour representation to enhance the Thermal Decay Maps. Fig. 4.11 shows the enhanced Thermal Decay Maps of Group 1 material in Shek Mun Day 1 dataset by the SD method, ranging from 0.5SD to 3.5 SD. By adding 0.5SD to the maximum and minimum thermal decay gradient values used in the colour representation, defects in shallow and deep cover depths can be shown clearly in the resulting enhanced Thermal Decay Map. However, the enhancement also enhanced the natural defect formed at the bottom when the sample wall existed in a prolonged outdoor environment. When the number of SD increases in the enhancement by the SD method, defects in deep cover depths gradually disappear. Therefore, this suggests the optimal number of SD should be selected during the enhancement by the SD method.
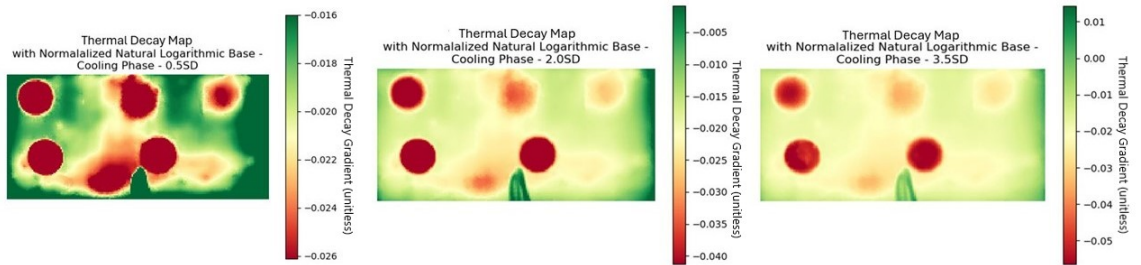
Figure 4.11: Enhancement of Group 1 material in Shek Mun Day 1 dataset by SD method.

Fig 4.12, 4.13 and 4.14 summarize the accuracies and F1-scores calculated from the comparison between the binary results of Defect A on selected wall finishes material in all groups generated by Otsu's thresholding methods and the ground truth from Shek Mun Day 1 dataset respectively. For Group 1 material, the accuracy and f1-score could be improved, which were above 0.9, by adding 0.5SD in the range of colour representation of the Thermal Decay Maps. For Group 2 and 3 material, the accuracy and f1-score could be improved by adding 1.5SD in the range of colour representation of the Thermal Decay Maps. This showed the benefits of enhancement by the SD method.

(a) Accuracy   (b) F1-Score
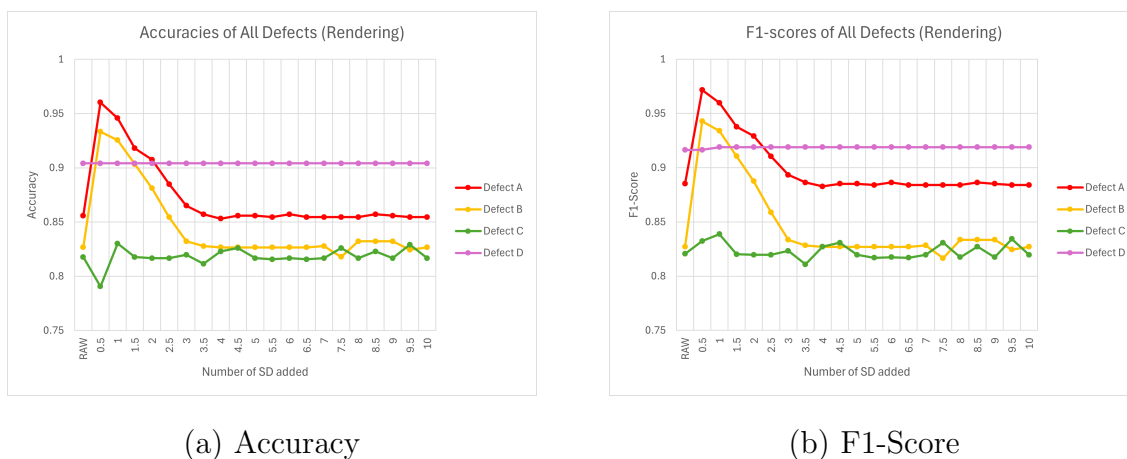
Figure 4.12: Accuracies and F1-Scores of Group 1 material in Shek Mun Day 1 dataset.
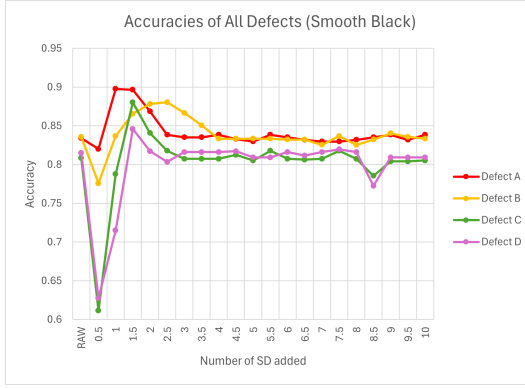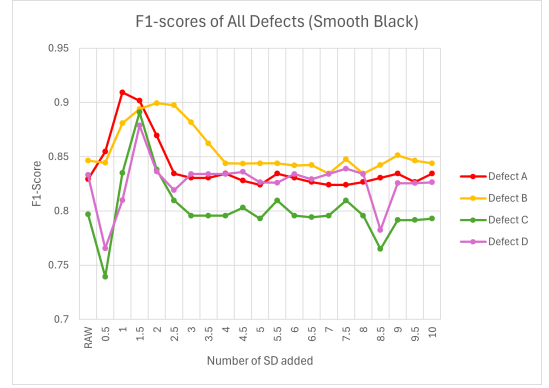
(a) Accuracy

(b) F1-Score

Figure 4.13: Accuracies and F1-Scores of Group 2 material (Smooth Black tiles) in Shek Mun Day 1 dataset.
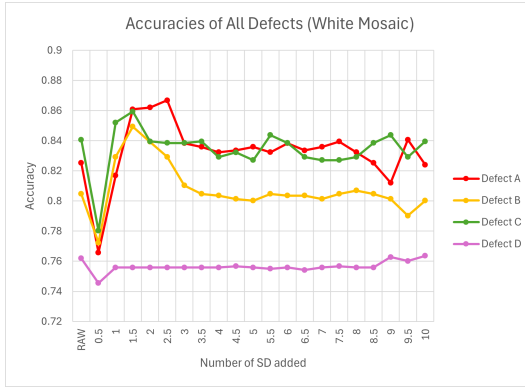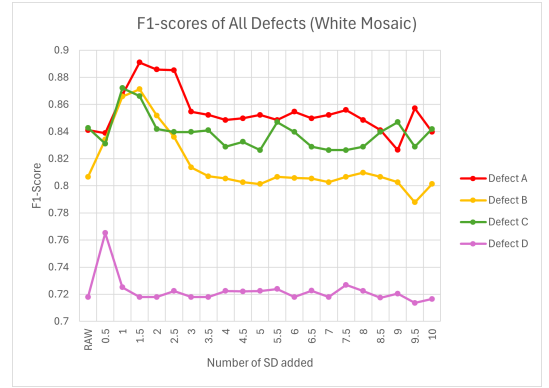
(a) Accuracy

(b) F1-Score

Figure 4.14: Accuracies and F1-Scores of Group 3 material (White Mosaic tiles) in Shek Mun Day 1 dataset.

4.6 Chapter Summary

The proposed Thermal Decay Mapping method was applied to datasets consisting of different wall finish materials and orientations. The results of adopting the proposed method were summarized in this chapter, which fulfilled the three objectives

proposed in this study. The embedded defects in each sample wall were visualized in binary images generated from the Thermal Decay Maps, and fulfilled part of Objective 1, which is to classify subsurface defects in building structures. Different factors affecting the accuracy of the Thermal Decay Mapping method were summarized and discussed in this chapter (Section 4.5), which included the selection of thresholding methods to be performed on the Thermal Decay Maps for generating binary images (Section 4.5.1), the physical and thermal properties of different wall finishes materials (Section 4.5.2), the orientation of the target surface (i.e. building) (Section 4.5.3) and the enhancement in defect identification by SD method (Section 4.5.4). This fulfilled part of Objective 2. The performance of the proposed Thermal Decay Mapping method was evaluated by the calculation of a confusion matrix. The binary images containing the suspected defects were compared with the ground truth image, and hence the number of TP, TN, FP and FN could be retrieved. These numbers were used for the calculation of accuracies and F1-scores for assessing the performance of the proposed method, which fulfilled part of Objective 3.

To summarize, this study validated the possibility of adopting the Thermal Decay Mapping method in building inspection, in which the average accuracy of the defect detection could be above 0.8, which depends on the types of wall finish materials and the orientation of the target surface. Based on the results presented in this chapter, it is suggested to adopt Otsu's thresholding method to generate binary images from the resulting Thermal Decay Maps since it does not require manual selection of the "suitable" block size (i.e. the size of the defect), as in adaptive thresholding method, to obtain optimal threshold values and the size of the defect is unknown in the field. To improve the accuracy of defect detection by adopting the proposed method, it is suggested to add 0.5SD and 1.5SD in the ranges of colour representation of the resulting Thermal Decay Maps before generating the binary images when dealing with external walls covered with rendering and tiles respectively. The results showed that a time-lapse IRT survey using the Thermal Decay Method

could provide quantitative results of the suspected defects, which is a significant improvement in building external wall diagnosis.

Chapter 5

Thermal Image Processing by Physical Approach (Thermal Decay Mapping) - Secondary Landslide Hazard Inspection

5.1   Chapter Overview

This chapter summarizes the results of feature classification on natural terrain by adopting the Thermal Decay Mapping method. The characteristics of each dataset such as histograms and temporal plots of each material are presented. The requirements for the selection of suitable thermal images of the target slope are discussed. Results and discussions for secondary landslide hazard inspection are summarized, including the factors affecting the feature classification results.

98

5.2 Thermal Data Preparation

Following the general workflow summarized in Section 3.2.1, the first step is thermal data preparation. Since the Thermal Decay Mapping method studies the temperature distribution of the target surface in the heat dissipation period, it is necessary to study the temporal plot of all the features on the target surface to determine the starting frames to be adopted in data processing. The datasets used in this chapter included the datasets collected in High Island Reservoir and Sai Wan Road for secondary landslide hazard inspection, which the details were described in Section 3.4.2.

The temporal plots of all features on the slope in High Island Reservoir dataset and Sai Wan Road dataset were presented in Fig. 5.1 and Fig. 5.2 respectively, which the dataset collected in High Island Reservoir was used for the explanation in this section. The features identified on the target surface include vegetation, fine ash tuff in weathering grades 3 and 4 to 5, basalt dyke and faults. The grading in weathering was based on the definitions provided by the Geotechnical Engineering Office [165], which is summarized in Table 5.1. From the temporal plots, the peaks of all features occurred at the frame numbers ranging from 35 to 46 (i.e. 2:30 pm to 3:25 pm). The range of temperatures of vegetation within the whole period is the narrowest, which is between 30.19℃and 34.05℃, and the range of temperatures of fine ash tuff in weathering grades 4 to 5 is the widest, which is between 41.82℃and 33.94℃. To study the thermal behaviours of all features, histograms of all features were presented in Fig. 5.3. In the histograms, the colour representation of vegetation, fine ash tuff in weathering grade 3, fine ash tuff in weathering grades 4 to 5, basalt dyke and faults are green, brown, pink, black and orange respectively. During the heat absorption period, vegetation can be separated from other features while other features are all overlapped with each other. During the heat dissipation period, the distribution of vegetation further separates from the other features, while fresh ash tuff in weathering

grades 4 to 5 can be separated from the remaining features. Fig. 5.4 shows the Thermal Decay regression plots in a natural logarithmic base of all features in Sai Wan Road dataset, which proves that thermal decay gradient can be used in slope feature classification. In these thermal decay regression plots, both temperature and time of the selected features were normalized in natural logarithmic base and plotted (which are shown as points in the figure). The lines of linear regression were then plotted and the coefficients of the regression line were retrieved, which are the thermal decay gradients. This shows the potential of feature classification using IRT since the distributions of vegetation and fresh ash tuff in weathering grades 4 to 5 allow feature segmentation. Therefore, as the temperature distribution of the target surface in the heat dissipation period (unlike in building envelope) is the main focus of the Thermal Decay Mapping method, thermal images within the heat dissipation period, starting from the peak to the end of the whole period in the dataset were used for producing thermal decay maps in later sections.
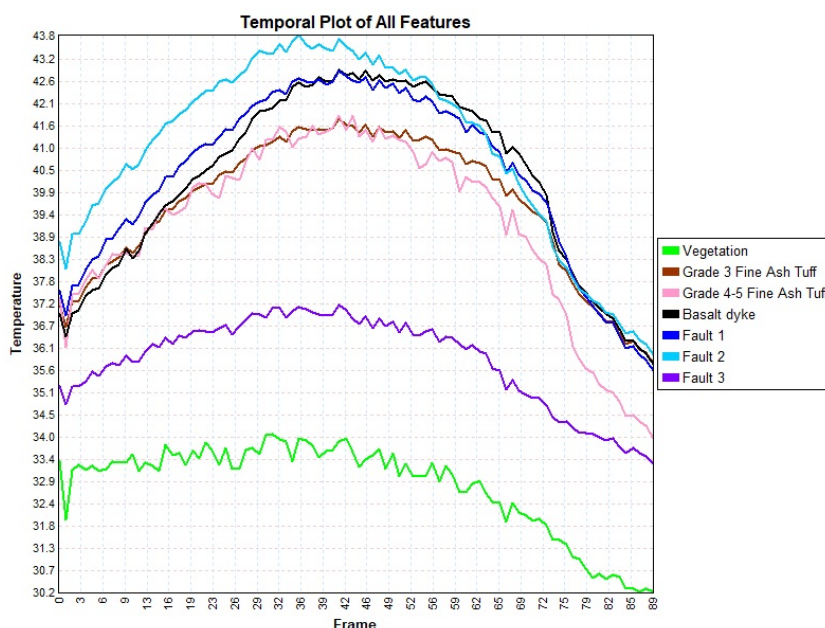
Figure 5.1: Temporal plots of all features on the slope in High Island Reservoir dataset.

Remarks: Frame in this plot can be converted to time, in which the starting time was 11:41 am, and the images were taken at 5-min intervals.
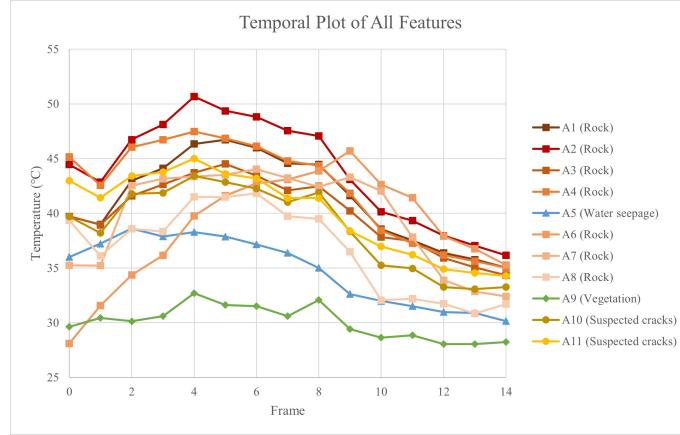
(a) Part 1
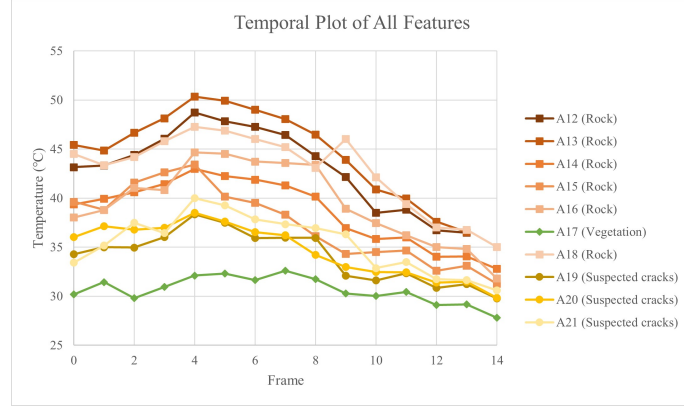
(b) Part 2

Figure 5.2: Temporal plots of all features in Sai Wan Road dataset.

Remarks: Frame in this plot can be converted to time, in which the starting time was 10:58 am, and the images were taken at 30-min intervals.

Table 5.1: Definitions of weathering grades [165]

Grade	Definition
V (Completely Decomposed)	The original rock texture is preserved. The rocks can be crumbled by hand and finger pressure into constituent grains, and it can be easily indented by point of geological pick. The sample can be slaked in water.
IV (Highly Decomposed)	The rocks are completely discoloured when compared with fresh rock. The rocks can be broken by hand into smaller pieces. A dull sound can be heard when the rocks are struck by hammer, and it cannot be easily indented by point of geological pick. The sample cannot be slaked in water. The rocks are completely discoloured when compared with fresh rock.
III (Moderately Decomposed)	The rocks cannot be broken by hand, but can be easily broken by hammer. A dull or slight ringing sound can be heard when the rocks are struck by hammer. The rocks are completely stained throughout.

101

(a) During the heat absorption period

(b) During the heat dissipation period
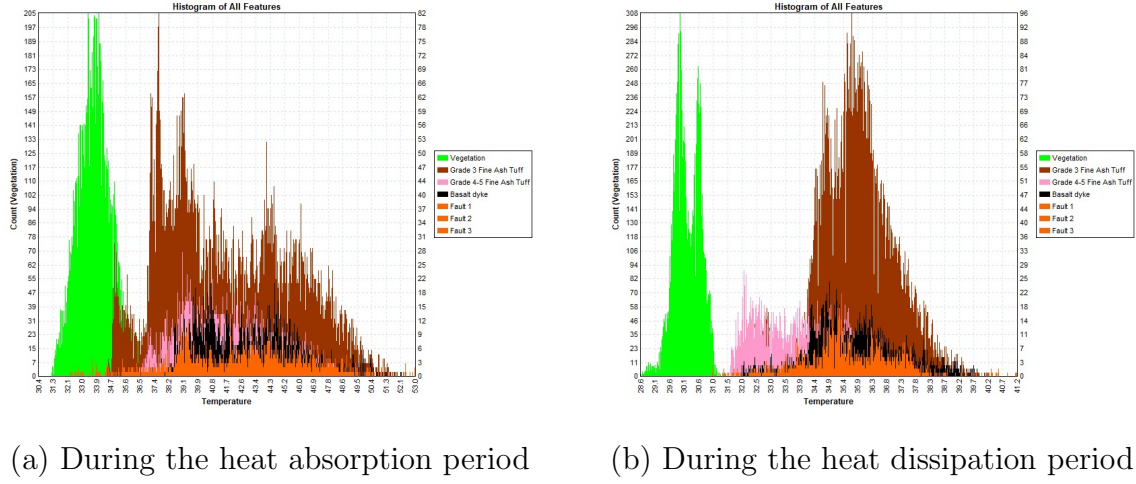
Figure 5.3: Selected histograms of all features in High Island Reservoir dataset.

(a) Part 1 - Rocks

(b) Part 1 - Moisture, Cracks and Vegetation

(c) Part 2 - Rocks

(d) Part 2 - Cracks and Vegetation
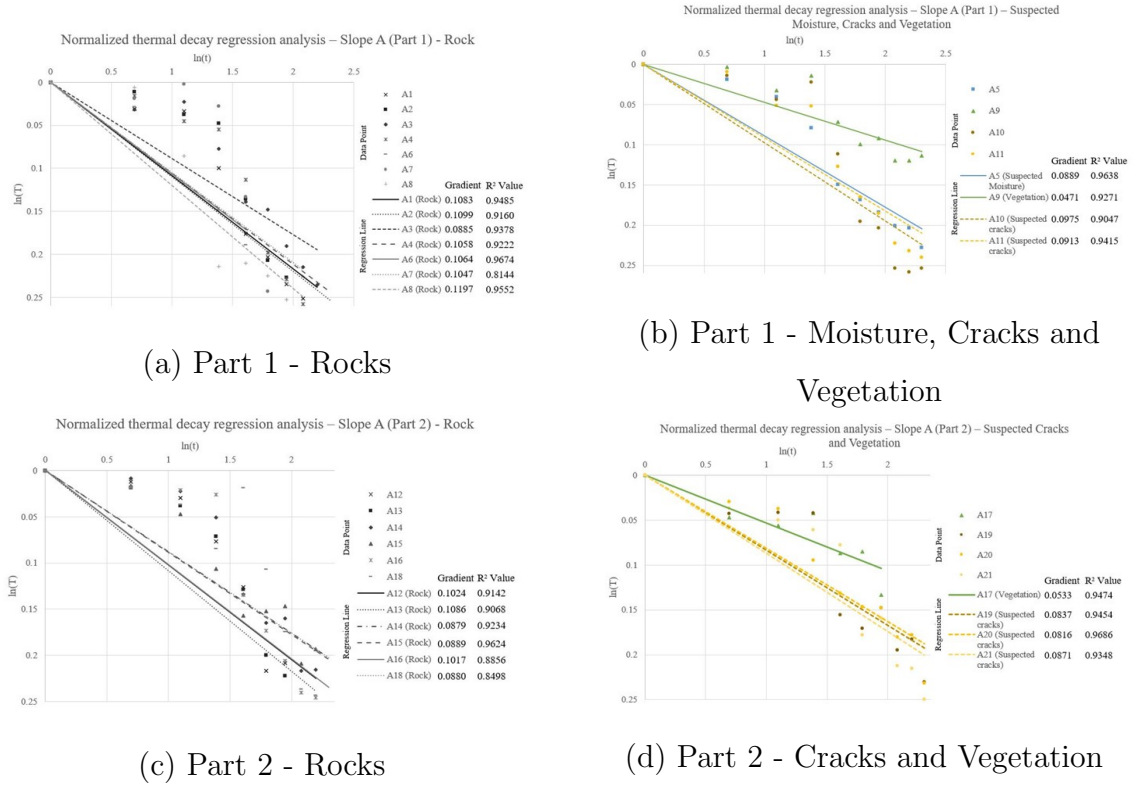
Figure 5.4: Thermal decay regression plots in a natural logarithmic base of all features in Sai Wan Road dataset. [44]

Remarks: The gradient values in the plots are absolute values.

5.3 Producing Thermal Decay Map

After selecting the suitable range of thermal images in each dataset, these thermal images in CSV format were imported into a dedicated Python program for the creation of the Thermal Decay Map. The selected period and the number of thermal images used in each dataset for secondary landslide hazard inspection are summarized in Table 5.2. Since the thermal images in Sai Wan Road dataset were collected by a UAS equipped with a thermal camera, the thermal images needed to be registered, which was explained in Section 3.2.1 in the previous chapter. For secondary landslide hazard inspection, all the features used the same range of thermal images to produce a single Thermal Decay Map for the whole target surface. The resulting Thermal Decay Maps in each dataset are presented in Section 5.5.

Table 5.2: Summary of thermal images used for the creation of Thermal Decay Maps in High Island Reservoir and Sai Wan Road dataset

Dataset	Starting Frame (Time)	Ending Frame (Time)	Number of thermal images
High Island Reservoir	37 (2:41pm)	90 (7:06pm)	54
Sai Wan Road	5 (1:00pm)	15 (6:00pm)	11

5.4 Feature Classification

The resulting Thermal Decay Maps were segmented according to their histograms to generate feature classification images. The histograms of the resulting Thermal Decay Maps using High Island Reservoir dataset and Sai Wan Road dataset are presented in Fig. 5.5 and 5.6 respectively. The selected ranges of the thermal decay gradient shown in the figures were selected by the clusters in the histograms, in which each range was sectioned at the troughs between two consecutive clusters, and were used for feature segmentation. The feature classification images will be

presented in a later section in this chapter. In High Island Reservoir, the target slope is located in a UNESCO Global Geopark, where the slope is under the protection of laws and contact inspection is prohibited. The target slope in Sai Wan Road was inaccessible during the data collection period, and the target slope could be inspected by UAS only. Hence, there was no ground truth data that could be obtained from both datasets. To evaluate the performance of the proposed Thermal Decay Method, the results including the resulting Thermal Decay Map and the feature classification images were compared with findings in the GEO reports published by the HKSAR government, previous research in [44, 101], visual images and raw thermal images, which the results and discussion are summarized in Section 5.5.
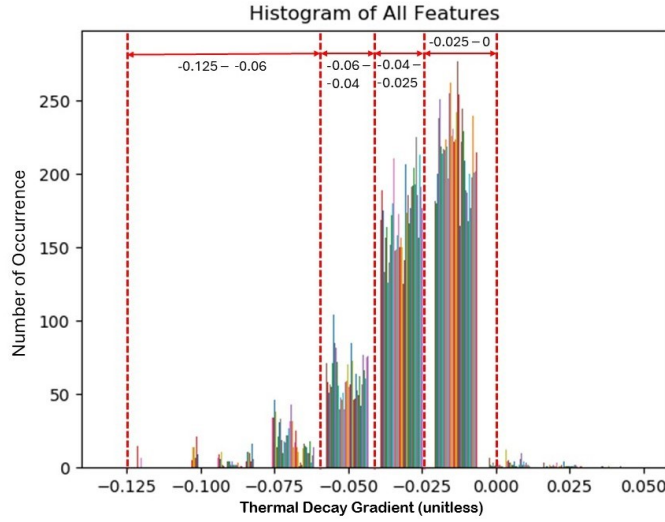
Figure 5.5: Histogram of all features and the selected ranges for segmentation in High Island Reservoir dataset.

(a) Part 1   (b) Part 2
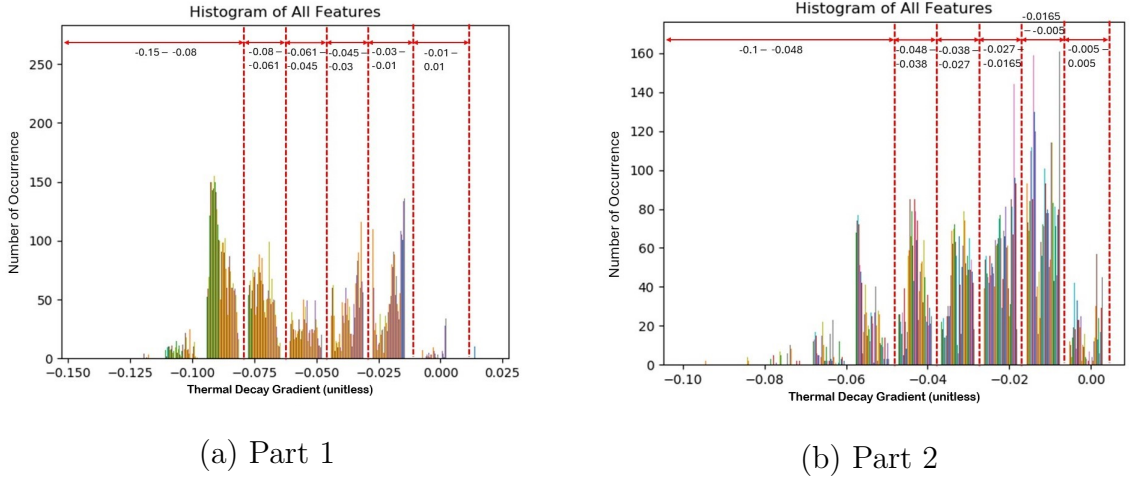
Figure 5.6: Histogram of all features and the selected ranges for segmentation in Sai Wan dataset.

5.5 Results and Discussions

All of the Thermal Decay Maps and feature classification images of all datasets are summarized in Fig. 5.7 and 5.8. The colour representations in each feature classification image are not the same representation, and the ranges of the assigned colours depend on the thermal decay gradient values within the ROI in each Thermal Decay Map. In Fig. 5.7, the hexagonal columns were segmented in brown and yellow colour, depending on the direction the surface is facing towards, while soil and vegetation on the ground that received direct sunlight at any time were segmented in black and dark blue colour. For Fig. 5.8, further colour representations are discussed in Section 5.5.4. Based on the results, various factors affecting the accuracy of the Thermal Decay Mapping method on secondary landslide hazard inspection are summarized in the following subsections.
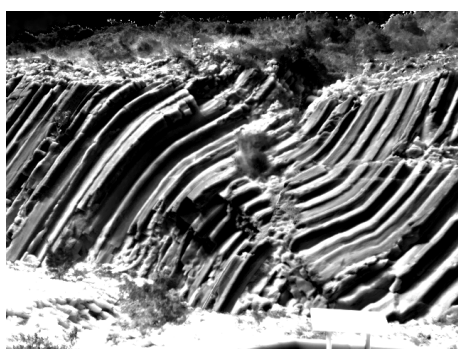
(a) High Island Reservoir -

Thermal Decay Map (1 SD)
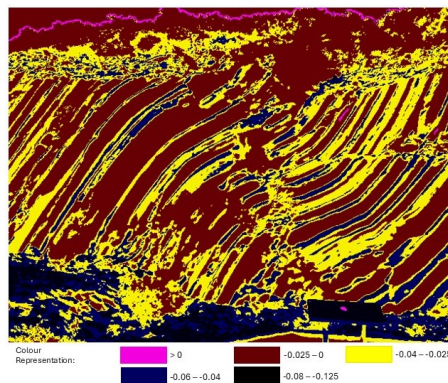
(b) High Island Reservoir -

Feature Classification

Figure 5.7: Thermal Decay Maps and feature classification images generated from High Island Reservoir dataset.

5.5.1   Image Enhancement in Thermal Dataset

The time-lapse IRT survey with the aid of UAS is the first study adopted in Hong Kong, while no standard regarding the application of the IRT survey on slopes is present in the field. This means unlike IRT applied to building envelope inspection, there is no guideline on the adjustment of a suitable temperature span in the thermal images when performing secondary landslide hazard inspection. Similar to building inspection using snapshot IRT, features on the slope can be hidden or exaggerated by an unsuitable choice of temperature span. The timing for capturing the thermal image for inspection affects the detectability of the features on a slope. Human bias could be a source of error since the optimal time for capturing a single thermal image in a snapshot IRT survey depends on the experience of the operators. If a thermal image is captured at a time when insufficient solar radiation can be absorbed, this results in insufficient thermal contrast between hidden features such as moisture and faults, and the intact area and lowers the detectability of the hidden features. In this study, this limitation can be eliminated by adopting the time-lapse IRT and Thermal Decay Mapping method following the same fashion as in Chapter 4. Fig.

106
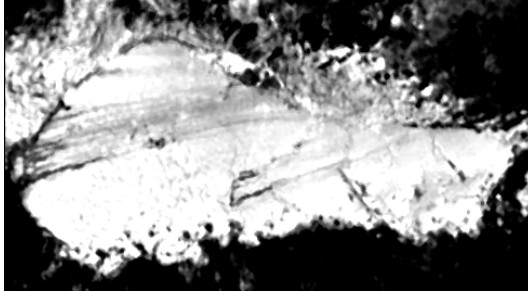
(a) Sai Wan Road Part 1 - Thermal
Decay Map (1 SD)
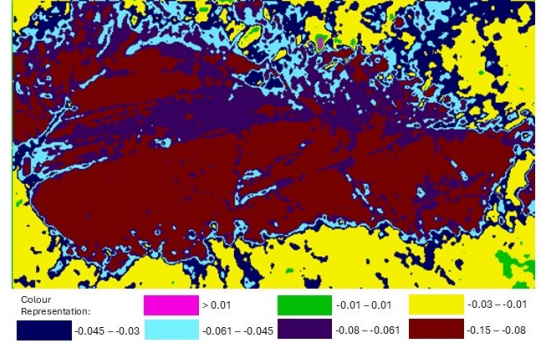
(b) Sai Wan Road Part 1 - Feature
Classification
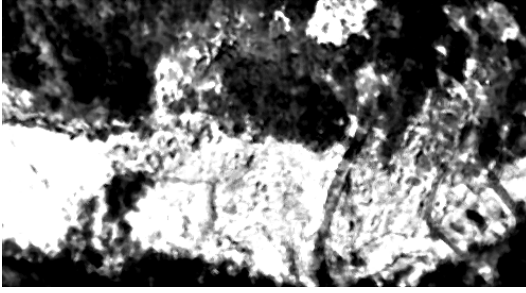
(c) Sai Wan Road Part 2 - Thermal
Decay Map (1 SD)
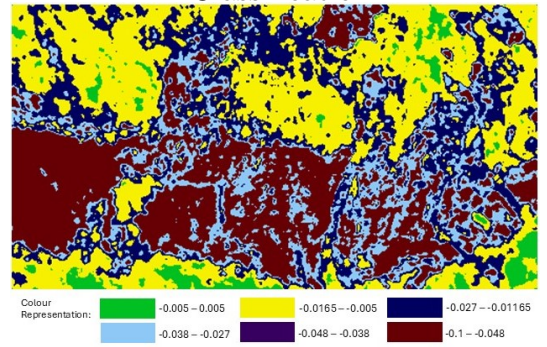
(d) Sai Wan Road Part 2 - Feature
Classification

Figure 5.8: Thermal Decay Maps and feature classification images generated from Sai Wan Road dataset.

5.9 shows the visual image of a slope, the corresponding thermal image collected by snapshot IRT without any alterations, the Thermal Decay Map and the feature classification image generated by the proposed method in this study. The features identified in the resulting Thermal Decay Map matched with the results reported in [44, 101], in which several faults/cracks and moisture patches were suspected in the landslide scar. These identified features were shown prominently in the feature classification image, while only vegetation could be classified in the visual image. The results showed that with the aid of an IRT survey, potential weakening areas like faults or cracks can be identified. Although these hidden features could be identified

107

in both the raw thermal image and the Thermal Decay map, the time at which the optimal thermal image for effective feature identification is unknown. Snapshot IRT survey has a risk of capturing a single thermal image at the wrong time when the thermal contrasts between features are insufficient. Time-lapse IRT inspection using the proposed Thermal Decay Mapping method does not have this limitation since time-lapse IRT considers the whole time period during analysis, and the Thermal Decay Map is produced by a sequence of thermal images. Further, the calculation of the ratio of the classified features on the slope could be possible, which could be calculated by the number of pixels in the same colour to the number of pixels within the ROI (i.e. the slope surface). This shows that adopting the Thermal Decay Mapping method can improve the performance of feature identification in secondary landslide hazard inspection.

5.5.2   Orientation and Roughness of Rock Slope

For a successful material classification with time-lapse IR, the results in this study show that the orientation of the target slope could be one of the factors affecting the success of feature detection and classification in secondary landslide hazard inspection. Orientation of the target slope facing either East or West facilitates more heat energy being transferred to the target slope. The target slope in High Island Reservoir dataset faces towards the West, where the heat absorption period occurs in the afternoon, resulting in direct solar radiation onto the surface. In theory, the feature classification of a West-facing slope should have a better result. However, due to the presence of hexagonal columns, the heating of the target surface in High Island Reservoir dataset was not uniform, which the patterns of the hexagonal columns could be observed in the feature classification image (Fig. 5.7(b)).

The roughness of the target slope could be a factor affecting successful feature identification. Large roughness scatters more incident heat energy in the target slope

(a) Visual image [44]

(b) Raw thermal image [44]

(c) Thermal Decay Map

(d) Feature classification image
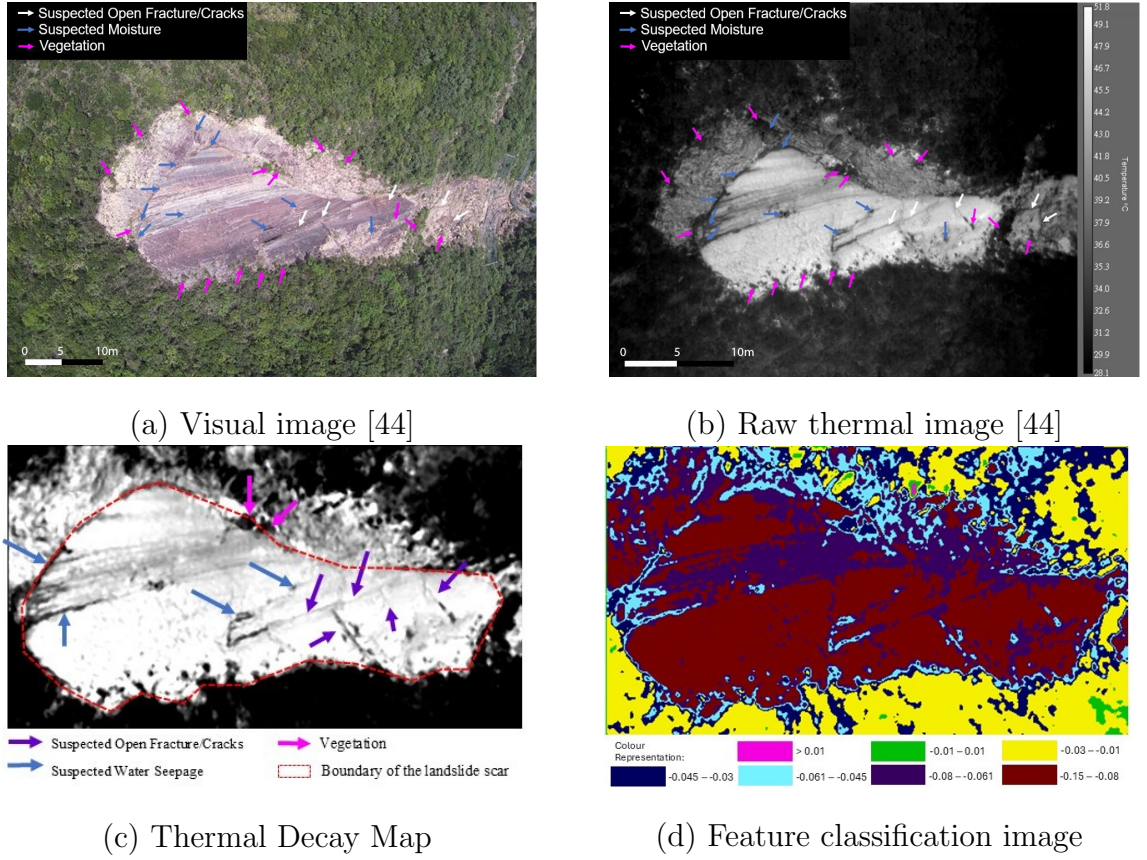
Figure 5.9: Visual image, original thermal image, Thermal Decay Map and feature classification image in Sai Wan Road Part 1 dataset.

in High Island Reservoir dataset than in the target slope in Sai Wan Road dataset, thus making the temperature measurement varied. The slope roughness increases in East Dam due to the presence of hexagonal columns. Fig. 5.10 illustrates the surface models obtained from the photogrammetric models taken by visual images from the UAS. The topographic profile was analysed to quantify the gradient and roughness of the slope surface. The first derivative determines the slope gradient, and the integral of the second derivative determines the terrain roughness defined as the variation of the gradient per meter (Fig. 5.11). The sum considers the absolute values of both the first and second derivatives. The roughness of the target slope in Sai Wan Road dataset was considered relatively smooth, which facilitated stable

109

temperature measurement and feature classification. Since the target slope in High Island Reservoir dataset is mainly hexagonal columns, its roughness is higher than the target slope in Sai Wan Road dataset, and hence feature classification after thermal decay plots was poor when compared to the results of Sai Wan Road. Only alignments of several faults could be identified in the feature classification image, in which the basaltic dyke could not be separated from the hexagonal columns of fine ash tuff (Fig. 5.7(b)). The results showed that the physical and material properties of the material could be a factor affecting the feature identification and classification when adopting time-lapse IRT with the proposed Thermal Decay Mapping method.
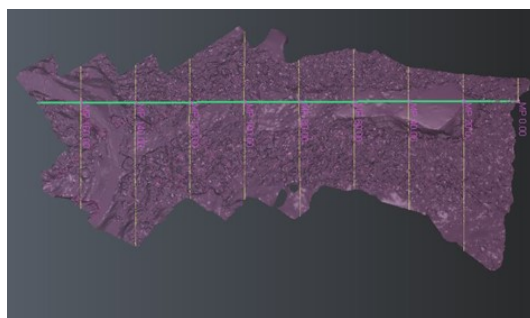
Figure 5.10: 3D top view extracted from a section of target slope in Sai Wan Road dataset by photogrammetry with horizontal profiles every 20 m.
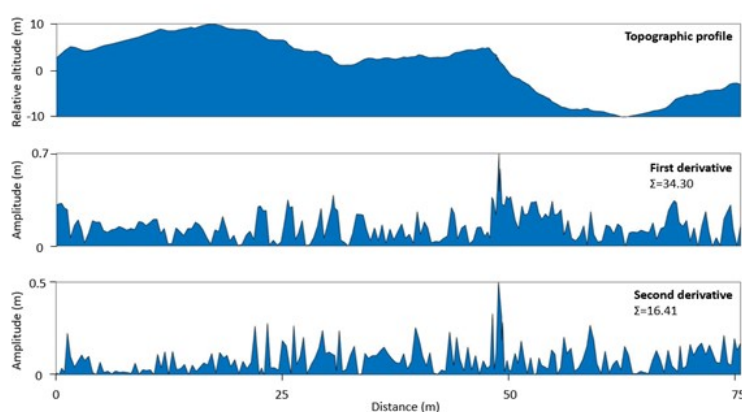
Figure 5.11: Topographic profile, first derivative and second derivative of the MP20.00 profile of the target slope in Sai Wan Road dataset, indicating its roughness.

5.5.3   Enhancement by Pixel's Standard Deviation (SD method)

The visualization of the resulting Thermal Decay Maps could be enhanced by the SD method. In the original Thermal Decay Map, the values of the maximum and minimum thermal decay gradient within the ROI (i.e. the slope surface) are used as the range of colour representation. SD of the thermal decay gradients within the ROI can be added to these values to enhance the Thermal Decay Maps. Fig. 5.12 presents the resulting Thermal Decay Maps of the target slope in Sai Wan Road dataset by adding different SDs. The SD method only alters the range of colour representation in the visualization of the resulting Thermal Decay Maps, which does not change the thermal decay gradient in each pixel of the Thermal Decay Maps, and hence will not affect the feature classification process. However, the SD method could be a useful image enhancement tool when performing qualitative analysis on the Thermal Decay Maps.

5.5.4   Feature Classifications

Referring to Fig. 5.7 and 5.8, different features could be segmented in the feature classification image because of their physical and material properties. Sai Wan Road dataset was selected in the following discussion.

The feature classification image of the target slope in Sai Wan Road Part 1 dataset and its corresponding visual image are shown in Fig. 5.9(a) and 5.9(d). Various features could be identified by the colour representation of the feature classification image. Bare rock surfaces with the highest thermal decay gradient were segmented and shown in brown colour, while the discoloured rock surfaces with slightly lower thermal decay gradient were segmented and shown in purple colour, which could be confirmed in the visual image. The location of the suspected moisture identified in the previous research [44] matched with the segmented area in black in the feature classification map. The suspected faults/cracks could be successfully seg-

111

(a) 0.5 SD

(b) 1 SD

(c) 1.5 SD

(d) 2.0 SD

(e) 2.5 SD

(f) 3.0 SD
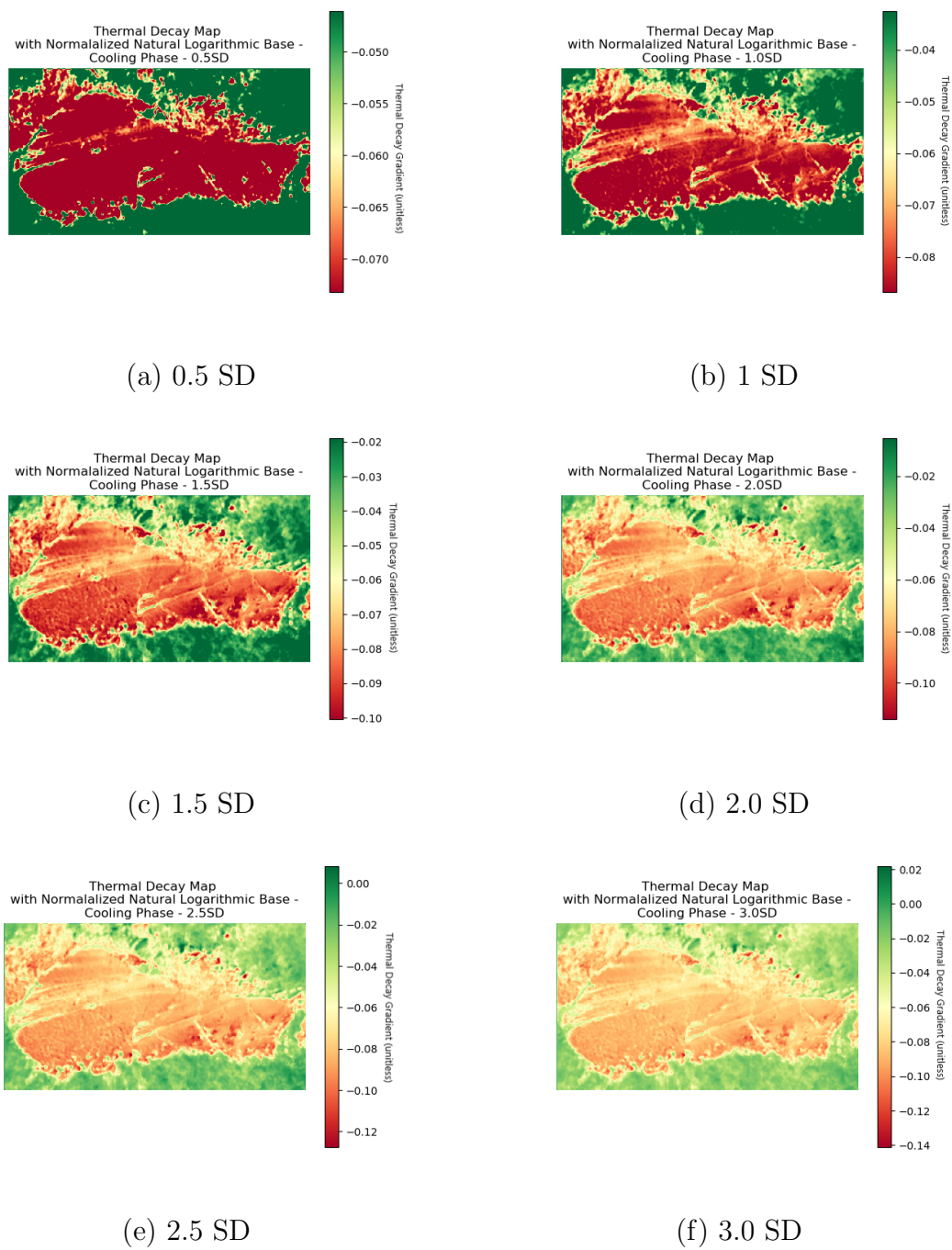
Figure 5.12: Thermal Decay Map with SD enhancement in Sai Wan Road Part 1 dataset.

mented in purple and dark blue, and the alignments could be clearly shown. Since the thermal conductivities of water and air are 0.586 W m^{-1} K^{-1} and 0.07 W m^{-1} K^{-1} respectively [49] and that of brown tuff is 0.27 W m^{-1} K^{-1} [166]. According to Eq. 2.3, a higher value for thermal conductivity k allows greater heat transfer through the medium. Hence, more heat can be transferred through moisture or faults/cracks than tuff in theory. However, the Thermal Decay Mapping method considers the cooling of the target surface. Considering the areas of tuff were much larger than that of the suspected moisture and faults, bare rock surfaces have the highest thermal decay gradient according to Eq. 2.4. The vegetation in the surrounding area was segmented and shown in yellow colour, but the sparse vegetation within the landslide scar was segmented in dark blue colour. This was due to the difference in area according to Eq. 2.4, and hence their thermal decay gradient was higher than that of the vegetation in the surrounding area.

5.6 Chapter Summary

The proposed Thermal Decay Mapping method was applied to datasets collected in High Island Reservoir and Sai Wan Road. The results of adopting the proposed method were summarized in this chapter, which fulfilled the three objectives proposed in this study. Features such as faults/cracks, moisture and vegetation could be visualized and segmented in feature classification images generated from the Thermal Decay Maps, and fulfilled part of Objective 1, which is to classify features in natural terrain. Different factors affecting the accuracy of the Thermal Decay Mapping method in secondary landslide hazard inspection were summarized and discussed in this chapter, which included the physical and material properties used in feature classifications on the target slope and the orientation and roughness of the target slope, and fulfilled part of Objective 2. The performance of the proposed Thermal Decay Mapping method was evaluated by comparing the findings in published materials

and qualitative results by snapshot IRT to assess the performance of the proposed method, which fulfilled part of Objective 3.

To sum up, this study validated the possibility of adopting the Thermal Decay Mapping method in secondary landslide hazard inspection by performing feature extraction based on different rates of thermal decay. Based on the results presented in this chapter, the resulting Thermal Decay Maps could be used in the feature classification of a slope, in which a feature classification image of the target slope could be generated from the thermal decay gradient. The results also showed that a time-lapse IRT survey with the aid of UAS using the Thermal Decay Method could provide quantitative results of the features identified since the ratio of the classified features on the slope could be calculated by the number of pixels in the same colour to the number of pixels within the ROI (i.e. the slope surface), which the data collection of using a UAS to capture thermal images of slopes in this study is the first case study in Hong Kong. The proposed method shows great improvement in secondary landslide hazard diagnosis in addition to traditional visual inspection and rock sampling.

Chapter 6

Thermal Image Processing by Statistical Approach - Machine Learning

6.1 Chapter Overview

Different from the Thermal Decay Mapping method which stems from thermal transfer physics, this chapter presents an attempt to adopt the machine learning approach to perform defect identification on external walls of a building, and feature classification on slopes, which the results and findings are presented in this chapter.

6.2 Selection of Thermal Frame Data

The general workflow in the Machine Learning method is summarized in Section 3.2.2, and the first step is to prepare the thermal data. To prepare both the training

and testing datasets, thermal images from the heat absorption period and the heat dissipation period need to be selected from the sequence of thermal images collected in a time-lapse IRT survey. Therefore, similar to the Thermal Decay Mapping method, it is important to examine the temporal plot of all the features on the target surface to determine which frames to be selected for extracting data points to build the training and testing dataset. The thermal datasets used in this chapter included datasets collected in Shek Mun and PolyU for building inspection, and datasets collected in High Island Reservoir and Sai Wan Road for secondary landslide hazard inspection, which the details of the data collection of each dataset were summarized in Section 3.4.1 and 3.4.2.

6.2.1   Thermal Data - Building Wall Finishes

Shek Mun dataset was used as the training dataset because the sample wall of 8 different wall finish materials was arranged to face towards the East and received direct solar radiation for sufficient thermal contrast between the defects and the intact area, in which 3 days of data were collected. The temporal plots of all wall finish materials on each day were illustrated in Fig. 6.1 to 6.6 respectively, where the two peaks and the transition period were marked on each temporal plot. The first peaks (indicated by orange arrows) occurred in the morning session, which was the heat absorption period since the sample wall faced towards the East and was heated up in the morning session. After the first peaks occurred, heat dissipation began. Second peaks (indicated by blue arrows) could be observed in the figures. The occurrences of the second peaks were due to the characteristics of the sample wall constructed, which was addressed and explained in Section 4.2. Transition periods occurred between the heat absorption period and the heat dissipation period, which were marked in red dashed boxes in the figures. During the transition period, the temperatures of the defects gradually decreased and there was an instant when the thermal contrast between the defects and the intact area was minimal, and defects could not be detected

in that moment [167]. After the transition period, the temperatures of the defects were lower than the temperatures in the intact area. This resulted in the defects showing as cold spots in the thermal images taken at night (Fig. 6.7). Thermal data collected on Day 3 showed abnormal temporal plots (Fig. 6.5 and 6.6). The temperatures in both the defect and intact area continued increasing even after the normal heat absorption period, until they reached the observed time when the second peaks occurred on Days 1 and 2. The temperatures in the second peaks on Day 3 were higher than the temperatures recorded in the first peaks. Due to this abnormal behaviour, Day 3 dataset was not used for building the training dataset.

The thermal contrast between the defects and the intact area in the heat absorption period was used as the first attribute in each training dataset, while the thermal contrast between the defects and the intact area in the heat dissipation period was used as the second attribute in each training dataset. To retrieve these two attributes, frames capturing the maximum thermal contrasts were selected. For the first attribute in each training dataset, a sequence of images (indicated by green dashed boxes in Fig. 6.1 to 6.4) was selected in the heat absorption period when the maximum thermal contrasts between the defects and the intact area occurred. Multiple training datasets were built by using images within the selected sequence. For the second attribute in each training dataset, the image capturing the moment when the defects were shown as cold spots was selected in the heat dissipation period. Referring to the temporal plots illustrated in Fig. 6.1 to 6.4, the fluctuation in the thermal contrast between the defects and the intact area became more stable during the heat dissipation period than the heat absorption period, since no solar radiation could be received by the target surface, and the rate of cooling in the defects and the intact area solely depended on their thermal properties of the materials but not the environment. Therefore, for efficient data preparation in later data processing, the last images on each survey day (indicated by purple arrows in Fig. 6.1 to 6.4) were selected as the image for extracting the second attribute for each training dataset.

117

Figure 6.1: Temporal plots of wall finishes in Group 1 (top left-handed corner) and Group 2 in Shek Mun Day 1 dataset.

Remarks: • Frame in this plot can be converted to time, in which the starting time was 8:23 am, and the images were taken at 5-min intervals. • Orange arrows indicate the first peaks; blue arrows indicate the second peaks; green dashed boxes indicate the selected sequences of images for extracting the first attributes; purple arrows indicate the selected images for extracting the second attributes; red dashed boxes indicate the transition period.
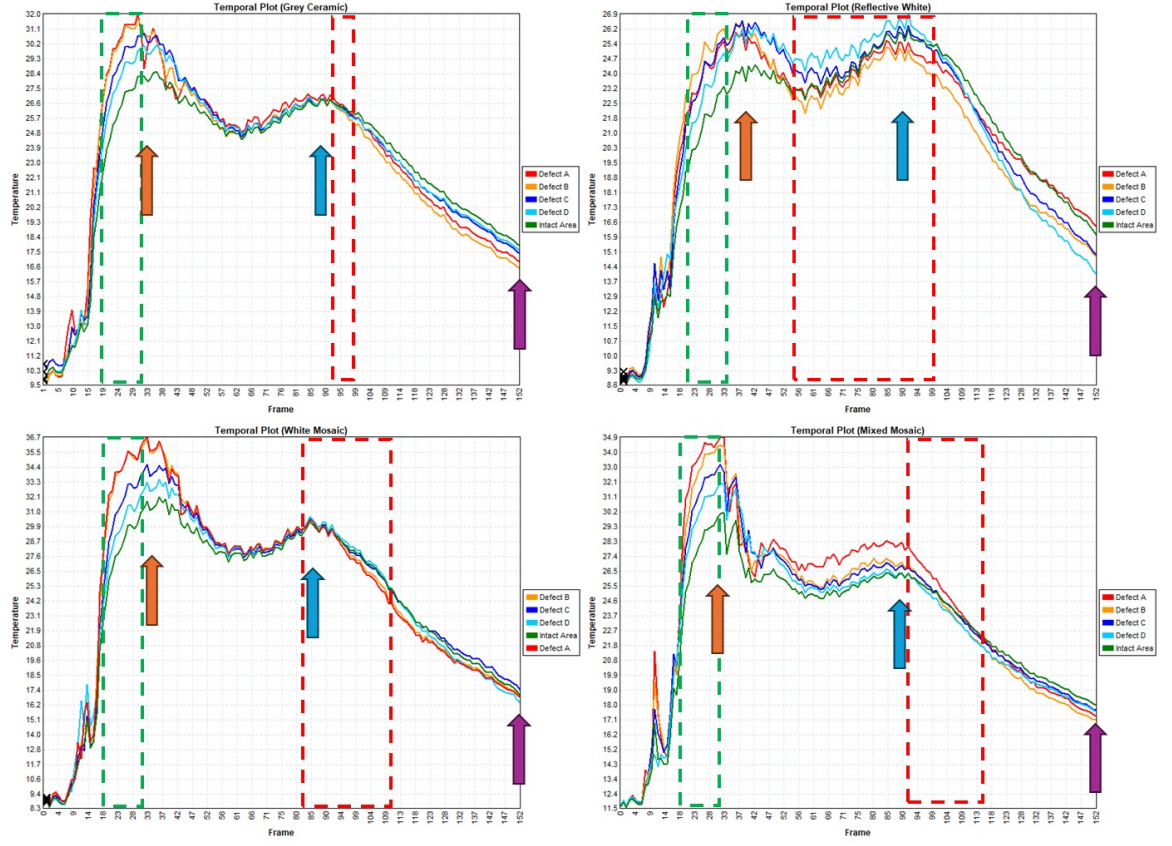
Figure 6.2: Temporal plots of wall finishes in Group 3 in Shek Mun Day 1 dataset.

Remarks: ● Frame in this plot can be converted to time, in which the starting time was 8:23 am, and the images were taken at 5-min intervals. ● Orange arrows indicate the first peaks; blue arrows indicate the second peaks; green dashed boxes indicate the selected sequences of images for extracting the first attributes; purple arrows indicate the selected images for extracting the second attributes; red dashed boxes indicate the transition period.

119

Figure 6.3: Temporal plots of wall finishes in Group 1 (top left-handed corner) and Group 2 in Shek Mun Day 2 dataset.

Remarks: • Frame in this plot can be converted to time, in which the starting time was 8:00 am, and the images were taken at 5-min intervals. • Orange arrows indicate the first peaks; blue arrows indicate the second peaks; green dashed boxes indicate the selected sequences of images for extracting the first attributes; purple arrows indicate the selected images for extracting the second attributes; red dashed boxes indicate the transition period.

Figure 6.4: Temporal plots of wall finishes in Group 3 in Shek Mun Day 2 dataset.
Remarks: • Frame in this plot can be converted to time, in which the starting time was 8:00 am, and the images were taken at 5-min intervals. • Orange arrows indicate the first peaks; blue arrows indicate the second peaks; green dashed boxes indicate the selected sequences of images for extracting the first attributes; purple arrows indicate the selected images for extracting the second attributes; red dashed boxes indicate the transition period.

121

Figure 6.5: Temporal plots of wall finishes in Group 1 (top left-handed corner) and Group 2 in Shek Mun Day 3 dataset.

Remarks: • Frame in this plot can be converted to time, in which the starting time was 8:30 am, and the images were taken at 5-min intervals. • Orange arrows indicate the first peaks; blue arrows indicate the second peaks; red dashed boxes indicate the transition period.
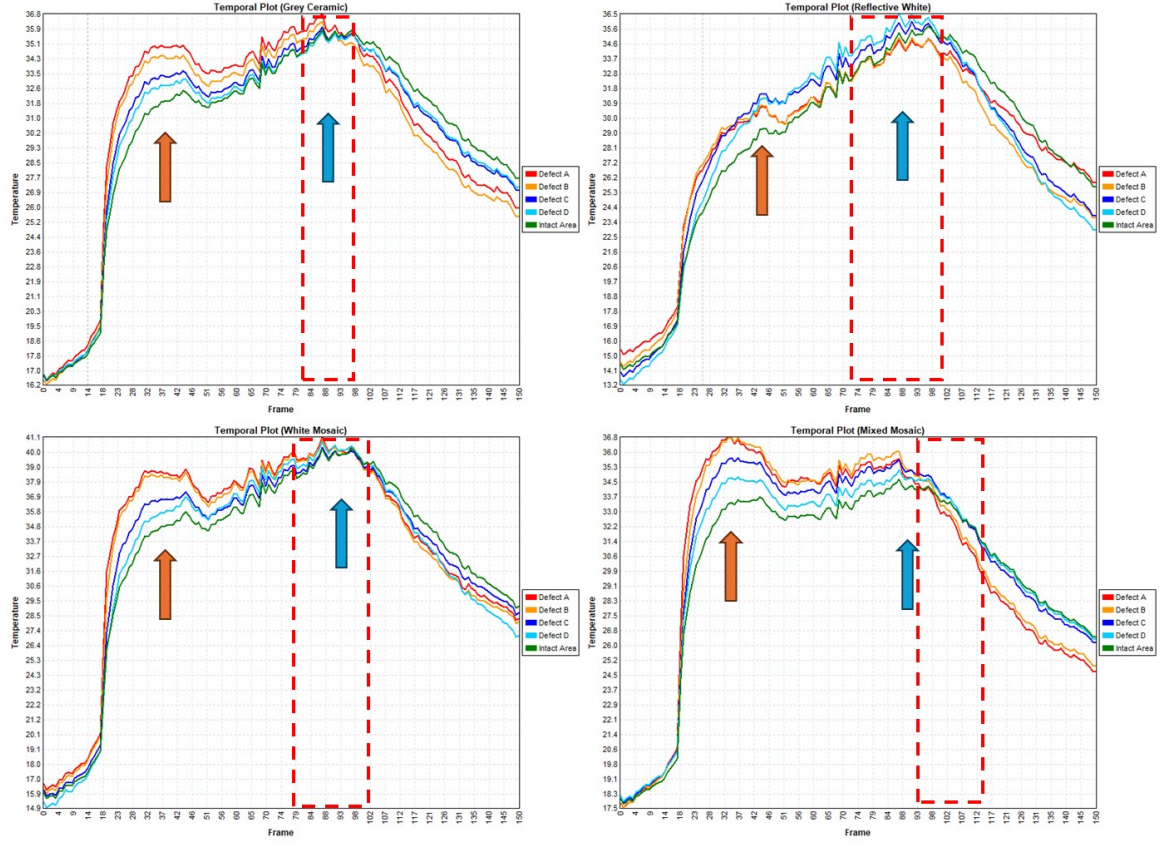
Figure 6.6: Temporal plots of wall finishes in Group 3 in Shek Mun Day 3 dataset.
Remarks: • Frame in this plot can be converted to time, in which the starting time was 8:30 am, and the images were taken at 5-min intervals. • Orange arrows indicate the first peaks; blue arrows indicate the second peaks; red dashed boxes indicate the transition period.

Figure 6.7: Thermal images in the heat absorption, transition and heat dissipation period.

To test the prediction model, PolyU dataset was used as the testing dataset.

The first attribute in each testing dataset was extracted from the frames within the heat absorption period where the maximum thermal contrast between the defects and the intact area occurred. Multiple testing datasets were built by using frames within a select period (marked in a green dashed box in Fig. 6.8), to ensure sufficient thermal contrast between the defects and the intact area for defect detection. Frame 79 in Position A dataset was dropped as the vision was blocked by the fabric of the tent. The second attribute in each testing dataset was extracted from an image selected in the heat dissipation period, when the temperatures of all features were minimum on the survey day, which was marked by a purple arrow in the figure. The thermal contrast between the defects and the intact area extracted from the selected image was used as the second attribute in each testing dataset.
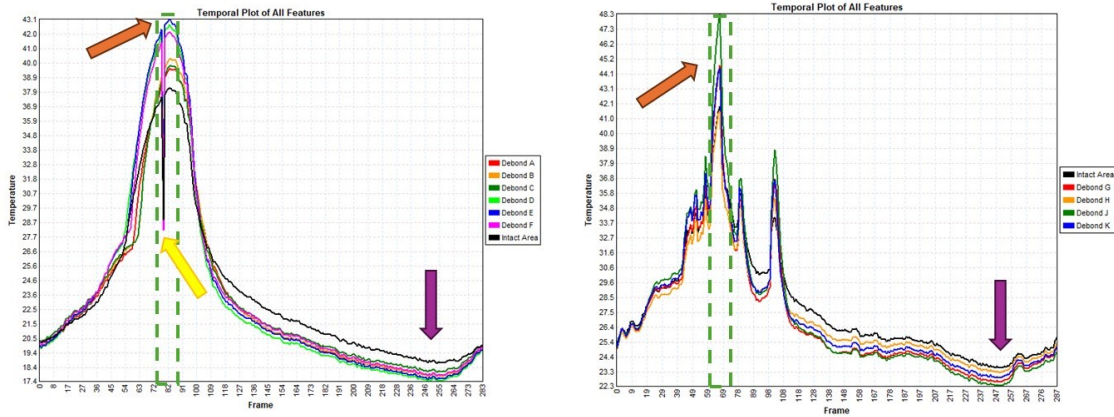
Figure 6.8: Temporal plots of all features in PolyU dataset.

Remarks: • Frame in this plot can be converted to time, in which the starting time was 8:30 am, and the images were taken at 5-min intervals. • Orange arrows indicate the first peaks; green dashed boxes indicate the frames within selected period (i.e. the first attributes in each testing dataset); purple arrows indicate the selected images for extracting the second attributes in each testing dataset; yellow arrows indicate the dropped frame 79.

After selecting suitable thermal images for constructing the training and testing dataset, a thermal contrast value in each pixel of the thermal images was calculated. For the first attribute in each dataset (i.e. selected images in the heat absorption period), the minimum temperature within the ROI was used as the reference temperature for the calculation of the thermal contrast in each pixel. For the second

attribute used in each dataset (i.e. selected images in the heat dissipation period), the maximum temperature within the ROI was used as the reference temperature to calculate the thermal contrast in each pixel. Then, in the training dataset, the pixels within the defect area were labelled as "1", while the pixels in the intact area were labelled as "0". Table 6.1 summarizes the total number of labelled data points in each training dataset.

Table 6.1: Summary of the number of labelled data points in each training dataset

Dataset	Total Pixel Number
Day 1 Group 1	432718
Day 1 Group 2	599368
Day 1 Group 3	986034
Day 2 Group 1	432718
Day 2 Group 2	599368
Day 2 Group 3	845173

6.2.2 Thermal Data - Slope Features

To train a prediction model for secondary landslide hazard inspection, High Island Reservoir dataset was used as the training dataset because this dataset was collected by ground-based IRT. The thermal camera was set up using a tripod and was not being moved during the data collection. Hence, a pixel-to-pixel comparison could be performed directly without the need for thermal image registration. For the testing dataset, Sai Wan Road Part 1 dataset was used as the target slope in this part consisting of rock surface, cracks and moisture, while Sai Wan Road Part 2 dataset mainly consisted of vegetation. Another reason is that the number of thermal images taken in Sai Wan Road dataset was much smaller, and the distance between the thermal camera and the target surface was large, resulting in poorer resolution or larger IFOV. There were difficulties in picking data points for small features (i.e.

cracks) for preparing labelled data. Hence, Sai Wan Road Part 1 was used as the testing dataset, instead of the training dataset.

Similar to the Thermal Decay Mapping method, it is necessary to examine the temporal plot of all the features on the target surface to determine which frames to be selected for extracting attributes to prepare both the training and testing dataset (Fig. 6.9 and Fig. 6.10). The dataset collected in High Island Reservoir is used for the explanation in this section. The features identified on the target surface include vegetation, fine ash tuff in weathering grades 3 and 4 to 5, basalt dyke and faults. From the temporal plots, the peaks of all features occurred at the frame numbers ranging from 35 to 46 (i.e. 2:30 pm to 3:25 pm). The range of temperatures of vegetation within the whole period is the narrowest, which is between 30.19℃ and 34.05℃, and the range of temperatures of fine ash tuff in weathering grades 4 to 5 is the widest, which is between 41.82℃ and 33.94℃. The thermal behaviours of all features were studied in the previous chapter (Section 5.2 in Chapter 5 by observing the histograms of the features. Vegetation and fresh as tuff in weathering grades 4 to 5 could be separated from other features in different timestamps.

The preparation of the training dataset for secondary landslide hazard inspection was similar to the steps in Section 6.2.1. The thermal contrast between the features and the reference temperature within the ROI was used as the attributes for developing the prediction model. The first attribute was extracted from the selected frames in the heat absorption period when the peaks occurred (indicated by orange arrows in the temporal plot in Fig. 6.9 and 6.10) to ensure there was sufficient thermal contrast in the features for slope feature classification. The sequences of the thermal images used for extracting the first attributes in each dataset were marked in the red dashed boxes in the figures. The second attribute was extracted from the frame selected in the heat dissipation period (marked by purple arrows in the figures), which the last image was used for data preparation efficiency. After selecting suitable thermal images for constructing the training and testing dataset, a thermal contrast

value in each pixel of the thermal images was calculated. Similar to the approach adopted for building inspection, the minimum temperature within the ROI was used as the reference temperature for the calculation of the thermal contrast in each pixel in the selected images within the heat absorption period as the first attributes in each dataset. For extracting the second attributes from the selected frames in the heat dissipation period in each dataset, the maximum temperature within the ROI was used as the reference temperature to calculate the thermal contrast in each pixel. Then, in the training dataset, the pixels in the vegetation area were labelled as "0", while the pixels of the fresh ash tuff with weathering grades 3 and 4 to 5, basalt and faults were labelled as "1", "2", "3", and "4" respectively. The total number of labelled data points in this training dataset was 154,990.
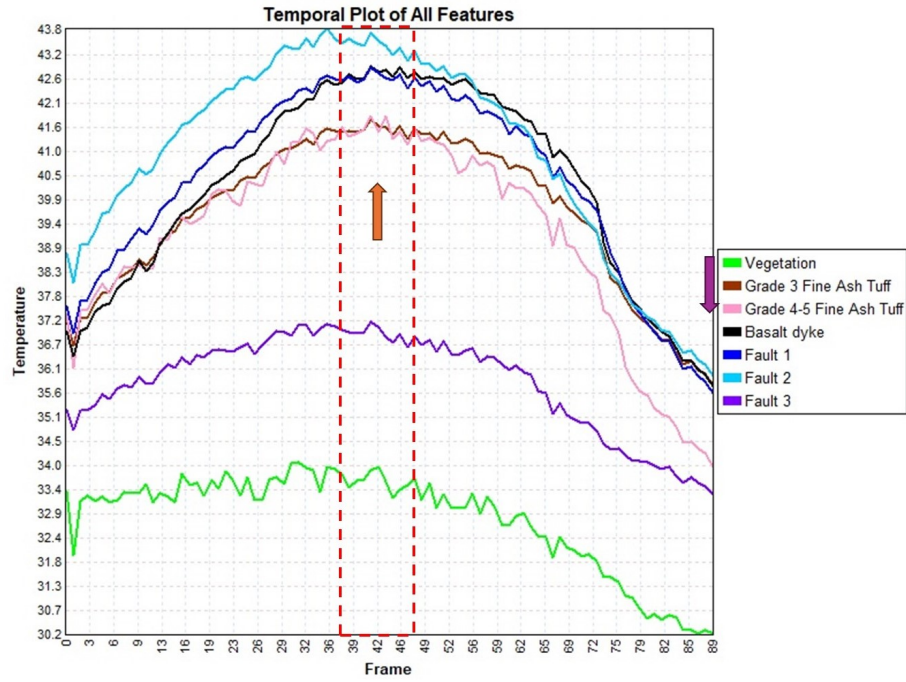
Figure 6.9: Temporal plots of all features on the slope in High Island Reservoir dataset.

Remarks: • Frame in this plot can be converted to time, in which the starting time was 11:41 am, and the images were taken at 5-min intervals. • Orange arrows indicate the first peaks; purple arrows indicate the selected images for extracting the second attributes; red dashed boxes indicate the selected sequence of thermal images used for extracting the first attributes.
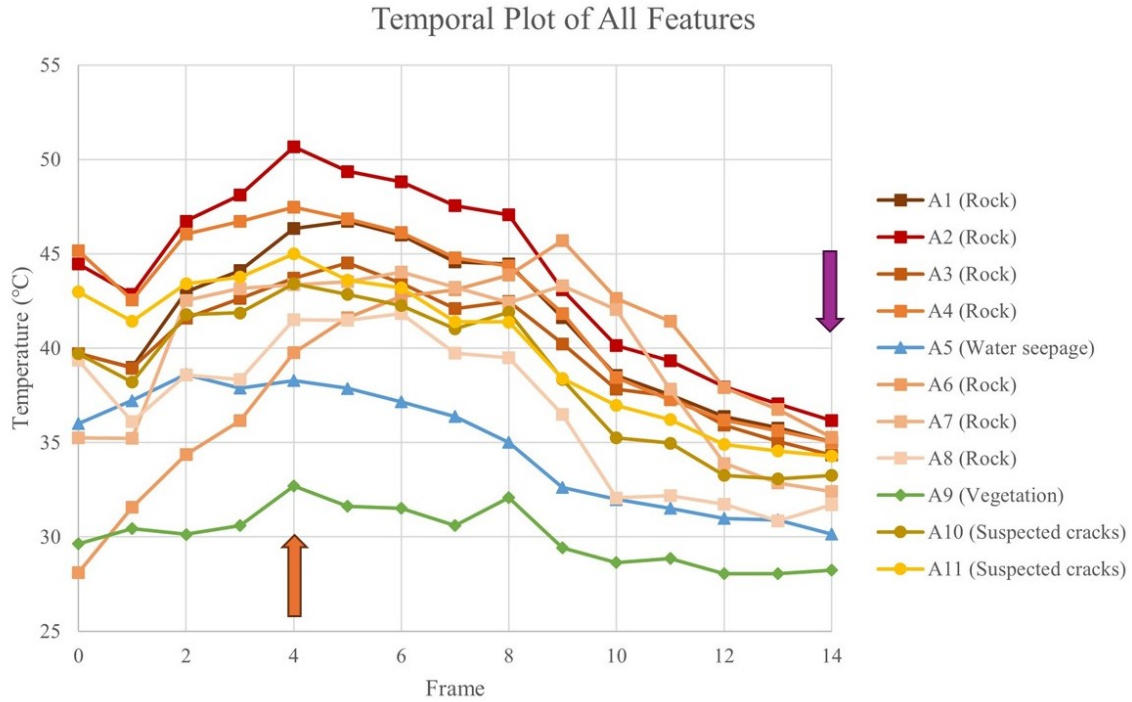
Figure 6.10: Temporal plots of all features on the slope in Sai Wan Road Part 1 dataset.

Remarks: ● Frame in this plot can be converted to time, in which the starting time was 11:41 am, and the images were taken at 5-min intervals. ● Orange arrows indicate the first peaks (the selected images used for extracting the first attributes); purple arrows indicate the selected images for extracting the second attributes.

6.3   Training the Prediction Model

6.3.1   Feature Space

To train the prediction model, the first step is feature scaling. The continuous attributes in each dataset were combined and then converted by using a selected scaler. Among the three scalers introduced in Section 2.5.3, the min-max scaler was used for building inspection, while the robust scaler was used for secondary landslide hazard inspection in the training. Since the observations in the histograms of the building dataset reflected that the pixels of the defects and the intact area

could mostly be separated and the number of outliers was small (Fig. 4.4), the min-max scaler was then used for building inspection due to fast processing time. For secondary landslide hazard inspection, the features in the target slope were not normally distributed in the histograms (Fig. 5.3), and hence the standard scaler was not used. The min-max scaler was also abandoned since this scaler is very sensitive to outliers in the dataset. The same rescaling parameters (i.e. the min-max scaler for buildings, and the robust scaler for slopes) for the testing dataset are applied to rescale the testing dataset when performing the prediction.

Training Dataset - Building Wall Finishes

Fig. 6.11 and 6.12 summarize the feature spaces in each wall finish material in Shek Mun Day 1 dataset. From the figure, the data points of the defects and the intact area could not be separated when the thermal contrast between them was insufficient (i.e. at the starting time, which was before the heat absorption period began)(left plots of Fig. 6.11 and 6.12). When the temperatures of the defects and the intact area reached their maximum, the data points of the defects and the intact area could be separated although part of the data points still overlapped with each other (middle plots of Fig. 6.11 and 6.12), which logistic regression equation (Eq. 2.21) can be applied to separate the defect data points and the intact area data points. If the defects appeared as cold spots in both the images for extracting the first attributes and the images for extracting the second attributes in the training dataset, the data points of the defects and the intact area would completely overlap with each other (right plots of Fig. 6.11 and 6.12). Hence, the training dataset was developed by using the thermal images during the heat absorption period when the maximum thermal contrast between the defects and the intact area occurred for extracting the first attributes in the training dataset. The best periods capturing these sequences of thermal images were summarized in Table 6.2 [102] and indicated in green dashed boxes in Fig. 6.1 to 6.4. Then, data points within the best period in

each wall finish material were combined into three main training datasets according to their emissivities (Table 3.3). Optimisation was then performed to determine the optimal model parameters for the prediction.

(a) Group 1 (Rendering) & Group 2 (Blue Mosaic)

(b) Group 2 (Smooth Black) & Group 2 (Matt Black)
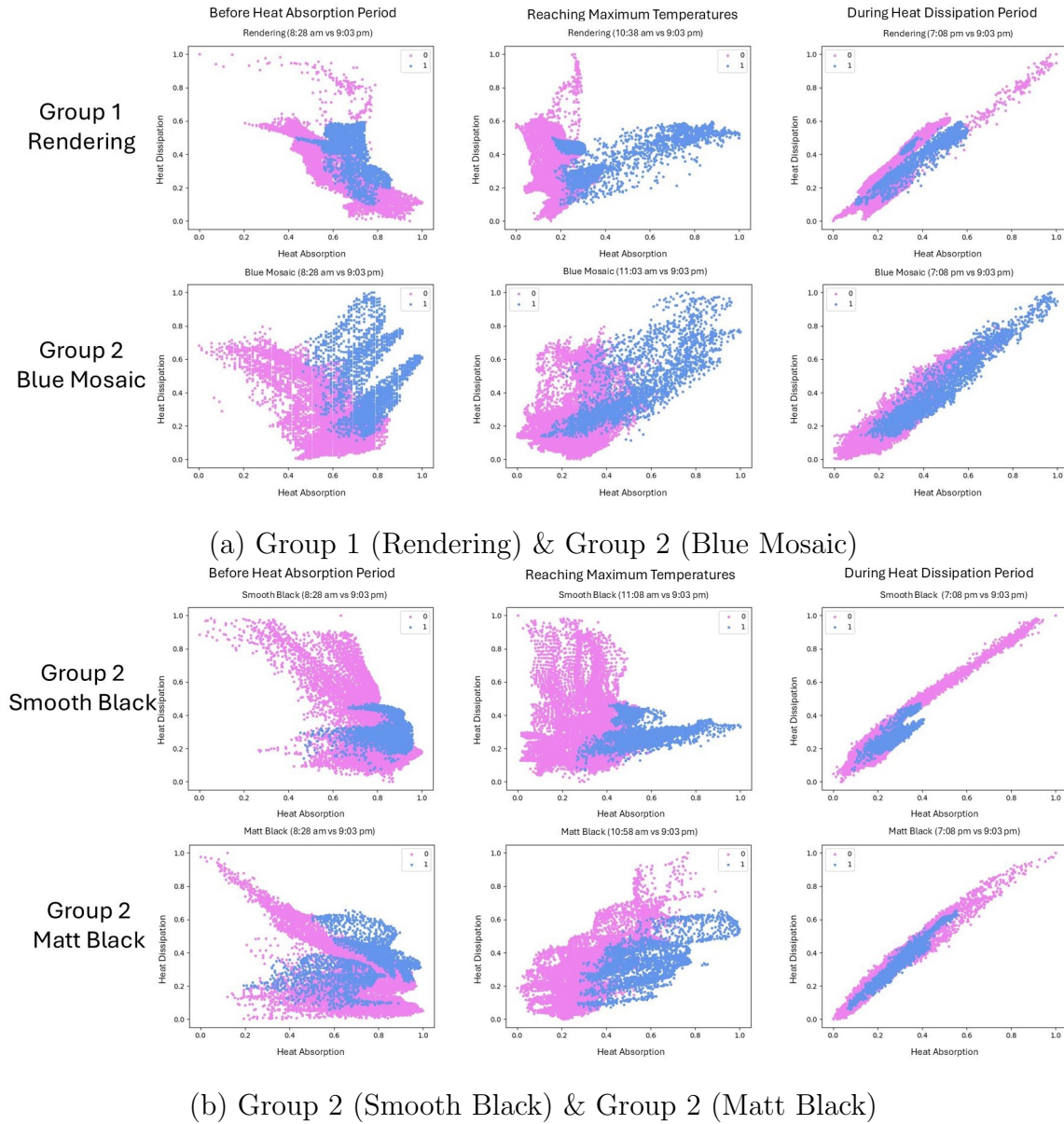
Figure 6.11: Feature spaces in each wall finish materials in Group 1 and 2 in Shek Mun Day 1 dataset.

Remarks: Blue dots represent the defect data points; pink dots represent the intact area data points.

(a) Group 3 (Grey Ceramic) & Group 3 (Reflective White)

(b) Group 3 (White Mosaic) & Group 3 (Mixed Mosaic)
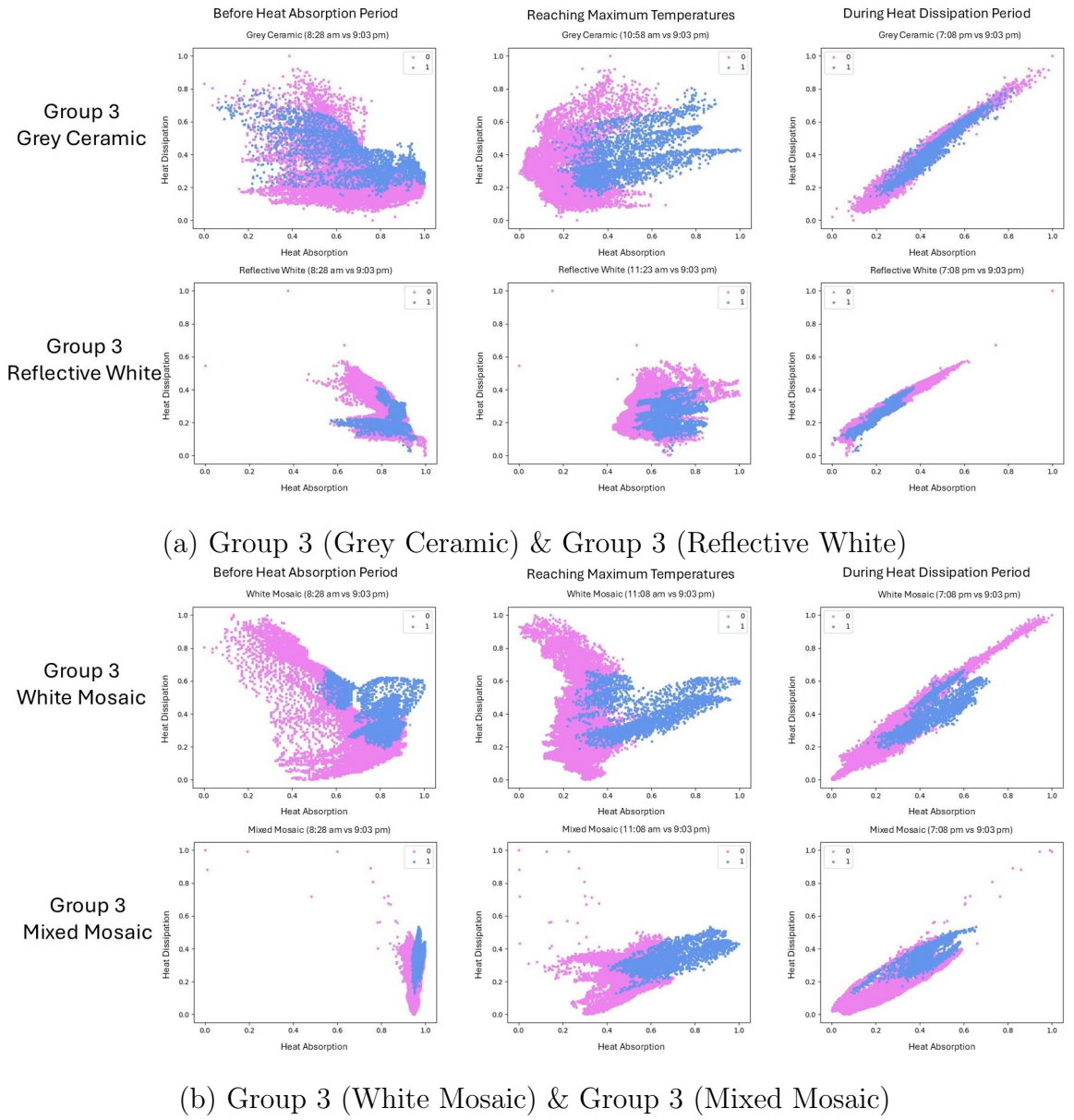
Figure 6.12: Feature spaces in each wall finish materials in Group 3 in Shek Mun Day 1 dataset.

Remarks: Blue dots represent the defect data points; pink dots represent the intact area data points.

Table 6.2: Summary of the best period in each training dataset

Dataset	Best Period	
	Starting Frame (Time)	Ending Frame (Time)
Day 1 Group 1	18 (9:58am)	43 (12:03pm)
Day 1 Group 2	21 (10:13am)	31 (11:03am)
Day 1 Group 3	18 (9:58am)	31 (11:03am)
Day 2 Group 1	20 (9:40am)	45 (11:45am)
Day 2 Group 2	18 (9:30am)	28 (10:20am)
Day 2 Group 3	26 (9:45am)	37 (11:20am)

The feature spaces of three main training datasets according to their emissivities with the corresponding decision boundaries in Shek Mun Day 1 and 2 datasets are summarized in Fig. 6.13, and the decision boundary equations for each training datasets are shown in Eq. (6.1) to (6.6), where x is the thermal contrast between the defects and the intact area in the heat absorption period, and y is the thermal contrast between the defects and the intact area in the heat dissipation period.

Decision Boundary Equation for each training datasets for building inspection

Shek Mun Day 1 - Group 1 Dataset

$$32.6393x - 3.1943y - 6.4709 = 0 \qquad (6.1)$$

Shek Mun Day 1 - Group 2 Dataset

$$23.6180x + 1.0779y - 9.7729 = 0 \qquad (6.2)$$

Shek Mun Day 1 - Group 3 Dataset

$$4.7454x - 0.0897y - 3.1096 = 0 \qquad (6.3)$$
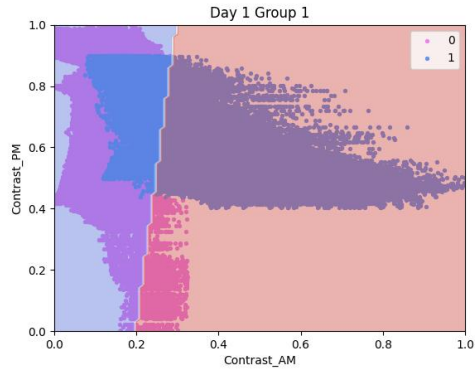
(a) Day 1 Group 1
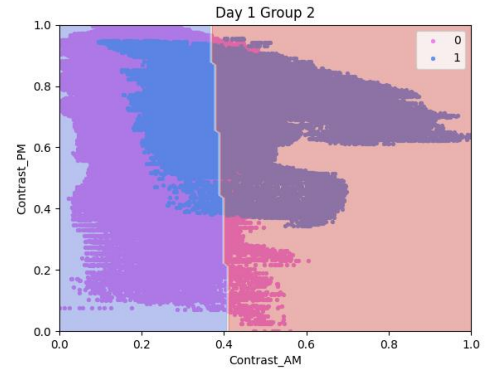
(b) Day 1 Group 2
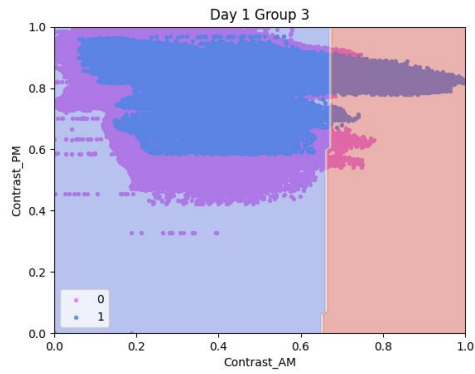
(c) Day 1 Group 3
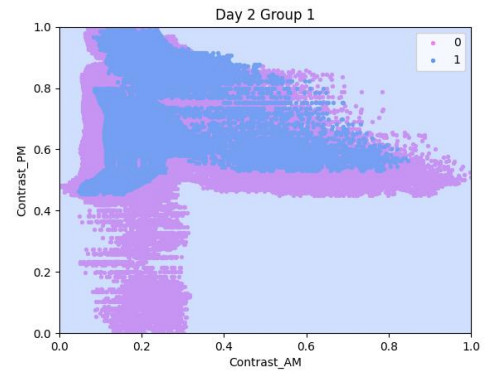
(d) Day 2 Group 1
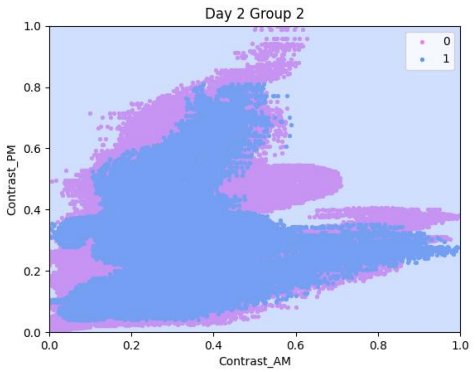
(c) Day 2 Group 2
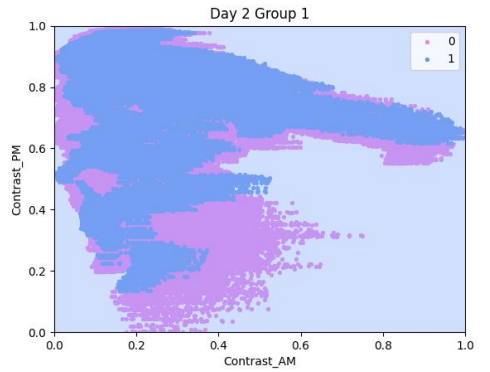
(d) Day 2 Group 3

Figure 6.13: Feature Spaces in the training datasets for building inspection with corresponding decision boundaries.

Shek Mun Day 2 - Group 1 Dataset

$$-0.7861x - 0.3349y - 1.2463 = 0 \tag{6.4}$$

Shek Mun Day 2 - Group 2 Dataset

$$0.5130x + 0.7607y - 2.0640 = 0 \tag{6.5}$$

Shek Mun Day 2 - Group 3 Dataset

$$1.3827x - 0.2963y - 1.8230 = 0 \tag{6.6}$$

Training dataset - Slope Features

The feature space in the training dataset built from the High Island Reservoir dataset is presented in Fig. 6.14. From the figure, only data points with the label "0" could be separated from the rest of the data points, which were the data points of vegetation. This showed that the thermal contrast between the features and a reference temperature within the ROI could only provide sufficient information for classifying vegetation on a slope, but not the other features like weathered rocks or cracks. Nevertheless, optimisation was performed to determine the optimal model parameters of this training dataset, attempting to classify vegetation in the testing dataset in the prediction stage.

6.3.2   Optimisation of the Model

Optimisation was performed on the parameters of the logistic regression classifier by determining the gradient descent. The regularisation strength was defaulted as 1. Adjustment of the degree of model complexity (in a range from 1 to 12 for the building dataset, and 1 to 10 for the slope dataset) was performed to generalise the decision boundaries for the defects and the intact area. The L2 norm (previously
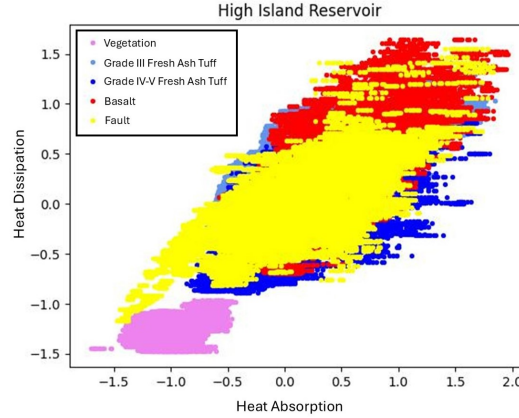
Figure 6.14: Feature spaces in High Island Reservoir dataset.

discussed in Section 2.5.3) was set as the penalty used in the regularisation since it is less computationally expensive [137]. Bias-variance decomposition was performed to evaluate the errors of the optimised classifier, which was integrated with 5-fold cross-validation, since its computation is more efficient as recommended in [140]. The optimal model in each training dataset was selected with the degree of complexity with the smallest bias and variance.

Thermal Dataset - Building Wall Finishes

Fig. 6.15, 6.16 and 6.17 summarize the plots of bias-variance decomposition in each group training dataset respectively, which the plots showed the weighted F1-score of the training and the validation. In each plot, the weighted F1-score of the training was plotted in red, and the weighted F1-score of the validation was plotted in green. From the figure, the weighted F1-scores of the training and the validation in the Group 1 (highest emissivity) and 2 (high emissivity) training datasets constructed from Shek Mun Day 1 dataset were above 0.85. However, the weighted F1-score were not ideal in the Group 1 and 2 training datasets constructed from Shek Mun Day 2 dataset, which were between 0.5 and 0.68. For Group 3 (low emissivity) training datasets, the weighted F1-scores on both days were below 0.75. This suggested that

using the Group 1 and 2 training dataset constructed from Shek Mun Day 1 dataset as the logistic regression classifier could increase the probability of successful prediction. The optimal degree of complexity in each training dataset was selected where both the weighted F1-scores of the training and the validation were the highest and the difference between them was small. Table 6.3 summarizes the corresponding degree of freedom used in the prediction when using the corresponding training dataset as the logistic regression classifier.
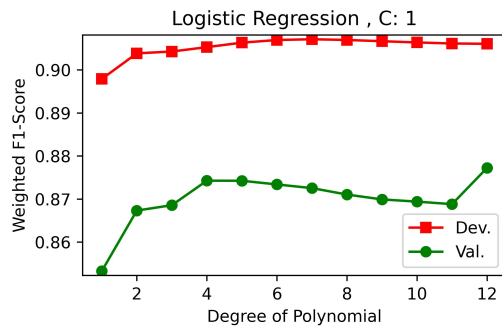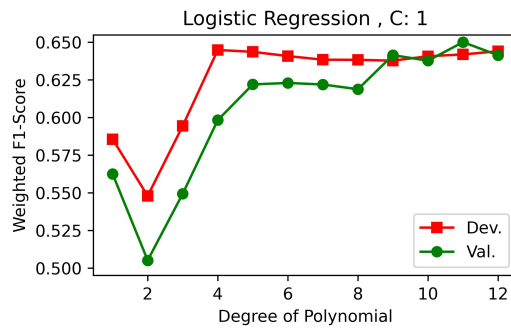
(a) Day 1   (b) Day 2

Figure 6.15: Bias-variance decomposition in Group 1 training datasets.
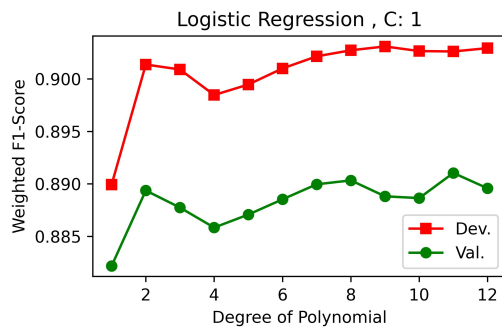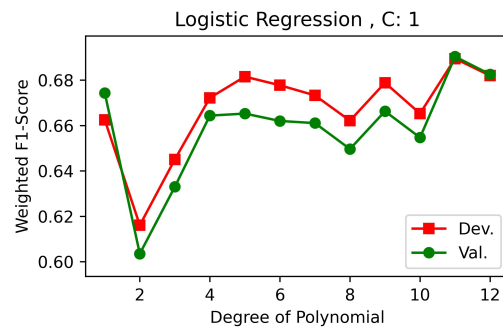
(a) Day 1   (b) Day 2

Figure 6.16: Bias-variance decomposition in Group 2 training datasets.

(a) Day 1   (b) Day 2
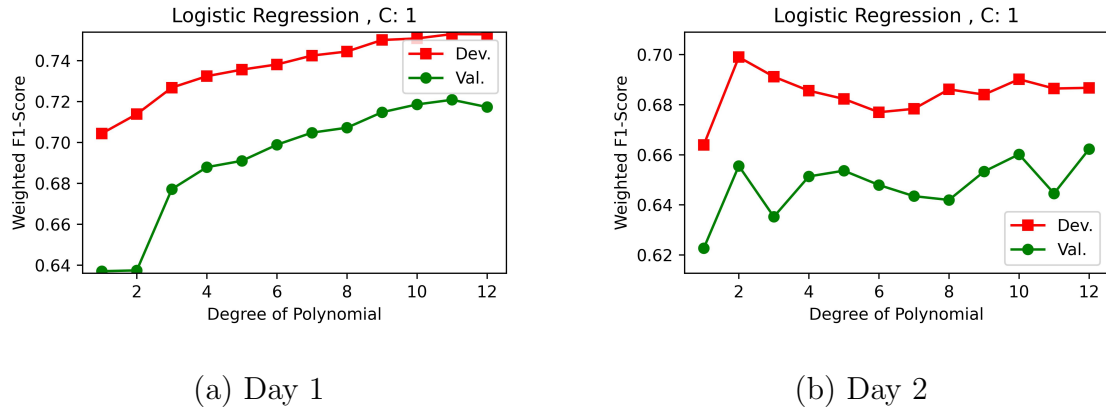
Figure 6.17: Bias-variance decomposition in Group 3 training datasets.

Table 6.3: Summary of the optimal degree of complexity for each training dataset

Dataset	Degree of Complexity
Day 1 Group 1	4
Day 1 Group 2	11
Day 1 Group 3	11
Day 2 Group 1	7
Day 2 Group 2	9
Day 2 Group 3	10

Thermal dataset - Slope Features

Fig. 6.18 illustrates the plot of bias-variance decomposition in the training dataset. The figure showed that the weighted F1 scores of the training and the validation were all below 0.65. Even increasing the degree of polynomial could not further improve the performance of the prediction. This suggested that using this training dataset beyond the degree of polynomial 2 as the logistic regression classifier could result in unfavourable predictions. However, the number of slope datasets collected in this study was limited, and only High Island Reservoir dataset could provide a variety of features to develop the training model. The selected optimal

137

degree of complexity in this training dataset was 2.
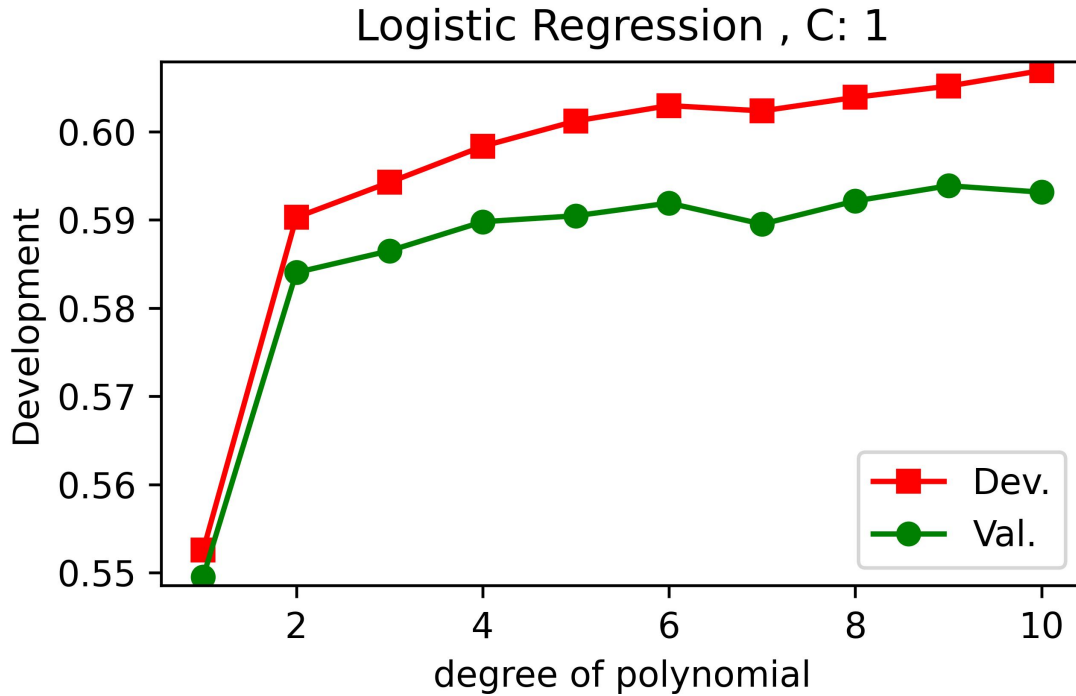
Figure 6.18: Bias-variance decomposition in High Island Reservoir training datasets.

6.4 Prediction and Accuracy Evaluation

After determining the optimal parameters to be used with each training dataset, the testing datasets prepared in the previous section were imported into the in-house program to perform prediction using the training dataset as the logistic regression classifier. For building inspection, there were two testing datasets, which were PolyU Position A and Position B datasets. 6 defects were embedded and covered by reddish-brown wall tiles in the sample wall at Position A, while 4 defects were embedded and covered by rendering in the sample wall at Position B. All groups of training datasets were used in the validation of the automatic defect classification using the prediction model, regardless of the actual emissivity value of the target surfaces in the testing

dataset. Since there were unrelated objects near the target surface at both Position A and Position B, image masks were applied to mask out the unwanted features on the target wall before performing the prediction (Fig. 6.19).
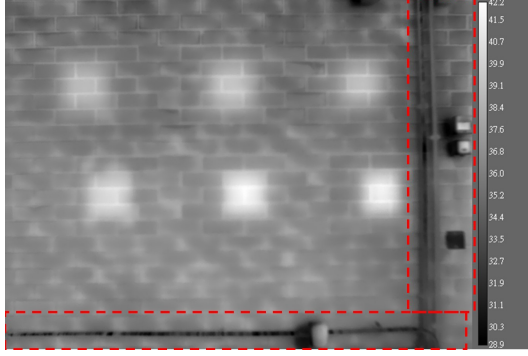
(a) Position A - Unwanted Features

(b) Position A - Image Mask
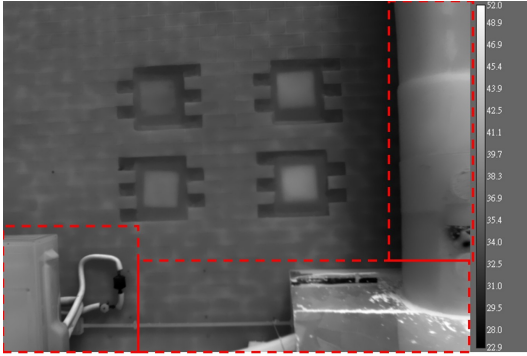
(c) Position B - Unwanted Features

(d) Position B - Image Mask

Figure 6.19: Unwanted features (in red dashed boxes) and the corresponding masks used at Position A and B.

Table 6.4 summarizes the performance of each classifier in feature classification, which ✓ represents successful defect classification and × represents unsuccessful defect classification. The results showed that automatic defect classification could be successfully performed at Position A and B when using all of Shek Mun Day 1 datasets as the classifier, while only Group 2 training datasets constructed from Shek Mun Day 2 datasets could give a prediction of suspected defects among the datasets

139

constructed from the data collected on the same day. Since the feature spacing and bias-variance decomposition of the training dataset for secondary landslide inspection resulted in poor performance, the prediction model could not return an image for the feature classification on the slope testing dataset. Discussion is summarized in the following subsections, which include the factors affecting the success of a prediction, and the performance of each successful prediction.

Table 6.4: Summary of Successful Feature Classification in Test Data

| Classifier | | Testing Dataset | | |
| | | Building | | Slope |
		PolyU Position A	PolyU Position B	Sai Wan Road Part 1
Shek Mun	Group 1	✓	✓	-
Day 1	Group 2	✓	✓	-
	Group 3	✓	✓	-
Shek Mun	Group 1	×	×	-
Day 2	Group 2	✓	✓	-
	Group 3	×	×	-
High Island Reservoir		-	-	×

6.5   Results and Discussions - Building Wall Finishes

The performances of the successful predictions in PolyU Position A and Position B testing datasets are summarized in Fig. 6.20 and 6.21 respectively. The calculated accuracies are the pixel accuracies of the defect predictions, whether each pixel could successfully return the correct label (i.e. defect (1) or no defect (0)). The performances of Group 1 and 2 training datasets built from the Shek Mun Day 1 thermal dataset,

and Group 2 training dataset from Day 2 thermal dataset on defect classification of the PolyU Position A testing dataset had accuracies (indicated as red lines in the figures) around 0.95. For Group 3 training dataset from the Day 1 thermal dataset, the accuracies of all the predictions ranged from 0.6 to 0.75, with precisions ranging from 0.1 to 0.2, and recalls ranging from 0.2 to 0.3. It was the logistic regression classifier with the poorest performance. There was a distinct pattern that could be observed in Group 1 and 2 in Fig. 6.20(a), 6.20(b), and 6.20(d) where emissivities are the highest, which the lines of F1-scores, precision and recall converged after the maximum temperatures of all the features on the sample wall appeared (i.e. frame 82 in this testing dataset). After the convergence happened, the precision continued increasing, while the recall started to decrease. The performances of the predictions in Position B testing dataset were different, as all four testing datasets had low F1 scores and precisions although the accuracies were all above 0.75. There was another pattern could be observed in Fig. 6.21, which the recalls of the predictions by Group 1 and 2 training datasets from the Shek Mun Day 1 thermal dataset, and Group 2 training dataset from Day 2 thermal dataset reached a maximum value close to 0.9 when the maximum temperatures of all the features on the sample wall appeared (i.e. frame 67 in this testing dataset). These observations are explained and the factors affecting the performance of the defect classification using the trained model are discussed in the following subsections.
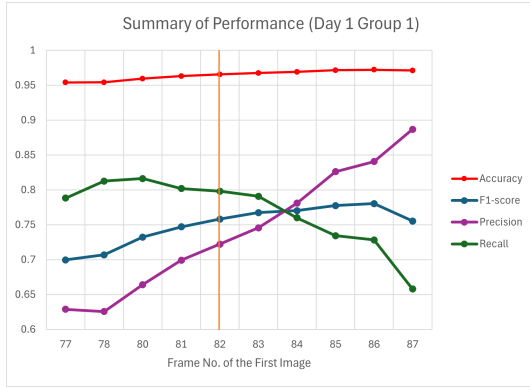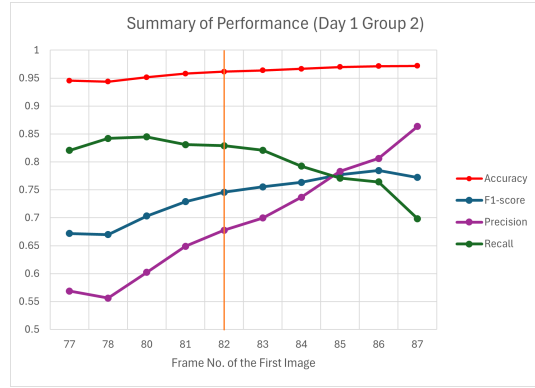
(a) Day 1 Group 1
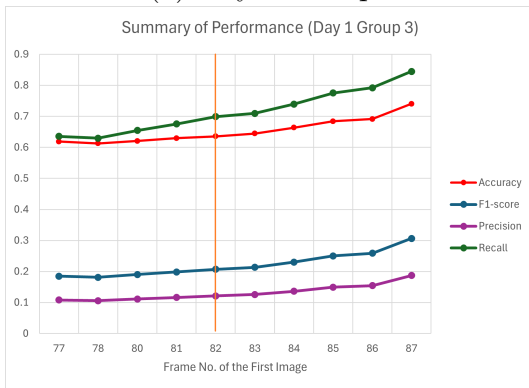
(b) Day 1 Group 2

(c) Day 1 Group 3
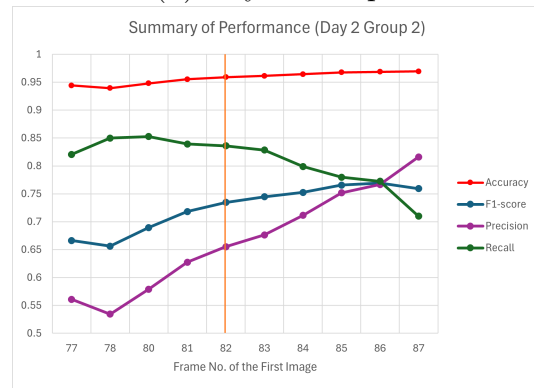
(d) Day 2 Group 2

Figure 6.20: Summary of Performance of Each Training Dataset for Position A Testing Dataset.

Remarks: Converging point of precision, recall and F1 score appeared right after the maximum temperatures of the features occurred. Orange lines marked the frame when the maximum temperature occurred.

(a) Day 1 Group 1

(b) Day 1 Group 2

(c) Day 1 Group 3

(d) Day 2 Group 2
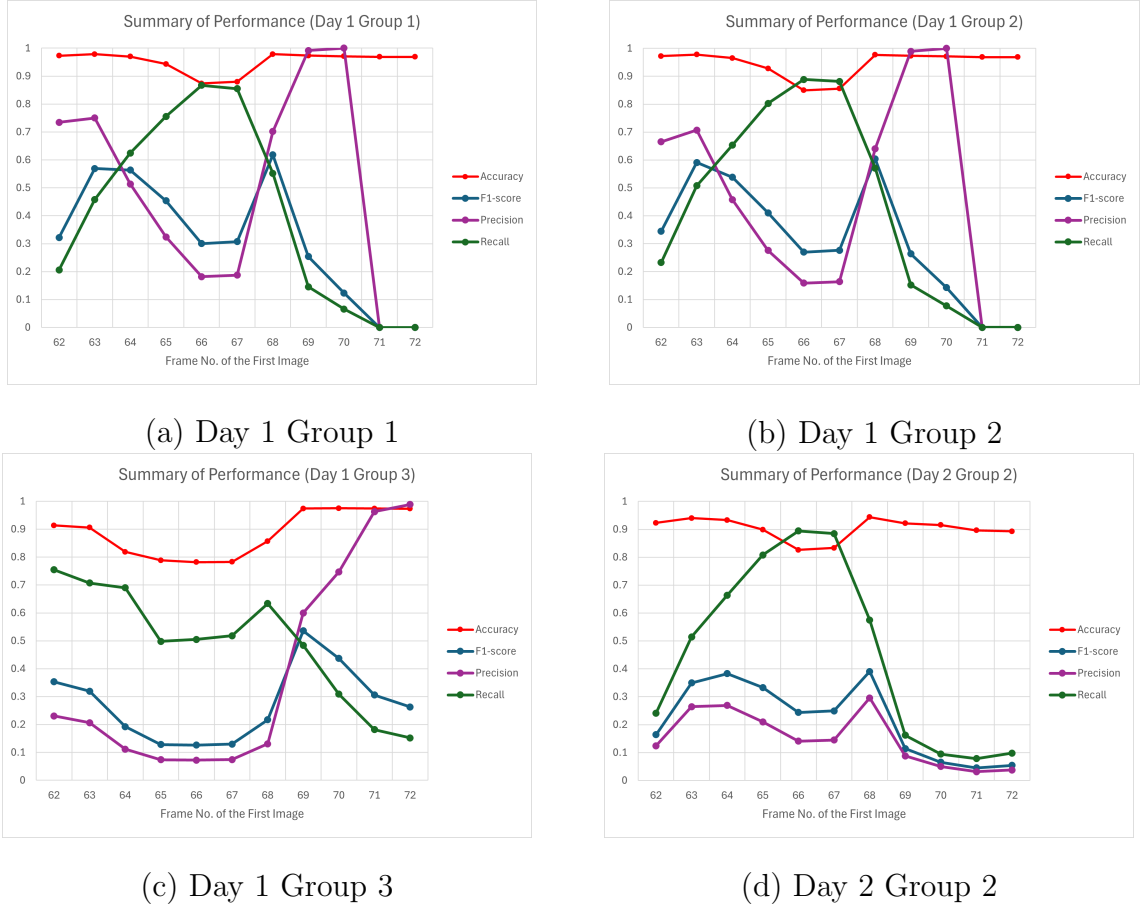
Figure 6.21: Summary of Performance of Each Training Dataset for Position B Testing Dataset.

6.5.1   Physical and Thermal Properties of Wall Finishes

The physical and thermal properties of the wall finishes on the target wall affect the choice of the logistic regression classifier. Referring to the feature spaces presented in the previous section (Section 6.3.1), the data points of the defects and the intact area in Group 1 materials had minimal overlapping area. The degree of overlapping increased slightly in Group 2 materials, and further increased in Group 3 materials. This suggested that the emissivity values of the wall finish materials play a significant role in affecting the performance of the logistic regression classification,

143

and it was necessary to develop the training datasets with different materials to ensure the classifier was suitable for the target surface. Hence, in this study, the training datasets were prepared according to the materials' emissivities.

The results of this study validated the above assumption. The wall finishes on the target wall at Position A were reddish-brown tiles and the texture of the tiles was similar to Smooth Black tiles of the eight wall finish materials used in Shek Mun's and Ping Che's sample wall. Based on the colours and the texture of the tiles, the emissivity of these tiles was assumed to be similar to those emissivity values in Group 2 materials, which are high emissivity materials. From Table 6.4 and Fig. 6.20, the prediction model using Group 2 training dataset as the logistic regression classifier successfully returned defect classification results at Position A with satisfactory performance (i.e. accuracies were around 0.95). The prediction model using Group 1 Day 1 training datasets as the classifiers could successfully return defect classification results, but the model using Group 1 Day 2 training dataset as the classifiers failed to return a prediction. This could be a result of the different ambient temperatures in the outdoor environment (Section 3.4), in which the average temperature on Day 1 was more similar to the average temperature on the surveying day at PolyU Position A. The performance of using Group 3 Day 1 training datasets as the classifier performed poorly and the model using Group 3 Day 2 training datasets could not perform prediction successfully. This emphasized the importance of choosing the correct classifiers to perform defect classification using the proposed machine learning method.

Another observation that needs to be addressed is that the change in wall finish materials might affect the performance of the machine learning method. Although the unwanted features were masked out before performing the predictions, the characteristics of the embedded defects at Position B were too significant, which affected the prediction results. Fig. 6.22 shows the visual image of the sample wall at Position B. The sample wall was constructed in an existing building (i.e. the rooftop of Block W

in PolyU), in which the original wall tiles were removed and defects (i.e. polystyrene foam plates) were embedded on the wall. Rendering was used to cover the embedded defects. This left marks on the position where the wall tiles were originally located. Even with the applied image mask and using a suitable logistic regression classifier (Group 1 Day 1 training datasets), the performance of the prediction results was unsatisfactory (Fig. 6.23).

Figure 6.22: Embedded defects and the marks on the sample wall at PolyU Position B.
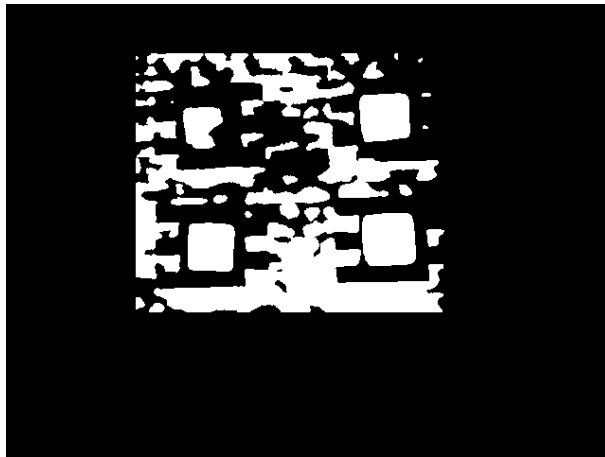
Figure 6.23: Defect classification on Position B testing dataset, using Group 1 Day 1 training datasets as the classifier.

6.5.2   Selection of the Images for Extracting the First Attributes for Training and Testing Dataset

As mentioned in the previous section (Section 6.2.1), the second attributes was extracted from the images chosen in the heat dissipation period (which normally occurred in the late afternoon and night), when the thermal contrast between the defects and the intact area became stable. Hence, determining which thermal images to use for extracting the second attributes for developing both training and testing datasets was a relatively easy task as long as the thermal images were taken at night. This means the selection of the images for extracting the first attributes highly affects the efficiency of the classifiers in the training dataset, and the prediction performance of the testing dataset. In this study, the thermal images taken during the heat absorption period were chosen, which includes the thermal image capturing the maximum thermal contrast between the defects and the intact area that occurred on the survey day. In Fig. 6.20, the convergence of the F1-score, precision and recall of the prediction performance occurred after the maximum temperatures appeared. Considering the trade-off between the precision and the recall, it is suggested to select a sequence of thermal images taken during the heat absorption period as the images for extracting the first attributes when developing the training dataset, and preparing the testing dataset in the machine learning method.

6.5.3   Depths and Thicknesses of Defects

The cover depths of the defects could affect the defect classification and size estimation using the proposed machine learning method. The defect classification result of the target wall at Position A predicted by the model using Shek Mun Day 1 Group 2 training dataset is illustrated in Fig. 6.24, marked with the estimated sizes of each suspected defect (in cm^2). All of the 6 embedded defects could be classified and used for size estimation. The true size of the embedded defects in this sample

wall is 400 cm^2, which the estimated size of Defect B is the closest (i.e. 402.43 cm^2) although the shape of the defect was deformed rather than in a perfect square shape. Defects A, B and C (upper rows, from right to left in the figure) had the same cover depth, but with different foam thicknesses (which were 12mm, 6mm, and 3 mm respectively). Based on the estimated sizes from the prediction result, the increase in the thicknesses of the defects could lead to underestimation. Regarding Defects D, E and F in the bottom rows with different foam thicknesses (i.e. 12mm, 6mm and 3mm) and cover depths (23mm, 29mm and 32 mm), Defect D was the shallowest, which the shallow cover depth compensated for the effect of thickness. Although Defect F was the thinnest defect among the three defects, the estimated size was overestimated. Similar to the findings in Section 4.5.2, deeper cover depths mean that the heat energy of the incident radiation experiences greater thermal absorption by the tiles due to the longer path length z (Eqs. 2.2 and 2.3). In addition, the incident radiation experiences omnidirectional dispersion along the lateral x and y directions, which explains the overestimation of Defect D. Therefore, the depths and thicknesses of the defects are important factors affecting the defect classification and size estimation using the machine learning method.
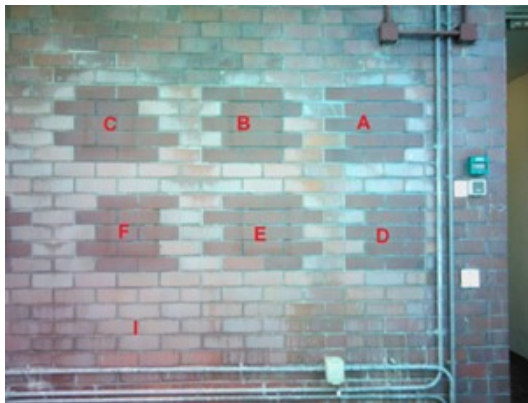
(a) Location of the embedded defects
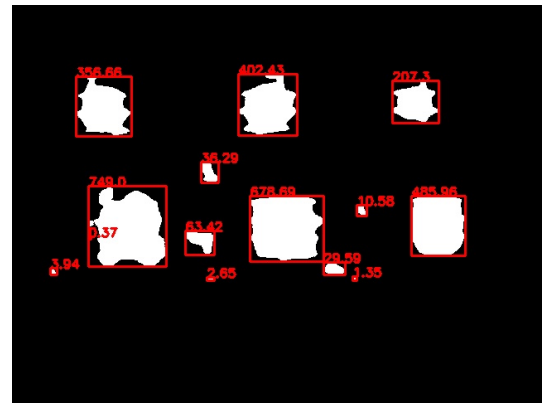
(b) Day 2 Group 2

Figure 6.24: Defect classification on Position A testing dataset, using Group 2 Day 1 training datasets as the classifier.

6.5.4   Orientation of Building

In the previous chapter regarding the Thermal Decay Mapping method, the orientation of the building is also one of the factors affecting the performance of defect classification using the machine learning method since it determines the selection of the images used for extracting the first attributes for developing the training and testing datasets. For East-facing targets, the optimal period for collecting the images for extracting the first attributes is the morning session, when the heat absorption period happens. Data collection of the targets facing towards the West shall take place in the afternoon session, as no solar radiation can reach the target surface in the morning. In this study, the data collected from a sample wall facing East (which was Shek Mun dataset) was used as the training dataset and the logistic regression classifiers for predicting the presence of the defects on a west-facing target (which was PolyU dataset). The results showed a positive defect classification result, which means it is not necessary to use a training dataset in the same orientation as the testing dataset, as long as they share a similar thermal behaviour during the data collection.

6.6   Results and Discussions - Rock Slopes

Unlike the successful defect classification in buildings, the developed training model could not provide a successful feature classification in slopes. The reasons leading to these results are summarized in the following sections.

6.6.1   Number of Data Points

The number of data points that could be used to develop the training dataset was limited. Unlike the training datasets used for building inspection, which had

more than 400,000 data points, the number of the training dataset used for secondary landslide hazard inspection was only 154,990. Although the thermal dataset collected in High Island Reservoir was by ground-based IRT in 5-minute intervals, data points from certain features, such as cracks and faults, were difficult to pick because of their quantity and small physical size. As the number of labelled data points in each class (i.e. types of features) in the training dataset should be balanced, this resulted in a training dataset with the limited number of data points, with no more than 40,000 data points for each class, which is only one fifth of the data points for each class in the training dataset for building inspection. Therefore, based on the results in this thesis, it is suggested that at least 200,000 data points for each class are needed to ensure sufficient data for developing the training dataset.

6.6.2 Distances Between Target and Thermal Camera

The thermal images in the building datasets were collected by ground-based IRT where the distances between the target and the thermal camera were short when compared to the thermal images in the slope datasets. During the data collection in High Island Reservoir, capturing the whole surface of the target slope was the first priority, and hence the distance between the target slope and the thermal camera was kept as close as possible, but it was still much farther than the distances between the sample wall and the thermal camera in the building datasets (i.e. 2.5m with a spatial resolution (IFOV) of 0.0939 cm^2 vs 24.78m with a spatial resolution (IFOV) of 9.23 cm^2). In the data collection on Sai Wan Road, a UAS was used to collect thermal images of a remote slope with landslide scars, where human access was impossible during that time, and the adoption of the UAS decreased the stability of the thermal camera. This resulted in a much larger distance between the thermal camera and the target surface, which was 115m. As mentioned in Section 2.3.7 regarding the limitations of IRT, increasing the distance between the target surface means decreasing the details of the thermal image. The effects of cracks/faults on the temperatures in the

area of small features would be averaged out, and hence reduce the thermal contrast value in that particular pixel, which further affected the detectability of such features when adopting the machine learning method proposed in this study.

6.6.3   Variety of Feature Type

From the feature space (in Fig. 6.14), only the data points of the vegetation could be separated from the other features. This demerit was shown in the bias-variance decomposition of the trained classifiers (Fig. 6.18). Feature classification on slopes was much more complicated than defect classification in building envelopes. In the defect classification for buildings in this study, there were only 2 features that needed to be classified, which were the defects and the intact area. However, in slope feature classification, the number of features to be classified was much greater, including the rock types and their weathering state, vegetation, cracks/faults, moisture, man-made structures, etc. The results presented in this study suggested that using only the thermal contrast in the features as the data points was insufficient in developing a prediction model for slope feature classification by the machine learning method. The thermal contrast value needs to be accompanied by other distinct characteristics from the targets to develop a successful machine learning model for slope feature classification, such as velocity from airborne radar.

6.7   Chapter Summary

The machine learning method proposed in this study was applied to the datasets consisting of different wall finish materials of buildings and features on slopes. The development of the proposed method and the application results for building inspection and secondary landslide hazard inspection were summarized in this chapter, which fulfilled the three objectives proposed in this study. The embedded defects in

each sample wall were visualized in binary images retrieved by the machine learning method and the sizes of the defects were estimated. For secondary landslide hazard inspection, the feature spacing stage suggested that vegetation could be separated from the other features. These findings fulfilled Objective 1 in this study, which was to classify defects and features. Factors affecting the accuracy of the machine learning method were summarized and discussed in this chapter, which included the physical and thermal properties of different wall finish materials, the depths and thicknesses of the defects and the orientation of the target surface. The results showed a successful implementation of the machine learning method in building inspection, and an attempt to apply the proposed method in secondary landslide hazard inspection. The factors affecting the criteria for the successful development of a prediction model were investigated, which fulfilled Objective 2 in this study. The performance of the proposed machine learning method was evaluated by the calculation of a confusion matrix, and several indices such as accuracy, precision and recall were calculated to assess the performance of the proposed method. This fulfilled Objective 3.

Summing up, this study validated the possibility of adopting the machine learning method in building inspection. With a suitable logistic regression classifier and the selection of the optimal first images for developing the training and testing dataset, the average accuracy of the defect detection could be achieved 0.95 with an F1 score of between 0.65 and 0.75. For secondary landslide hazard inspection, the findings in this study suggested that using the thermal contrast in features only for developing the training and testing dataset was insufficient to perform slope feature classification. Several factors led to this conclusion, including the number of data points in the training datasets, the distances between the thermal camera and the target surface affecting the spatial resolution (IFOV), and the variety of feature types. Based on the results presented in this chapter, it is suggested to select the prediction classifiers according to the materials' thermal properties like emissivities, and captured thermal images during the heat absorption period based on the orientation of the target

surface. To develop the machine learning model for classifying slope features, it is suggested to include other distinct features on the slopes to build the testing datasets with the thermal contrast values, which the thermal decay gradient value introduced in the previous chapter can be a potential feature to pair with. Nevertheless, the results in this chapter showed that it was possible to apply the machine learning method in automatic defect detection and size estimation of building structures, which is a step forward in building diagnosis.

Chapter 7

Conclusions and Recommendations

7.1 Chapter Overview

Summarizing the results of the application of the proposed methods in this study, this chapter concludes the major findings presented in this PhD study and whether the objectives of this study are satisfied. Recommendations for future work are given at last.

7.2 Major Findings and Conclusions

Overall, this thesis addresses the challenge when performing defect/feature classification in an outdoor environment, and presents the application of the Thermal Decay Mapping method and the machine learning method for defect/feature classification in two outdoor objects of interest with significant importance, which are building envelopes and slopes. Monitoring the health of buildings and slopes is important as the failures of these two objects will endanger the public. IRT is used to be regarded as a qualitative colour-dragging exercise to highlight the features, since

153

the colour span of a thermal image is normally determined by the user. This process is heavily biased by the judgment of the investigator, which could not reflect the real health of the buildings or slopes. Therefore, it is necessary to take a step forward in the industry, proving the potential of adopting IRT to assess the defects and estimate the sizes for better planning in the maintenance of both buildings and slopes. From the results in this study, the similarities of IRT inspections on building envelopes and secondary landslide hazards were identified. For example, the lack of automatic defect/feature classification leads to human bias in both analyses. Both inspections rely on observing the thermal contrast between the features and the intact area. The main concern of applying the proposed approaches in this thesis is to ensure the pedestrian safety by identifying potential hazards in both building envelopes and secondary landslide hazards, which is very common in Hong Kong. Since it is difficult to get access to both research objects, IRT analysis is the most common NDT technique to evaluate the risk of both research objects. Considering the above similarities, it is believed that the proposed approaches in this thesis can benefit the IRT inspection in both research objects, moving forward from the traditional qualitative analysis to a quantitative analysis which provides much more useful figures for identifying potential hazards. Through the proposed methods, an automatic defect/feature classification can be performed, which produces binary images containing the defects, and the major objectives of this study as established in Section 1.2 are all successfully fulfilled. The performances of the proposed methods are evaluated by the calculations of confusion matrices. The major findings of this study are summarized in the following sections.

7.2.1   Physical Approach - Thermal Decay Mapping Method

1. Defect/feature classification by this method returned successful results for both the building and secondary landslide hazard inspection, in which the thermal images taken from the instant of the maximum temperatures of the target sur-

face during the heat dissipation period were used for producing the Thermal Decay Map. The resulting Thermal Decay Map fulfilled part of Objective 1, which is to classify subsurface defects in building structures. The resulting Thermal Decay Map could be further enhanced by the SD method, which could improve the detectability of the suspected defects/features. With the aid of a suitable thresholding method, the defects/features could be segmented, and quantitative analysis could be performed, which fulfilled part of Objectives 2 and 3.

2. Building inspection: The effects of different wall finish materials on the application of the Thermal Decay Mapping method were analysed. The results showed that the average accuracy of the defect classification by the proposed method could be above 0.8, and the performance of the defect classification on building envelopes could be affected by the physical and thermal properties of the target's materials and the orientation of the target. It is suggested to add 0.5SD and 1.5SD in the ranges of colour representation of the resulting Thermal Decay Maps of the target wall covered with rendering and tiles respectively, before applying Otsu's thresholding to generate binary images of the suspected defects.

3. Secondary landslide hazard inspection: Features including vegetation, faults/cracks and moisture could be segmented from the resulting Thermal Decay Maps, and visualized in feature classification images. Physical and thermal properties of the target surface, such as the roughness of the slopes and the thermal conductivities of the features, could be the factors affecting the feature classification on slopes.

7.2.2 Statistical Approach - Machine Learning Method

1. Defect/feature classification by this method returned successful results for building inspection, where the sequences of thermal images captured in the heat absorption period when the instant of the maximum temperatures of the target surface occurred, and the thermal images taken in the heat dissipation period were used for developing the prediction model. The resulting model with the optimal logistic regression classifiers could successfully return predictions of suspected defects in the testing datasets, with an accuracy of 0.95 and an F1 score of 0.7, which fulfilled Objectives 1 to 3.

2. Building inspection: The selection of an appropriate logistic regression classifier should consider the physical and thermal properties of different wall finish materials. The results showed that the sequences of thermal images captured in the heat absorption period determined whether the trained model could return a successful prediction. The prediction returned a binary image containing the suspected defects on the target surface, on which quantitative analysis such as defect size estimation could be performed.

3. Secondary landslide hazard inspection: This study attempted to apply the machine learning method in secondary landslide hazard inspection, using the thermal contrast in features to develop the training model. However the trained model failed to return a prediction of the testing dataset, and the reasons for causing unfavourable prediction were concluded, including the limited number of data points, the variety of feature types and the distances between the thermal camera and the target.

7.2.3 Generic Workflow

Comparing the Thermal Decay Mapping method and the machine learning method, both methods could achieve accuracies up to 0.90. While the former does not require training a model and uses comparatively simple thresholding to perform the defect classification process, it still requires the user to define the ROI before performing the defect classification and size estimation because of the limitation posed by simple thresholding when dealing with defects in different cover depths. The machine learning method provides an overall defect classification and size estimation of the target surface with better accuracy, but this method requires sufficient data points for developing the prediction model beforehand, which becomes one of the reasons why the trained model failed to return a prediction for slopes. Based on the strengths and shortcomings of the proposed approaches, a generic workflow is established to provide a guideline for selecting the appropriate approach in different scenarios. The generic workflow for time-lapse and passive IRT by the proposed time-lapse Thermal Decay Mapping method and machine learning method is shown in Fig. 7.1. Based on the results in this thesis, when attempting a defect/feature classification adopting time-lapse IRT, the size of the existing data should be taken into consideration before selecting the appropriate approach. If the existing time-lapse thermal data could provide at least 200,000 data points for each feature class, the statistical approach (the Machine Learning method) can be used. Otherwise, the physical approach (the Thermal Decay Mapping method) can provide a more accurate result. After selecting the appropriate approach, several steps need to be taken to ensure a successful result. For the Thermal Decay Mapping method, the processing steps depend on the type of target that needs to be investigated. When dealing with buildings as the targets, it is suggested to apply Otsu's thresholding to perform the defect size estimation. When dealing with slopes, it is suggested to perform the segmentation by thermal decay gradient values and produce a segmentation map to visualize the identified features. For the Machine Learning method, it is suggested to apply image masking to

eliminate any unwanted features in the data before performing the prediction. This established workflow fulfilled Objective 4 in this thesis.
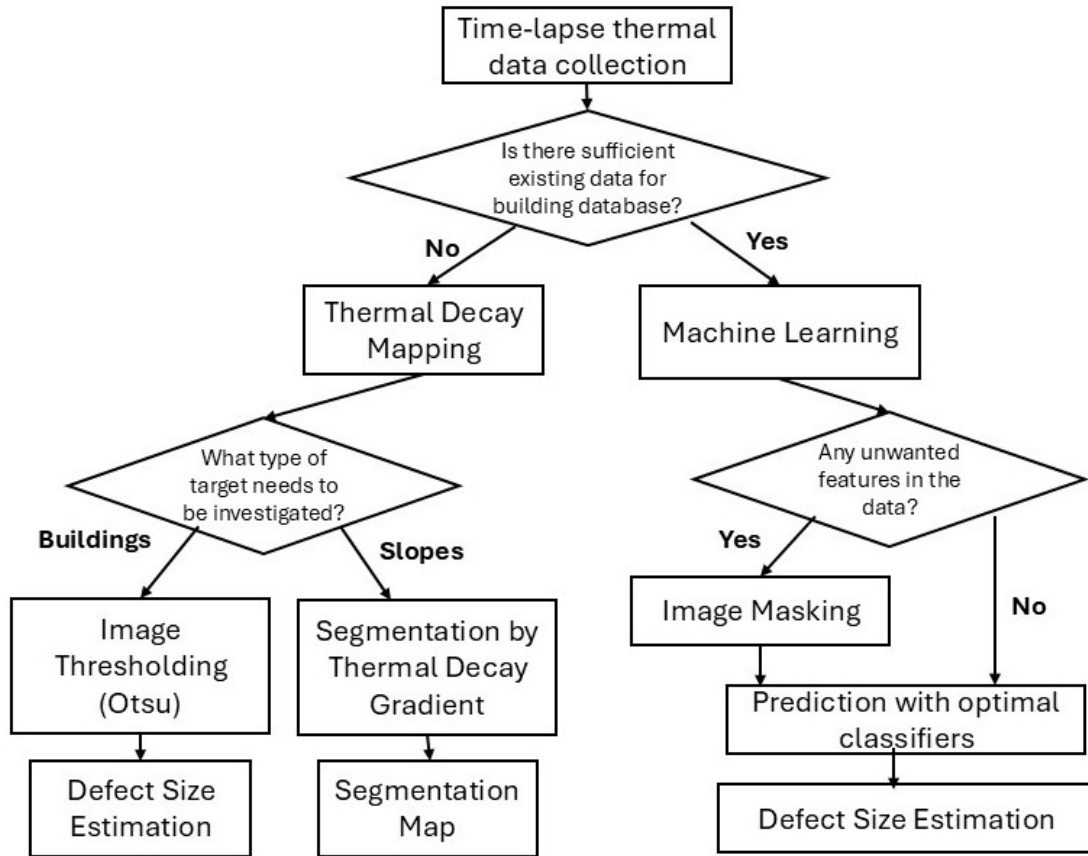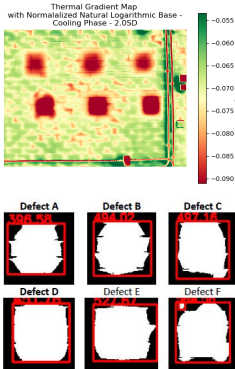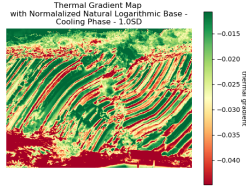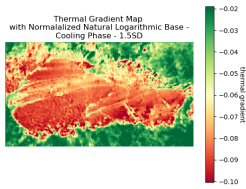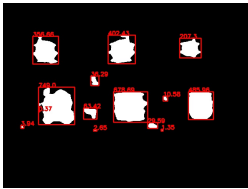
Figure 7.1: Generic workflow established in this thesis

Overall, the 4 objectives in this study were fulfilled, and IRT analyses on defect/feature classification by the proposed Thermal Decay Mapping method and the machine learning method using Logistic Regression were presented in this study, which were not seen in the research field. Table 7.1 provides a visualization of the overall results in this thesis.

Table 7.1: Overall results in this thesis

Method	Types of features		
	Building envelopes	Rock slopes in natural terrain	Soil slopes in natural terrain
Physical method - Thermal Decay Mapping	Binary - debond/ no debond Accuracy: 0.61−0.90 F1 score: 0.60- 0.91	Rock, dissolved rock, faults/ cracks, vegetation	Rock, dissolved rock, water, faults/cracks, vegetation, vegetation in landslide scars
Statistical method Supervised Machine Learning	Binary - debond/ no debond Average Accuracy: 0.95 F1 score: 0.65- 0.75	/	/

7.3 Recommendations

This study demonstrated the application of the Thermal Decay Mapping method and the machine learning method in the defect/feature classification for building and secondary landslide hazard inspection, in which the number of datasets used was

limited. Suggestions and recommendations for future studies are summarized in the following sections:

1. Case studies are suggested for validating the proposed methods in different scenarios. In this study, the sample walls used had their demerits, which could be observed in the results and findings. It is suggested to apply the proposed methods in real cases, starting from simply designed buildings, or slopes with direct access and ground truths. This can help to identify potential improvements and obstacles which are not addressed in this study.

2. In building inspection, the unwanted features on the target surface will affect the accuracy and the success rate of the prediction by both methods. It is suggested to investigate the possibility of adopting Artificial Intelligence (AI) such as deep learning to help eliminate these unwanted features automatically, as those unwanted features were excluded by a simple image mask in this study. Also, it is recommended to further investigate the development of an AI-based large model based on the proposed approaches in this thesis, since the proposed approaches still require data pre-processing manually.

3. For tall buildings, it is suggested to investigate the possibility of using a UAS equipped with a thermal camera for building inspection, since ground-based IRT has the restriction of angle of inclination when capturing the thermal images of the upper floors of the buildings.

4. For developing a machine learning model for classifying slope features, it is suggested to include other features with the thermal contrast in slope features. The thermal decay gradient obtained by the proposed Thermal Decay Mapping method could be a possible feature for the classification.

5. Seasonal effect: the data used in this thesis were mainly collected in the wintertime. The results of this thesis show that even when the data was collected

in the same season, the temperature evolution of the target varies according to the weather conditions, which caused the shift in the occurrence of maximum temperature during the survey day. Therefore it is suggested to further investigate how the seasonal effect affects the proposed approaches by applying data collected in summertime.

6. De-colourization of building materials: in existing buildings, the de-colourization of building envelopes is a common phenomenon in the outdoor environment. Since this thesis only performed and evaluated the proposed approaches on newly established sample walls, it is suggested to further investigate how the de-colourization of building materials changes the emissivity and hence the accuracy of the defect classification and size estimation.

7. Developing a building health record: it is suggested to further investigate the possibility of developing a building health record by the proposed approaches in this thesis. Since both approaches provide a visualization of the suspected defects/features on the target, by performing regular IRT inspection of the same target, comparison can be made to investigate whether there are any newly formed defects between consecutive inspections.

8. Defect classification by aspect ratio: the proposed approaches in this thesis were used to identify the suspected defects in both building envelopes and secondary landslide hazards, and perform a size estimation. It is suggested to further develop the proposed approaches by considering the aspect ratio of the defects to provide a more detailed defect analysis. By considering the aspect ratio of the defects, the suspected defects can be further classified according to their sizes and severity, which can be useful in maintenance planning.

9. Physics-guided model: the proposed approaches in this thesis took the thermal contrast between the defects/features and the intact area into main consideration, and provided successful defect/feature classification results. While IRT

analysis does not only involve temperature, it is suggested to investigate the possibility of taking other physical properties in developing a more physics-guided model, such as emissivity and frequency.

10. Thermal image stitching: it is suggested to stitch the thermal images of the whole buildings/slopes before doing the defect/feature classification, to avoid duplication of the defects/features. The challenges of thermal image stitching are its low spatial resolution, increasing geometric distortion, and signal loss, which are all challenges for the time-lapse Thermal Decay Mapping method and supervised machine learning. Hence further study on this topic is recommended.

Appendix A

Summary of Thermal Images Used for the Creation of Thermal Decay Map in Each Dataset

A.1   Building

A.1.1   Shek Mun Dataset

Table A.1: Summary of thermal images used for the creation of Thermal Decay Map in Shek Mun Day 1 dataset

Group	Material	Starting Frame (Time)	Ending Frame (Time)	Number of thermal images
1	Rendering	27 (10:38am)	71 (2:18pm)	45
2	Blue Mosaic	32 (11:03am)	64 (1:43pm)	33
2	Smooth Black	33 (11:08am)	64 (1:43pm)	32
2	Matt Black	31 (10:58am)	64 (1:43pm)	34
3	Grey Ceramic	31 (10:58am)	64 (1:43pm)	34
3	Reflective White	37 (10:28am)	64 (1:43pm)	28
3	White Mosaic	33 (11:08am)	65 (1:48pm)	33
3	Mixed Mosaic	33 (11:08am)	59 (1:18pm)	27

Table A.2: Summary of thermal images used for the creation of Thermal Decay Map in Shek Mun Day 2 dataset

Group	Material	Starting Frame (Time)	Ending Frame (Time)	Number of thermal images
1	Rendering	36 (11:00am)	76 (2:20pm)	41
2	Blue Mosaic	43 (11:35am)	69 (1:45pm)	27
2	Smooth Black	43 (11:35am)	69 (1:45pm)	27
2	Matt Black	43 (11:35am)	69 (1:45pm)	27
3	Grey Ceramic	43 (11:35am)	67 (1:35pm)	25
3	Reflective White	49 (12:05pm)	57 (12:45pm)	9
3	White Mosaic	43 (11:35am)	69 (1:45pm)	27
3	Mixed Mosaic	43 (11:35am)	69 (1:45pm)	27

Table A.3: Summary of thermal images used for the creation of Thermal Decay Map in Shek Mun Day 3 dataset

Group	Material	Starting Frame (Time)	Ending Frame (Time)	Number of thermal images
1	Rendering	32 (11:10am)	68 (2:10pm)	37
2	Blue Mosaic	35 (11:25am)	52 (12:50pm)	18
2	Smooth Black	32 (11:10am)	52 (12:50pm)	21
2	Matt Black	37 (11:35am)	52 (12:50pm)	16
3	Grey Ceramic	44 (12:10pm)	52 (12:50pm)	9
3	Reflective White	45 (12:15pm)	52 (12:50pm)	8
3	White Mosaic	45 (12:15pm)	52 (12:50pm)	8
3	Mixed Mosaic	34 (11:20am)	52 (12:50pm)	19

Appendix A. Summary of Thermal Images Used for the Creation of Thermal Decay Map in Each Dataset

A.1.2   Ping Che Dataset

Table A.4: Summary of thermal images used for the creation of Thermal Decay Map in Ping Che Day 1 dataset

Group	Material	Starting Frame (Time)	Ending Frame (Time)	Number of thermal images
1	Rendering	71 (3:47pm)	95 (5:47pm)	25
2	Blue Mosaic	72 (3:52pm)	95 (5:47pm)	24
2	Smooth Black	71 (3:47pm)	95 (5:47pm)	25
2	Matt Black	73 (3:57pm)	95 (5:47pm)	23
3	Grey Ceramic	73 (3:57pm)	95 (5:47pm)	23
3	Reflective White	71 (3:47pm)	95 (5:47pm)	25
3	White Mosaic	71 (3:47pm)	95 (5:47pm)	25
3	Mixed Mosaic	72 (3:52pm)	95 (5:47pm)	24

Table A.5: Summary of thermal images used for the creation of Thermal Decay Map in Ping Che Day 2 dataset

Group	Material	Starting Frame (Time)	Ending Frame (Time)	Number of thermal images
1	Rendering	64 (3:06pm)	96 (5:46pm)	33
2	Blue Mosaic	66 (3:16pm)	96 (5:46pm)	31
2	Smooth Black	64 (3:06pm)	96 (5:46pm)	33
2	Matt Black	66 (3:16pm)	96 (5:46pm)	31
3	Grey Ceramic	66 (3:16pm)	96 (5:46pm)	31
3	Reflective White	66 (3:16pm)	96 (5:46pm)	31
3	White Mosaic	66 (3:16pm)	96 (5:46pm)	31
3	Mixed Mosaic	66 (3:16pm)	96 (5:46pm)	31

A.1.3 PolyU Dataset

Table A.6: Summary of thermal images used for the creation of Thermal Decay Map in PolyU dataset

Position	Starting Frame (Time)	Ending Frame (Time)	Number of thermal images
A	84 (4:30pm)	127 (8:05pm)	44
B	68 (2:59pm)	89 (4:44pm)	22

A.2 Slope

Table A.7: Summary of thermal images used for the creation of Thermal Decay Map in High Island Reservoir and Sai Wan Road dataset

Dataset	Starting Frame (Time)	Ending Frame (Time)	Number of thermal images
High Island Reservoir	37 (2:41pm)	90 (7:06pm)	54
Sai Wan Road Part 1	4 (12:59pm)	15 (5:31pm)	11
Sai Wan Road Part 2	4 (12:59pm)	15 (5:31pm)	11

Appendix B

Program Code

B.1 Thermal Decay Mapping Method

B.1.1 Thermal Decay Map Production

```python
1  import os
2  import pandas as pd
3  import numpy as np
4  from numpy import isneginf
5  from glob import glob
6  import matplotlib.pyplot as plt
7
8  os.chdir("folder path")
9  strain = glob("*.csv")
10
11 ref_img = pd.read_csv("path of the first image", header=None)
12 arr = np.zeros((len(strain), ref_img.shape[0], ref_img.shape[1]))
13
14 i = 0
15 for filename in strain:
16     df = pd.read_csv(filename, header=None)
```

```
17
18     arr[i] = df.values
19     i = i + 1
20
21 arr_l = np.log(arr)
22 y = np.log(np.arange(0, (len(strain) * 5), 5)) # Change the interval
       according to dataset
23 y[isneginf(y)] = 0
24
25 arr_l_reshaped = arr_l.reshape(len(arr_l), -1)
26
27 slope = np.polyfit(y, arr_l_reshaped, 1)[0].reshape(ref_img.shape
       [0], ref_img.shape[1])
28 vmax = np.max(slope)
29 vmin = np.min(slope)
30
31 plt.imsave("path to save the resulting thermal decay map in png",
       slope, cmap='binary')
32 np.savetxt("path to save the resulting thermal decay map in csv",
       slope, delimiter=",")
33
34
35 # plot histogram of the original thermal decay map
36 plt.hist(slope,density=0)
37 plt.title(f"Histogram of All Features")
38 plt.xlabel("Thermal Decay Gradient")
39 plt.ylabel("Frequency")
40 plt.savefig(f'path to save the histogram of the resulting thermal
       decay map')
```

B.1.2 Thresholding - Adaptive Thresholding and Otsu's Thresholding

```
1 import cv2 as cv
```

169

```python
from matplotlib import pyplot as plt
import pandas as pd
from skimage import morphology

img = cv.imread("file path of the resulting thermal decay map", cv.
    IMREAD_GRAYSCALE)

# Read coordinates for selecting ROI
r = pd.read_csv("file path of the ROI coordinates", header=None, sep
    =',')

starting_x = r[0][0]
starting_y = r[0][1]

ending_x = r[1][0]
ending_y = r[1][1]

img_cropped_raw = img[starting_x:ending_x,
        starting_y:ending_y]

cv.imwrite("path to save the cropped Thermal Decay Map",
    img_cropped_raw)

# Apply Adaptive Thresholding
th1_raw = cv.adaptiveThreshold(img_cropped_raw, 255, cv.
    ADAPTIVE_THRESH_MEAN_C, cv.THRESH_BINARY, 3, 1)

# Apply Otsu's Thresholding
th2_raw = cv.threshold(img_cropped_raw, 0, 255, cv.THRESH_BINARY +
    cv.THRESH_OTSU)

# Remove small objects in the intact area
th1_raw = th1_raw > 0
th2_raw = th2_raw[1] > 0
```

```
31 th1_raw = morphology.remove_small_objects(th1_raw, min_size=30)
32 th2_raw = morphology.remove_small_objects(th2_raw, min_size=30)
33
34 # Save binary images
35 plt.imsave("path to save binary image produced by adaptive
      thresholding", th1_raw, cmap='gray')
36 plt.imsave("path to save binary image produced by adaptive
      thresholding", th2_raw, cmap='gray')
```

B.2 Machine Learning Method

B.2.1 Feature Spacing

```
1 import numpy as np
2 import matplotlib.pyplot as plt
3 from sklearn.preprocessing import MinMaxScaler, RobustScaler
4 import pandas as pd
5
6 folder = "path of the training dataset"
7 saved_folder = "path to save the plot"
8
9 fname = '{folder}.xlsx'
10
11 def dFS(fname):
12     data = pd.read_excel(fname)
13
14     X = data[['Contrast_AM', 'Contrast_PM']]
15     data['Label'] = data['Label'].astype(int)
16
17     scaler = MinMaxScaler() # Change to Robust Scaler when
    processing slope dataset
18     scaler.fit(X)
19     X_std = scaler.transform(X)
20
```

```
21    MAX = scaler.data_max_ # Change to center_ when processing slope
       dataset
22    MIN = scaler.data_min_ # Change to scale_ when processing slope
      dataset
23
24    X_std = pd.DataFrame({'Contrast_AM': X_std[:,0],'Contrast_PM':
      X_std[:,1], 'Label': data['Label']})
25    data = 0
26
27    return X_std, MAX, MIN
28
29 X_std, MAX, MIN= dFS(fname)
30
31 scatter_x = np.ravel(X_std['Contrast_AM'])
32 scatter_y = np.ravel(X_std['Contrast_PM'])
33 group = np.ravel(X_std['Label'])
34 cdict = {0: 'violet', 1: 'cornflowerblue'}
35
36 fig, ax = plt.subplots()
37 for g in np.unique(group):
38    ix = np.where(group == g)
39    ax.scatter(scatter_x[ix], scatter_y[ix], c=cdict[g], label=g, s
      =8)
40
41 plt.xlabel('Contrast_AM')
42 plt.ylabel('Contrast_PM')
43 plt.title('Tile Type 1')
44 ax.legend()
45 plt.savefig(f"{saved_folder}.jpg")
46 plt.close()
```

B.2.2   Bias-variance Decomposition

```
1 import matplotlib.pyplot as plt
2 from sklearn.linear_model import LogisticRegression
```

```
3 from sklearn.pipeline import make_pipeline
4 from sklearn.preprocessing import MinMaxScaler, RobustScaler,
       PolynomialFeatures
5 import pandas as pd
6 from sklearn import model_selection
7
8 folder = 'folder path containing the dataset'
9 fname = ''.join(folder + "/" + 'dataset filename')
10
11 def FS(fname):
12     data = pd.read_csv(fname)
13
14     X = data[['Contrast_AM', 'Contrast_PM']]
15     data['Label'] = data['Label'].astype(int)
16
17     scaler = MinMaxScaler()  # Change to Robust Scaler when
       processing slope dataset
18     scaler.fit(X)
19     X_std = scaler.transform(X)
20
21     MAX = scaler.data_max_  # Change to center_ when processing
       slope dataset
22     MIN = scaler.data_min_  # Change to scale_ when processing slope
        dataset
23
24     X_std = pd.DataFrame({'Contrast_AM': X_std[:, 0], 'Contrast_PM':
        X_std[:, 1], 'Label': data['Label']})
25
26     return X_std, MAX, MIN
27
28
29 X_std, MAX, MIN = FS(fname)
30
31 X_std = X_std[['Contrast_AM','Contrast_PM']]
```

173

```
32 data = pd.read_csv(fname)
33 y1 = data['Label']
34
35 D_error = []
36 V_error = []
37
38 degree_min=1
39 degree_max=12
40
41 for degree in range(degree_min,degree_max+1):
42     print('d:',degree)
43     model_logo = make_pipeline(PolynomialFeatures(degree=degree,
       interaction_only=False, include_bias=False), LogisticRegression(C
       =1,class_weight='balanced', max_iter=100000, solver='lbfgs',
       multi_class='multinomial', penalty='l2'))
44     results_logo = model_selection.cross_validate(model_logo, X_std,
        y1, cv=None, scoring='f1_weighted', return_train_score=True)
45
46     train_error = results_logo['train_score'].mean()
47     D_error.append(train_error)
48     test_error = results_logo['test_score'].mean()
49     V_error.append(test_error)
50
51 ee = pd.DataFrame(data=zip(D_error, V_error), columns=['Dev','Val'])
52
53 fig, ax1 = plt.subplots(figsize=(4.5, 3))
54
55 ax1.set_ylabel('Weighted F1-Score')
56 ax1.set_xlabel('Degree of Polynomial')
57 ax1.plot(range(degree_min,degree_max+1), D_error, 'r', marker="s",
       label='Dev.')
58 ax1.plot(range(degree_min,degree_max+1), V_error, 'g', marker ="o",
       label ='Val.')
59 ax1.legend(loc=0)
```

```
60 ax1.set_ylim(ee['Val'].min()-0.01, ee['Dev'].max()+0.01)
61
62 t = ''.join('Logistic Regression , C: '+ str(1))
63 plt.title(t)
64 fig.tight_layout()
65 fig.savefig(fname =f'path to save the plot', dpi =600, format='jpg')
66 plt.show()
```

B.2.3 Prediction

```
1  from __future__ import division
2
3  import pandas as pd
4  import numpy as np
5  from sklearn.linear_model import LogisticRegression
6  from sklearn.preprocessing import PolynomialFeatures
7  from sklearn.pipeline import make_pipeline
8  import matplotlib.pyplot as plt
9  from matplotlib import colors
10 from Feature_Scaling import FS
11
12 my_dpi = 96
13
14 # Calculating IFOV
15 distance = 2.8625
16 horizontal_pixel = 640
17 vertical_pixel = 480
18
19 fname = 'path of the dataset to be used as classifier'
20 data, MAX, MIN = FS(fname)
21
22 X_train = data[['Contrast_AM', 'Contrast_PM']]
23 data['Label'] = data['Label'].astype(int)
24 y_train = data['Label']
25
```

```
26 # choose the image to be processed
27 X_test = pd.read_excel(r'path of the image to be predicted',
       sheet_name=['Contrast_AM', 'Contrast_PM'], header=None)
28 condition = ['Intact', 'Defected']
29
30 Contrast_AM = X_test['Contrast_AM']
31 Contrast_AM = -Contrast_AM
32 Contrast_PM = X_test['Contrast_PM']
33
34 Contrast_AM = (Contrast_AM-MIN[1])/(MAX[1]-MIN[1])
35 Contrast_PM = (Contrast_PM-MIN[0])/(MAX[0]-MIN[0])
36
37 lr = make_pipeline(PolynomialFeatures(degree=5, interaction_only=
       False, include_bias=False),
38                    LogisticRegression(C=1, max_iter=5000,
       class_weight='balanced', solver='lbfgs', multi_class='multinomial
       ', penalty='l2'))
39 lr.fit(X_train, y_train)
40 Z = lr.predict(np.c_[np.ravel(Contrast_PM), np.ravel(Contrast_AM)])
41
42 Z = Z.reshape(Contrast_PM.shape)
43
44 delta_x = (round(horizontal_pixel)/10)/Contrast_PM.shape[1]
45 delta_y = (round(vertical_pixel)/10)/Contrast_PM.shape[0]
46 x = np.arange(0, Contrast_PM.shape[1]*delta_x, delta_x)
47 y = np.arange(0, Contrast_PM.shape[0]*delta_y, delta_y)
48 X, Y = np.meshgrid(x, y)
49
50 cmap = colors.ListedColormap(['black', 'cornflowerblue', '
       forestgreen', 'white'])
51 bounds = [-1, 0, 1]
52 norm = colors.BoundaryNorm(bounds, cmap.N)
53 plt.figure(figsize=(horizontal_pixel/0.775/my_dpi, vertical_pixel
       /0.769/my_dpi))
```

```
54 CS = plt.contourf(X, Y, Z, cmap=cmap, norm=norm, levels=bounds)
55 plt.gca().invert_yaxis()
56 plt.axis('off')
57 plt.savefig('path to save the prediction image', bbox_inches='tight'
      , transparent=True, pad_inches=0, dpi=my_dpi)
```

B.3   Common Code for Both Methods

B.3.1   Size Estimation

```
1 import cv2
2
3 # read image
4 img = cv2.imread('path of the binary image')
5
6 distance = 2.8625 # distance between the camera and the target
7
8 horizontal_cm = 45/640 * 17.44 / 1000 * distance * 100 # Change the
      parameters here when using other camera model
9 vertical_cm = 33.7/480 * 17.44 / 1000 * distance * 100
10
11 area_per_pixel = horizontal_cm * vertical_cm
12
13 gray = cv2.cvtColor(img, cv2.COLOR_BGR2GRAY)
14 thresh = cv2.threshold(gray, 128, 255, cv2.THRESH_BINARY)[1]
15
16 # get contours
17 result = img.copy()
18 contours = cv2.findContours(thresh, cv2.RETR_EXTERNAL, cv2.
      CHAIN_APPROX_SIMPLE)
19 contours = contours[0] if len(contours) == 2 else contours[1]
20 for cntr in contours:
21     x, y, w, h = cv2.boundingRect(cntr)
22     cv2.rectangle(result, (x, y), (x + w, y + h), (0, 0, 255), 2)
```

```
23    area = cv2.contourArea(cntr)
24    total_area = area_per_pixel * area
25
26    cv2.putText(result, str(round(total_area, 2)), (x, y),
27               cv2.FONT_HERSHEY_SIMPLEX, 0.5, (0, 0, 255), 2)
28
29 # save resulting image
30 cv2.imwrite('path to save the size estimation image', result)
31
32 # show thresh and result
33 cv2.imshow("bounding_box", result)
34 cv2.waitKey(0)
35 cv2.destroyAllWindows()
```

B.3.2   Confusion Matrix

```
1 import matplotlib.pyplot as plt
2 from sklearn.metrics import ConfusionMatrixDisplay, confusion_matrix
3 import csv
4 import numpy as np
5
6 header = ['Accuracy', 'Precision', 'Recall', 'F1-score', 'TPR', 'TNR
      ', 'FPR']
7
8 gt = np.genfromtxt('path of the ground truth in csv', delimiter=',')
9 predict = np.genfromtxt(f'path of the binary image in csv',
      delimiter=',')
10 labels = [1, 0]
11
12 matrix = confusion_matrix(gt, predict)
13 cm = ConfusionMatrixDisplay(confusion_matrix=matrix, display_labels=
      labels)
14 cm.plot()
15 plt.xticks(fontsize=15)
16 plt.yticks(fontsize=15)
```

```
17 plt.title('Confusion Matrix', fontsize=15)
18 plt.savefig('path to save the confusion matrix image', transparent=
       True, dpi=500)
19 plt.cla()
20 plt.close()
21
22 tn, fp, fn, tp = confusion_matrix(gt, predict).ravel()
23
24 ac_raw = float((tp + tn) / (tp + tn + fp + fn))
25
26 if tp == 0 and fp == 0:
27     p_raw = 0
28 else:
29     p_raw = float(tp / (tp + fp))
30
31 r_raw = float(tp / (tp + fn))
32
33 if p_raw == 0 and r_raw == 0:
34     f1_raw = 0
35 else:
36     f1_raw = float(2 * (p_raw * r_raw) / (p_raw + r_raw))
37
38 tpr_raw = float(tp / (tp + fn))
39
40 tnr_raw = float(tn / (tn + fp))
41
42 fpr_raw = float(fp/ (tn + fp))
43
44 tuple_raw = (ac_raw, p_raw, r_raw, f1_raw, r_raw, tnr_raw, fpr_raw)
45
46 list_raw =  map(lambda x: x, tuple_raw)
47
48 header = ['Accuracy', 'Precision', 'Recall', 'F1-score', 'TPR', 'TNR
       ', 'FPR']
```

```
49
50  with open (f"path to save the errors in csv", 'w', encoding='UTF8',
        newline='') as f:
51      writer = csv.writer(f)
52
53      writer.writerow(header)
54
55      writer.writerow(list_raw)
```

References

[1] Takahide Sakagami and Shiro Kubo. Development of a new non-destructive testing technique for quantitative evaluations of delamination defects in concrete structures based on phase delay measurement using lock-in thermography. *Infrared physics & technology*, 43(3):311–316, 2002. `doi:10.1016/S1350-4495(02)00157-3`.

[2] Joaquin Humberto Aquino-Rocha, Yêda Vieira Póvoas, and Pedro Igor Bezerra-Batista. Flaw recognition in reinforced concrete bridges using infrared thermography: A case study. *Revista Facultad de Ingeniería*, (110):99–109, 2024. `doi:10.17533/udea.redin.20230521`.

[3] Muflih Alhammad, Nicolas P. Avdelidis, Clemente Ibarra-Castanedo, Muhammet E. Torbali, Marc Genest, Hai Zhang, Argyrios Zolotas, and Xavier P. V. Maldgue. Automated impact damage detection technique for composites based on thermographic image processing and machine learning classification. *Sensors (Basel, Switzerland)*, 22(23):9031, 2022. `doi:10.3390/s22239031`.

[4] G. V. P. Chandra Sekhar Yadav, V. S. Ghali, and N. R. Baloji. A time frequency-based approach for defect detection in composites using nonstationary thermal wave imaging. *Russian journal of nondestructive testing*, 57(6):486–499, 2021. `doi:10.1134/S1061830921060061`.

[5] F. Cerdeira, M. E. Vázquez, J. Collazo, and E. Granada. Applicability of infrared thermography to the study of the behaviour of stone panels as building envelopes. *Energy and buildings*, 43(8):1845–1851, 2011. `doi:10.1016/j.enbuild.2011.03.029`.

[6] Michael Y. L. Chew and Vincent J. L. Gan. Long-standing themes and future prospects for the inspection and maintenance of façade falling objects from tall buildings. *Sensors (Basel, Switzerland)*, 22(16):6070, 2022. ObjectType-Article-2. `doi:10.3390/s22166070`.

[7] Buildings Department. Code of Practice for The Mandatory Building Inspection Scheme and The Mandatory Window Inspection Scheme 2012 (2023 Edition), 2023. URL: `https://www.bd.gov.hk/doc/en/safety-and-inspection/mbis/registered-inspectors-and-registered-contractors/CoP_MBIS_MWISe.pdf`.

[8] Siu Ming Lo. The use of thermography for the detection of external finishes defects of buildings in hong kong. *Structural survey*, 17(1):22–26, 1999. ark:/67375/4W2-74DT854S-S. `doi:10.1108/02630809910258683`.

[9] HOKLAS. HOKLAS Supplementary Criteria No. 19 Construction Materials Test Category - Accreditation of Diagnostic Tests on Concrete, 2018. URL: `https://www.itc.gov.hk/en/quality/hkas/doc/SupplementaryCriteria/HOKLAS_SC-19.pdf`.

[10] Wallace Wai Lok Lai, Ka Kin Lee, and Chi Sun Poon. Validation of size estimation of debonds in external wall's composite finishes via passive infrared thermography and a gradient algorithm. *Construction and Building Materials*, 87:113–124, 2015. `doi:10.1016/j.conbuildmat.2015.03.032`.

[11] W. L. Lai, K. K. Lee, S. C. Kou, C. S. Poon, and W. F. Tsang. A study of full-field debond behaviour and durability of cfrp-concrete composite beams

by pulsed infrared thermography (irt). *NDT and E International*, 52:112–121, 2012. `doi:10.1016/j.ndteint.2012.07.001`.

[12] Government of the Hong Kong Special Administrative Region. 601 landslide reports in 2023, May 27, 2024 2024. URL: `https://www.news.gov.hk/eng/2024/05/20240527/20240527_150907_819.html`.

[13] Geotechnical Engineering Office. GEO Report No. 376 - Detailed Study of the 8 and 14 September 2023 Landslides on Slope No. 11SE-D/F47 at Shek O Road, Shek O. Report, Geotechnical Engineering Office,, 2024.

[14] Zheng-fang Wang, Yan-fei Yu, Jing Wang, Jian-qing Zhang, Hong-liang Zhu, Peng Li, Lei Xu, Hao-nan Jiang, Qing-mei Sui, Lei Jia, and Jiang-ping Chen. Convolutional neural-network-based automatic dam-surface seepage defect identification from thermograms collected from uav-mounted thermal imaging camera. *Construction & building materials*, 323:126416, 2022. `doi:10.1016/j.conbuildmat.2022.126416`.

[15] Chia-Chi Cheng, Tao-Ming Cheng, and Chih-Hung Chiang. Defect detection of concrete structures using both infrared thermography and elastic waves. *Automation in construction*, 18(1):87–92, 2008. ObjectType-Article-2. `doi:10.1016/j.autcon.2008.05.004`.

[16] Gene F. Sirca and Hojjat Adeli. Infrared thermography for detecting defects in concrete structures. *Journal of civil engineering and management*, 24(7):508–515, 2018. `doi:10.3846/jcem.2018.6186`.

[17] Ali K. Saleh, Zafer Sakka, and Hasan Almuhanna. The application of two-dimensional continuous wavelet transform based on active infrared thermography for subsurface defect detection in concrete structures. *Buildings (Basel)*, 12(11):1967, 2022. `doi:10.3390/buildings12111967`.

[18] P. Bagavac, L. Krstulović-Opara, and Ž Domazet. Enhancing ir thermographic inspection of subsurface defects by using the technique of edge detection. *Russian journal of nondestructive testing*, 57(7):609–618, 2021. `doi: 10.1134/S1061830921070020`.

[19] Hyun-Tae Bang, Solmoi Park, and Haemin Jeon. Defect identification in composite materials via thermography and deep learning techniques. *Composite structures*, 246:112405, 2020. `doi:10.1016/j.compstruct.2020.112405`.

[20] Qiwen Qiu. Imaging techniques for defect detection of fiber reinforced polymer-bonded civil infrastructures. *Structural control and health monitoring*, 27(8):n/a, 2020. `doi:10.1002/stc.2555`.

[21] Ming Bao and Na Zhang. Enhanced methodology for building surface inspection using infrared thermography and numerical simulation. *Traitement du signal*, 41(3):1527–1537, 2024. `doi:10.18280/ts.410340`.

[22] Cheng Zhang, Yang Zou, Johannes Dimyadi, and Vicente Gonzalez. Uav thermography for building energy audit: Comparing image acquisition strategies. volume 41, pages 1144–1151. IAARC Publications.

[23] Stefano Sfarra, Antonio Cicone, Bardia Yousefi, Clemente Ibarra-Castanedo, Stefano Perilli, and Xavier Maldague. Improving the detection of thermal bridges in buildings via on-site infrared thermography: The potentialities of innovative mathematical tools. *Energy and buildings*, 182:159–171, 2019. `doi:10.1016/j.enbuild.2018.10.017`.

[24] Marco Puliti, Giovanni Montaggioli, and Alessandro Sabato. Automated subsurface defects' detection using point cloud reconstruction from infrared images. *Automation in construction*, 129:103829, 2021. `doi:10.1016/j.autcon.2021. 103829`.

[25] S. Lagüela, J. Armesto, P. Arias, and J. Herráez. Automation of thermographic 3d modelling through image fusion and image matching techniques. *Automation in construction*, 27:24–31, 2012. ObjectType-Article-2. `doi: 10.1016/j.autcon.2012.05.011`.

[26] M. Hasan Shariq and Ben Richard Hughes. Revolutionising building inspection techniques to meet large-scale energy demands: A review of the state-of-the-art. *Renewable & sustainable energy reviews*, 130:109979, 2020. `doi:10.1016/ j.rser.2020.109979`.

[27] Mariluz Gil-Docampo, Juan Ortiz Sanz, Ignacio Cañas Guerrero, and Manés Fernández Cabanas. Uas ir-thermograms processing and photogrammetry of thermal images for the inspection of building envelopes. *Applied sciences*, 13(6):3948, 2023. `doi:10.3390/app13063948`.

[28] Mengyang Guo. *Spatially resolved infrared imaging for building performance evaluation*. Thesis, 2016.

[29] Jian-Hong Wu, Hung-Ming Lin, Der-Her Lee, and Shih-Chieh Fang. Integrity assessment of rock mass behind the shotcreted slope using thermography. *Engineering geology*, 80(1):164–173, 2005. `doi:10.1016/j.enggeo.2005.04.005`.

[30] Giordano Teza, Gianluca Marcato, Eugenio Castelli, and Antonio Galgaro. Irtrock: A matlab toolbox for contactless recognition of surface and shallow weakness of a rock cliff by infrared thermography. *Computers & geosciences*, 45:109–118, 2012. `doi:10.1016/j.cageo.2011.10.022`.

[31] Ivo Baron, David Beckovsky, and Lumir Mica. Application of infrared thermography for mapping open fractures in deep-seated rockslides and unstable cliffs. *Landslides*, 11(1):15–27, 2014. `doi:10.1007/s10346-012-0367-z`.

[32] William Frodella, Giovanni Gigli, Stefano Morelli, Luca Lombardi, and Nicola Casagli. Landslide mapping and characterization through infrared thermog-

raphy (irt): Suggestions for a methodological approach from some case studies. *Remote sensing (Basel, Switzerland)*, 9(12):1281, 2017. `doi:10.3390/rs9121281`.

[33] G. Pappalardo, S. Mineo, A. C. Angrisani, D. Di Martire, and D. Calcaterra. Combining field data with infrared thermography and dinsar surveys to evaluate the activity of landslides: the case study of randazzo landslide (ne sicily). *Landslides*, 15(11):2173–2193, 2018. `doi:10.1007/s10346-018-1026-9`.

[34] Robert K. Vincent and Fred Thomson. Spectral compositional imaging of silicate rocks. *J. Geophys. Res*, 77(14):2465–2472, 1972. `doi:10.1029/JB077i014p02465`.

[35] Philip R. Christensen, Joshua L. Bandfield, Victoria E. Hamilton, Douglas A. Howard, Melissa D. Lane, Jennifer L. Piatek, Steven W. Ruff, and William L. Stefanov. A thermal emission spectral library of rock-forming minerals. *J. Geophys. Res*, 105(E4):9735–9739, 2000. `doi:10.1029/1998JE000624`.

[36] Shahrzad Roshankhah. *Physical properties of geomaterials with relevance to thermal energy geo-systems*. Thesis, 2015.

[37] S. Mineo and G. Pappalardo. The use of infrared thermography for porosity assessment of intact rock. *Rock mechanics and rock engineering*, 49(8):3027–3039, 2016. `doi:10.1007/s00603-016-0992-2`.

[38] S. Mineo, G. Pappalardo, F. Rapisarda, A. Cubito, and G. Di Maria. Integrated geostructural, seismic and infrared thermography surveys for the study of an unstable rock slope in the peloritani chain (ne sicily). *Engineering geology*, 195:225–235, 2015. `doi:10.1016/j.enggeo.2015.06.010`.

[39] Antoine Guerin, Michel Jaboyedoff, Brian D. Collins, Greg M. Stock, Marc-Henri Derron, Antonio Abellán, and Battista Matasci. Remote thermal de-

tection of exfoliation sheet deformation. *Landslides*, 18(3):865–879, 2020. `doi:10.1007/s10346-020-01524-1`.

[40] William Frodella, Daniele Spizzichino, Giovanni Gigli, Mikheil Elashvili, Claudio Margottini, Alberto Villa, Paolo Frattini, Giovanni Crosta, and Nicola Casagli. Integrating kinematic analysis and infrared thermography for instability processes assessment in the rupestrian monastery complex of david gareja (georgia), 2020. `doi:10.1007/978-3-030-60196-6_36`.

[41] Guglielmo Grechi, Matteo Fiorucci, Gian Marco Marmoni, and Salvatore Martino. 3d thermal monitoring of jointed rock masses through infrared thermography and photogrammetry. *Remote sensing (Basel, Switzerland)*, 13(5):1–25, 2021. `doi:10.3390/rs13050957`.

[42] Marco Loche, Gianvito Scaringi, Jan Blahůt, Maria Teresa Melis, Antonio Funedda, Stefania Da Pelo, Ivan Erbì, Giacomo Deiana, Mattia Alessio Meloni, and Fabrizio Cocco. An infrared thermography approach to evaluate the strength of a rock cliff. *Remote sensing (Basel, Switzerland)*, 13(7):1265, 2021. `doi:10.3390/rs13071265`.

[43] G. Pappalardo, S. Mineo, S. Perriello Zampelli, A. Cubito, and D. Calcaterra. Infrared thermography proposed for the estimation of the cooling rate index in the remote survey of rock masses. *International journal of rock mechanics and mining sciences (Oxford, England : 1997)*, 83:182–196, 2016. `doi:10.1016/j.ijrmms.2016.01.010`.

[44] Lydia Sin-Yau Chiu, Wallace Wai-Lok Lai, Sónia Santos-Assunção, Sahib Singh Sandhu, Janet Fung-Chu Sham, Nelson Fat-Sang Chan, Jeffrey Chun-Fai Wong, and Wai-Kin Leung. A feasibility study of thermal infrared imaging for monitoring natural terrain—a case study in hong kong. *Remote sensing (Basel, Switzerland)*, 15(24):5787, 2023. `doi:10.3390/rs15245787`.

[45] Xavier Maldague and Patrick O. Moore. *Infrared and thermal testing.* American Society for Nondestructive Testing, Columbus, OH, 3rd ed.. edition, 2001.

[46] Thomas Johann Seebeck. *Magnetische polarisation der metalle und erze durch temperatur-differenz.* W. Engelmann, 1895.

[47] ASTM. ASTM D4788 Standard test method for detecting delaminations in bridge decks using infrared thermography (Reapproved 2022), 15 April 2022 2022. URL: `www.astm.org`.

[48] Hong Kong Concrete Institute. Detection of external wall debonding/delamination by infrared thermography (issue 2), 2022. URL: `http://www.hongkongci.org/wp-content/uploads/2022/08/HKCI-TM1-2022.pdf`.

[49] Xavier Maldague. *Theory and practice of infrared technology for nondestructive testing.* Wiley series in microwave and optical engineering. Wiley, New York ;, 2001.

[50] Mrinal Kanti Bhowmik. Thermal infrared face recognition – a biometric identification technique for robust security system, 2011. MODID-6d55e02e354:IntechOpen. `doi:10.5772/18986`.

[51] Sahar Hassani and Ulrike Dackermann. A systematic review of advanced sensor technologies for non-destructive testing and structural health monitoring. *Sensors (Basel, Switzerland)*, 23(4):2204, 2023. ObjectType-Article-2. `doi:10.3390/s23042204`.

[52] David P DeWitt and Gene D Nutter. *Theory and practice of radiation thermometry.* John Wiley & Sons, 1988.

[53] Tommaso Astarita and G. M. Carlomagno. *Infrared thermography for thermo-fluid-dynamics.* Springer Science & Business Media, 2012. Includes bibliographical references and index.

[54] Michael Vollmer and Klaus-Peter Möllmann. *Infrared Thermal Imaging: Fundamentals, Research and Applications.* John Wiley & Sons, Incorporated, Newark, second edition. edition, 2018. `doi:10.1002/9783527693306`.

[55] FP Incropera and David P De Witt. Fundamentals of heat and mass transfer, third edit. ed. jonn wiley & sons, 1990.

[56] Vedat S. Arpaci. *Conduction heat transfer.* Addison-Wesley series in mechanics and thermodynamics. Addison-Wesley Pub. Co., Reading, Mass, 1966.

[57] W. Swiderski and V. Vavilov. Ir thermographic detection of defects in multi-layered composite materials used in military applications. pages 553–556. IEEE, 2007. `doi:10.1109/ICIMW.2007.4516626`.

[58] A. Moropoulou, N. P. Avdelidis, M. Koui, and K. Kakaras. An application of thermography for detection of delaminations in airport pavements. *NDT & E international : independent nondestructive testing and evaluation*, 34(5):329–335, 2001. ObjectType-Article-2. `doi:10.1016/S0963-8695(00)00047-5`.

[59] Bu Chiwu, Tao Liu, Rui Li, Bo Zhao, and Qingju Tang. Infrared image segmentation algorithm based on multi structure morphology—pulse coupled neural network in application to the inspection of aerospace materials. *Russian journal of nondestructive testing*, 57(11):1018–1026, 2021. `doi:10.1134/S1061830921110061`.

[60] Zongjin Li, Wu Yao, Stephen Lee, Chihung Lee, and Zhiyu Yang. Application of infrared thermography technique in building finish evaluation. *Journal of nondestructive evaluation*, 19(1):11–19, 2000. ObjectType-Article-2. `doi:10.1023/A:1006612023656`.

[61] C. A. Balaras and A. A. Argiriou. Infrared thermography for building diagnostics. *Energy & Buildings*, 34(2):171–183, 2002. `doi:10.1016/S0378-7788(01)00105-0`.

[62] Tommy Y. Lo and K. T. W. Choi. Building defects diagnosis by infrared thermography. *Structural survey*, 22(5):259–263, 2004. original-pdf:1100220503.pdf. `doi:10.1108/02630800410571571`.

[63] Carosena Meola, Rosa Di Maio, Nicola Roberti, and Giovanni Maria Carlomagno. Application of infrared thermography and geophysical methods for defect detection in architectural structures. *Engineering failure analysis*, 12(6):875–892, 2005. ObjectType-Article-2. `doi:10.1016/j.engfailanal.2004.12.030`.

[64] S. Sfarra, E. Marcucci, D. Ambrosini, and D. Paoletti. Infrared exploration of the architectural heritage: From passive infrared thermography to hybrid infrared thermography (hirt) approach. *Materiales de construccion (Madrid)*, 66(323):e094–e094, 2016. ObjectType-Article-1. `doi:10.3989/mc.2016.07415`.

[65] Anna Ostanska. Thermal imaging for detection of defects in envelopes of buildings in use: Qualitative and quantitative analysis of building energy performance. *Periodica polytechnica. Civil engineering. Bauingenieurwesen*, 62(4):939–946, 2018. `doi:10.3311/PPci.12148`.

[66] Iole Nardi, Elena Lucchi, Tullio de Rubeis, and Dario Ambrosini. Quantification of heat energy losses through the building envelope: A state-of-the-art analysis with critical and comprehensive review on infrared thermography. *Building and environment*, 146:190–205, 2018. `doi:10.1016/j.buildenv.2018.09.050`.

[67] Muhd Zubair Tajol Anuar, Noor Nabilah Sarbini, Izni Syahrizal Ibrahim, Siti Hajar Othman, and Mohd Nadzri Reba. Building condition ratings using infrared thermography: a preliminary study. *Archives of civil engineering*, 68(4):403–418, 2022. `doi:10.24425/ace.2022.143046`.

[68] Hong Kong Concrete Institute. Detection of building surface defect by infrared thermography, 2009.

[69] H. Wiggenhauser. Active ir-applications in civil engineering. *Infrared physics & technology*, 43(3):233–238, 2002. `doi:10.1016/S1350-4495(02)00145-7`.

[70] Hisashi Tanaka, Seiichi Tottori, and Tatsuya Nihei. Detection of concrete spalling using active infrared thermography. *Quarterly Report of RTRI*, 47(3):138–144, 2006. `doi:10.2219/rtriqr.47.138`.

[71] Ralf W. Arndt. Square pulse thermography in frequency domain as adaptation of pulsed phase thermography for qualitative and quantitative applications in cultural heritage and civil engineering. *Infrared physics & technology*, 53(4):246–253, 2010. `doi:10.1016/j.infrared.2010.03.002`.

[72] Carosena Meola. Infrared thermography in the architectural field. *TheScientificWorld*, 2013(2013):1–8, 2013. ObjectType-Article-2. `doi:10.1155/2013/323948`.

[73] Qin Luo, Bin Gao, W. L. Woo, and Yang Yang. Temporal and spatial deep learning network for infrared thermal defect detection. *NDT & E international : independent nondestructive testing and evaluation*, 108:102164, 2019. `doi:10.1016/j.ndteint.2019.102164`.

[74] Babar Nasim Khan Raja, Saeed Miramini, Colin Duffield, Massoud Sofi, Priyan Mendis, and Lihai Zhang. The influence of ambient environmental conditions in detecting bridge concrete deck delamination using infrared thermography (irt). *Structural control and health monitoring*, 27(4):n/a, 2020. `doi:10.1002/stc.2506`.

[75] Azusa Watase, Recep Birgul, Shuhei Hiasa, Masato Matsumoto, Koji Mitani, and F. Necati Catbas. Practical identification of favorable time windows for infrared thermography for concrete bridge evaluation. *Construction & building materials*, 101:1016–1030, 2015. `doi:10.1016/j.conbuildmat.2015.10.156`.

[76] Michal Janku, Ilja Brezina, and Jiri Grosek. Use of infrared thermography to detect defects on concrete bridges. volume 190, pages 62–69. Elsevier Ltd, 2017. `doi:10.1016/j.proeng.2017.05.308`.

[77] Tarek Omar, Moncef L. Nehdi, and Tarek Zayed. Infrared thermography model for automated detection of delamination in rc bridge decks. *Construction & building materials*, 168:313–327, 2018. `doi:10.1016/j.conbuildmat.2018.02.126`.

[78] Michal Janku, Petr Cikrle, Jiri Grosek, Ondrej Anton, and Josef Stryk. Comparison of infrared thermography, ground-penetrating radar and ultrasonic pulse echo for detecting delaminations in concrete bridges. *Construction & building materials*, 225:1098–1111, 2019. `doi:10.1016/j.conbuildmat.2019.07.320`.

[79] Chongsheng Cheng, Zhexiong Shang, and Zhigang Shen. Automatic delamination segmentation for bridge deck based on encoder-decoder deep learning through uav-based thermography. *NDT & E international : independent nondestructive testing and evaluation*, 116:102341, 2020. `doi:10.1016/j.ndteint.2020.102341`.

[80] Ecem Edis, Inês Flores-Colen, and Jorge de Brito. Passive thermographic detection of moisture problems in facades with adhered ceramic cladding. *Construction & building materials*, 51:187–197, 2014. ObjectType-Article-2. `doi:10.1016/j.conbuildmat.2013.10.085`.

[81] Giovanni Maria Carlomagno, Rosa Di Maio, Carosena Meola, and Nicola Roberti. Infrared thermography and geophysical techniques in cultural heritage conservation. *Quantitative infrared thermography*, 2(1):5–24, 2005. `doi:10.3166/qirt.2.5-24`.

[82] E. Z. Kordatos, D. A. Exarchos, C. Stavrakos, A. Moropoulou, and T. E. Matikas. Infrared thermographic inspection of murals and characterization of

degradation in historic monuments. *Construction & building materials*, 48:1261–1265, 2013. `doi:10.1016/j.conbuildmat.2012.06.062`.

[83] P. Theodorakeas, E. Cheilakou, E. Ftikou, and M. Koui. Passive and active infrared thermography: An overview of applications for the inspection of mosaic structures. *33RD UIT (ITALIAN UNION OF THERMO-FLUID DYNAMICS) HEAT TRANSFER CONFERENCE*, 655(1):12061, 2015. `doi:10.1088/1742-6596/655/1/012061`.

[84] Akira Hoyano, Kohichi Asano, and Takehisa Kanamaru. Analysis of the sensible heat flux from the exterior surface of buildings using time sequential thermography. *Atmospheric environment (1994)*, 33(24):3941–3951, 1999. `doi:10.1016/S1352-2310(99)00136-3`.

[85] Matthew Fox, David Coley, Steve Goodhew, and Pieter De Wilde. Time-lapse thermography for building defect detection. *Energy and buildings*, 92:95–106, 2015. `doi:10.1016/j.enbuild.2015.01.021`.

[86] Elton Bauer, Elier Pavón, Elias Oliveira, and Claudio H. F. Pereira. Facades inspection with infrared thermography: cracks evaluation. *Journal of building pathology and rehabilitation*, 1(1), 2016. `doi:10.1007/s41024-016-0002-9`.

[87] Mohanned Al Gharawi, Yaw Adu-Gyamfi, and Glenn Washer. A framework for automated time-lapse thermography data processing. *Construction & building materials*, 227:116507, 2019. `doi:10.1016/j.conbuildmat.2019.07.233`.

[88] Tarek Rakha, Yasser El Masri, Kaiwen Chen, Eleanna Panagoulia, and Pieter De Wilde. Building envelope anomaly characterization and simulation using drone time-lapse thermography. *Energy and buildings*, 259(C):111754, 2022. USDOE Office of Energy Efficiency and Renewable Energy (EERE). `doi:10.1016/j.enbuild.2021.111754`.

[89] Nitin Nagesh Kulkarni, Koosha Raisi, Nicholas A. Valente, Jason Benoit, Tzuyang Yu, and Alessandro Sabato. Deep learning augmented infrared thermography for unmanned aerial vehicles structural health monitoring of roadways. *Automation in construction*, 148:104784, 2023. `doi:10.1016/j.autcon.2023.104784`.

[90] Tarek Omar and Moncef L. Nehdi. Remote sensing of concrete bridge decks using unmanned aerial vehicle infrared thermography. *Automation in construction*, 83:360–371, 2017. `doi:10.1016/j.autcon.2017.06.024`.

[91] Sandra Pozzer, Ehsan Rezazadeh Azar, Francisco Dalla Rosa, and Zacarias Martin Chamberlain Pravia. Semantic segmentation of defects in infrared thermographic images of highly damaged concrete structures. *Journal of performance of constructed facilities*, 35(1), 2021. `doi:10.1061/(ASCE)CF.1943-5509.0001541`.

[92] Sandra Pozzer, Gabriel Ramos, Ehsan Rezazadeh Azar, Ahmad Osman, Ahmed El Refai, Fernando López, Clemente Ibarra-Castanedo, and Xavier Maldague. Enhancing concrete defect segmentation using multimodal data and siamese neural networks. *Automation in construction*, 166:105594, 2024. `doi:10.1016/j.autcon.2024.105594`.

[93] Christopher Dunderdale, Warren Brettenny, Chantelle Clohessy, and E. Ernest Dyk. Photovoltaic defect classification through thermal infrared imaging using a machine learning approach. *Progress in photovoltaics*, 28(3):177–188, 2020. `doi:10.1002/pip.3191`.

[94] Yahya Zefri, Imane Sebari, Hicham Hajji, and Ghassane Aniba. Developing a deep learning-based layer-3 solution for thermal infrared large-scale photovoltaic module inspection from orthorectified big uav imagery data. *International Journal of Applied Earth Observation and Geoinformation*, 106:102652, 2022. `doi:10.1016/j.jag.2021.102652`.

[95] Qiang Fang and Xavier Maldague. A method of defect depth estimation for simulated infrared thermography data with deep learning. *Applied sciences*, 10(19):6819, 2020. `doi:10.3390/app10196819`.

[96] Gwanyong Park, Minhyung Lee, Hyangin Jang, and Changmin Kim. Thermal anomaly detection in walls via cnn-based segmentation. *Automation in construction*, 125:103627, 2021. `doi:10.1016/j.autcon.2021.103627`.

[97] Ivana Walter, Marko Tanaskovic, and Milos Stankovic. Ir building analysis with extraction of elements using image segmentation and retinanet. *Buildings (Basel)*, 13(1):109, 2023. `doi:10.3390/buildings13010109`.

[98] Changmin Kim, Gwanyong Park, Hyangin Jang, and Eui-Jong Kim. Automated classification of thermal defects in the building envelope using thermal and visible images. *Quantitative infrared thermography*, 20(3):106–122, 2023. `doi:10.1080/17686733.2022.2033531`.

[99] I. Garrido, S. Lagüela, Q. Fang, and P. Arias. Introduction of the combination of thermal fundamentals and deep learning for the automatic thermographic inspection of thermal bridges and water-related problems in infrastructures. *Quantitative infrared thermography*, 20(5):231–255, 2023. `doi:10.1080/17686733.2022.2060545`.

[100] Tamas Aujeszky, Georgios Korres, and Mohamad Eid. Material classification with laser thermography and machine learning. *Quantitative infrared thermography*, 16(2):181–202, 2019. `doi:10.1080/17686733.2018.1539895`.

[101] Yan Yu Celia YANG. *Characterization of Geospatial Data on Geotechnical and Geological Features with Thermal Infrared Imaging*. Thesis, 2023.

[102] Yi Na MOK. *Development of a Machine-Learning Based Framework on External Wall Debond Evaluation and Size Estimation Via Passive Thermography*. Thesis, 2024.

[103] S Mineo, D Calcaterra, S Perriello Zampelli, and G Pappalardo. Application of infrared thermography for the survey of intensely jointed rock slopes. rend online soc geol it 35: 212–215, 2015.

[104] Giovanna Pappalardo and Simone Mineo. Study of jointed and weathered rock slopes through the innovative approach of infrared thermography. *Landslides: Theory, Practice and Modelling*, pages 85–103, 2018. `doi:10.1007/978-3-319-77377-3_5`.

[105] Thomas Junique, Patricia Vazquez, Céline Thomachot-Schneider, Issra Hassoun, Mirlène Jean-Baptiste, and Yves Géraud. The use of infrared thermography on the measurement of microstructural changes of reservoir rocks induced by temperature. *Applied sciences*, 11(2):1–23, 2021. `doi:10.3390/app11020559`.

[106] Nicola Casagli, William Frodella, Stefano Morelli, Veronica Tofani, Andrea Ciampalini, Emanuele Intrieri, Federico Raspini, Guglielmo Rossi, Luca Tanteri, and Ping Lu. Spaceborne, uav and ground-based remote sensing techniques for landslide mapping, monitoring and early warning. *Geoenvironmental disasters*, 4(1):1–23, 2017. `doi:10.1186/s40677-017-0073-1`.

[107] KC Feely and PR Christensen. Modal abundances of rocks using infrared emission spectroscopy. In *Lunar and Planetary Science Conference*, volume 28, page 349.

[108] Simone Mineo and Giovanna Pappalardo. Rock emissivity measurement for infrared thermography engineering geological applications. *Applied sciences*, 11(9):3773, 2021. `doi:10.3390/app11093773`.

[109] G. Pappalardo and S. Mineo. Investigation on the mechanical attitude of basaltic rocks from mount etna through infrared thermography and labo-

ratory tests. *Construction & building materials*, 134:228–235, 2017. `doi:10.1016/j.conbuildmat.2016.12.146`.

[110] Giovanna Pappalardo. First results of infrared thermography applied to the evaluation of hydraulic conductivity in rock masses. *Hydrogeology journal*, 26(2):417–428, 2018. `doi:10.1007/s10040-017-1670-5`.

[111] S. Mineo and G. Pappalardo. Infrared thermography presented as an innovative and non-destructive solution to quantify rock porosity in laboratory. *International journal of rock mechanics and mining sciences (Oxford, England : 1997)*, 115:99–110, 2019. `doi:10.1016/j.ijrmms.2019.01.012`.

[112] William Frodella, Mikheil Elashvili, Daniele Spizzichino, Giovanni Gigli, Luka Adikashvili, Nikoloz Vacheishvili, Giorgi Kirkitadze, Akaki Nadaraia, Claudio Margottini, and Nicola Casagli. Combining infrared thermography and uav digital photogrammetry for the protection and conservation of rupestrian cultural heritage sites in georgia: A methodological application. *Remote sensing (Basel, Switzerland)*, 12(5):892, 2020. `doi:10.3390/rs12050892`.

[113] Renlian Zhou, Zhiping Wen, and Huaizhi Su. Automatic recognition of earth rock embankment leakage based on uav passive infrared thermography and deep learning. *ISPRS journal of photogrammetry and remote sensing*, 191:85–104, 2022. `doi:10.1016/j.isprsjprs.2022.07.009`.

[114] Lidia Loiotine, Gioacchino Francesco Andriani, Marc-Henri Derron, Mario Parise, and Michel Jaboyedoff. Evaluation of infrared thermography supported by uav and field surveys for rock mass characterization in complex settings. *Geosciences (Basel)*, 12(3):116, 2022. `doi:10.3390/geosciences12030116`.

[115] V. Vivaldi, M. Bordoni, S. Mineo, M. Crozi, G. Pappalardo, and C. Meisina. Airborne combined photogrammetry—infrared thermography applied to land-

slide remote monitoring. *Landslides*, 20(2):297–313, 2023. `doi:10.1007/s10346-022-01970-z`.

[116] Christopher Small and Daniel Sousa. Robust cloud suppression and anomaly detection in time-lapse thermography. *Remote sensing (Basel, Switzerland)*, 16(2):255, 2024. `doi:10.3390/rs16020255`.

[117] Mark Settle. Workshop on geological applications of thermal infrared remote sensing techniques: a lunar and planetary institute workshop, february 11-13, 1980, 1980.

[118] Joseph R. Michalski, Stephen J. Reynolds, Thomas G. Sharp, and Philip R. Christensen. Thermal infrared analysis of weathered granitic rock compositions in the sacaton mountains, arizona: Implications for petrologic classifications from thermal infrared remote-sensing data. *J. Geophys. Res*, 109(E3):E03007–n/a, 2004. `doi:10.1029/2003JE002197`.

[119] N. K. Bansal, S. N. Garg, and S. Kothari. Effect of exterior surface colour on the thermal performance of buildings. *Building and environment*, 27(1):31–37, 1992. ObjectType-Article-2. `doi:10.1016/0360-1323(92)90005-A`.

[120] L. Doulos, M. Santamouris, and I. Livada. Passive cooling of outdoor urban spaces. the role of materials. *Solar energy*, 77(2):231–249, 2004. ObjectType-Article-2. `doi:10.1016/j.solener.2004.04.005`.

[121] B. Lehmann, K. Ghazi Wakili, Th Frank, B. Vera Collado, and Ch Tanner. Effects of individual climatic parameters on the infrared thermography of buildings. *Effects of individual climatic parameters on the infrared thermography of buildings*, 110:29–43, 2013.

[122] A. Chudnovsky, E. Ben-Dor, and H. Saaroni. Diurnal thermal behavior of selected urban objects using remote sensing measurements. *Energy and build-*

ings, 36(11):1063–1074, 2004. ObjectType-Article-1. `doi:10.1016/j.enbuild.2004.01.052`.

[123] Z. K. Huang and K. W. Chau. A new image thresholding method based on gaussian mixture model. *Applied Mathematics and Computation*, 205(2):899–907, 2008. `doi:10.1016/j.amc.2008.05.130`.

[124] I. N. Bankman, Inc ebrary, and ScienceDirect. *Handbook of medical image processing and analysis.* Academic Press series in biomedical engineering. Elsevier/Academic Press, Burlington, MA, 2nd edition, 2009.

[125] Judith M. S. Prewitt and Mortimer L. Mendelsohn. The analysis of cell images. *Annals of the New York Academy of Sciences*, 128(3):1035–1053, 1966. `doi:10.1111/j.1749-6632.1965.tb11715.x`.

[126] W. Doyle. Operations useful for similarity-invariant pattern recognition. *Journal of the ACM*, 9(2):259–267, 1962. `doi:10.1145/321119.321123`.

[127] Nobuyuki Otsu. A threshold selection method from gray-level histograms. *IEEE transactions on systems, man, and cybernetics*, 9(1):62–66, 1979. `doi:10.1109/TSMC.1979.4310076`.

[128] Lydia S. Y. Chiu;, C. P. Yuen;, Wallace W. L. Lai;, and Janet F. C. Sham. Selection of thresholding for defect detection and size estimation of building exterior wall using time-lapse infrared thermography. In *17th Quantitative InfraRed Thermography Conference*, 2024.

[129] E. R. Davies. *Computer and Machine Vision: Theory, Algorithms, Practicalities.* San Diego: Elsevier Science & Technology, San Diego, 2012.

[130] Tess X. H. Luo, Wallace W. L. Lai, and Zhanzhan Lei. Intensity normalisation of gpr c-scans. *Remote sensing (Basel, Switzerland)*, 15(5):1309, 2023. `doi:10.3390/rs15051309`.

[131] Solveig Badillo, Balazs Banfai, Fabian Birzele, Iakov I. Davydov, Lucy Hutchinson, Tony Kam-Thong, Juliane Siebourg-Polster, Bernhard Steiert, and Jitao David Zhang. An introduction to machine learning. *Clinical pharmacology and therapeutics*, 107(4):871–885, 2020. `doi:10.1002/cpt.1796`.

[132] I. H. Witten, Eibe Frank, and Mark A. Hall. *Data mining : practical machine learning tools and techniques*. Morgan Kaufmann Publisher, Cambridge, MA, fourth edition. edition, 2017.

[133] Han Jiawei, Kamber Micheline, and Pei Jian. *3 - Data Preprocessing*, pages 83–124. Elsevier Inc, third edition edition, 2012. `doi:10.1016/B978-0-12-381479-1.00003-4`.

[134] Scikit-Learn. MinMaxScaler, 2024. URL: `https://scikit-learn.org/stable/modules/generated/sklearn.preprocessing.MinMaxScaler.html`.

[135] Scikit-Learn. StandardScaler, 2024. URL: `https://scikit-learn.org/stable/modules/generated/sklearn.preprocessing.StandardScaler.html#sklearn.preprocessing.StandardScaler`.

[136] Scikit-Learn. RobustScaler, 2024. URL: `https://scikit-learn.org/stable/modules/generated/sklearn.preprocessing.RobustScaler.html`.

[137] Ian Goodfellow, Yoshua Bengio, and Aaron Courville. *Deep learning*. Adaptive computation and machine learning. The MIT Press, London, England, 1 edition, 2016.

[138] Edwin Kah Pin Chong and Stanislaw H. Żak. *An introduction to optimization*. Wiley series in discrete mathematics and optimization. John Wiley & Sons, Inc., Hoboken, New Jersey, 4th edition, 2013. Includes bibliographical references and index.

[139] Trevor Hastie, Robert Tibshirani, and Jerome Friedman. *Elements of Statistical Learning: Data Mining, Inference, and Prediction*. Springer Series in

Statistics. Springer, New York, second edition edition, 2009. `doi:10.1007/978-0-387-84858-7`.

[140] Joel Grus and Inc ebrary. *Data science from scratch*. O'Reilly Media, Sebastopol, Calif, 1st edition, 2015.

[141] Tin Wai Phoebe Wong. *Imaging and Diagnosis of Corrosion in Reinforced Concrete Structures by Using Ground Penetrating Radar*. Thesis, 2023.

[142] ASTM. ASTM E1933 – 14 Standard Practice for Measuring and Compensating for Emissivity Using Infrared Imaging Radiometers, 2022. URL: `www.astm.org`.

[143] Hong Kong Observatory;. Daily extract of meteorological observations , january 2018, 2024. URL: `https://www.hko.gov.hk/en/cis/dailyExtract.htm?y=2018&m=1` [cited 2024-12-19].

[144] Hong Kong Observatory;. Daily extract of meteorological observations , february 2018, 2024. URL: `https://www.hko.gov.hk/en/cis/dailyExtract.htm?y=2018&m=2` [cited 2024-12-19].

[145] Hong Kong Observatory;. Daily extract of meteorological observations , march 2018, 2024. URL: `https://www.hko.gov.hk/en/cis/dailyExtract.htm?y=2018&m=3` [cited 2024-12-19].

[146] Hong Kong Observatory;. Daily weather summary and radiation level, 2024. URL: `https://www.hko.gov.hk/en/wxinfo/dailywx/dailywx.htm` [cited 2024-12-19].

[147] Hong Kong Observatory;. Daily mean amount of cloud (%) at the hong kong observatory 2018, 2024. URL: `https://www.hko.gov.hk/en/cis/dailyElement.htm?ele=CLD&y=2018` [cited 2024-12-19].

[148] Google. Google Maps PolyU's Road Lab, Shek Mun, Hong Kong, n.d. URL: `https://maps.app.goo.gl/8ws12nwCrf9LWe6i9` [cited 2024-12-20].

[149] Hong Kong Observatory;. Daily extract of meteorological observations , november 2021, 2024. URL: `https://www.hko.gov.hk/en/cis/dailyExtract.htm?y=2021&m=11` [cited 2024-12-19].

[150] Hong Kong Observatory;. Daily extract of meteorological observations , december 2021, 2024. URL: `https://www.hko.gov.hk/en/cis/dailyExtract.htm?y=2021&m=12` [cited 2024-12-19].

[151] Hong Kong Observatory;. Daily mean amount of cloud (%) at the hong kong observatory 2021, 2024. URL: `https://www.hko.gov.hk/en/cis/dailyElement.htm?ele=CLD&y=2021` [cited 2024-12-19].

[152] Google. Google Maps Ping Che, Fanling, Hong Kong, n.d. URL: `https://maps.app.goo.gl/NwVByEGvmCRTeS549` [cited 2024-12-21].

[153] Hong Kong Observatory;. Daily total bright sunshine (hours) at king's park 2021, 2024. URL: `https://www.hko.gov.hk/en/cis/dailyElement.htm?ele=SUNSHINE&y=2021` [cited 2024-12-19].

[154] Google. Google Maps PolyU Block W, Hung Hom, Hong Kong, n.d. URL: `https://maps.app.goo.gl/uVtygWSntEiekF9E6` [cited 2024-12-20].

[155] Hong Kong Observatory;. Daily extract of meteorological observations , september 2021, 2024. URL: `https://www.hko.gov.hk/en/cis/dailyExtract.htm?y=2021&m=9` [cited 2024-12-19].

[156] Hong Kong Observatory;. Daily extract of meteorological observations , july 2022, 2024. URL: `https://www.hko.gov.hk/en/cis/dailyExtract.htm?y=2022&m=7` [cited 2024-12-19].

[157] Hong Kong Observatory;. Daily mean amount of cloud (%) at the hong kong observatory 2022, 2024. URL: `https://www.hko.gov.hk/en/cis/dailyElement.htm?ele=CLD&y=2022` [cited 2024-12-19].

[158] Google. Google Maps UNESCO Global Geopark, Sai Kung, Hong Kong, n.d. URL: `https://maps.app.goo.gl/2h3gervyof5ur82q6` [cited 2024-12-19].

[159] Geotechnical Engineering Office. GEO Report No. 336 - Detailed Study of the 21 May 2016 Landslide on the Natural Hillside above Slope No. 8SE-A/F34 at Sai Kung Sai Wan Road, Sai Kung. Report, Geotechnical Engineering Office, 2018.

[160] Geotechnical Control Office. Hong Kong Geological Survey Memoir No. 4 - Geology of Sai Kung and Clear Water Bay. Report, 1990.

[161] Geotechnical Control Office. Sai Kung Peninsula: Solid and Superficial Geology , Hong Kong Geological Survey, Map Series HGM 20 , Sheet 8, 1:20,000 scale., 1989.

[162] Google. Google Maps Sai Wan Road, Saikung, Hong Kong, n.d. URL: `https://maps.app.goo.gl/ktg9F1Svj8XBRLkU8` [cited 2024-12-21].

[163] E. Garcia, A. de Pablos, M. A. Bengoechea, L. Guaita, M. I. Osendi, and P. Miranzo. Thermal conductivity studies on ceramic floor tiles. *CERAM INT*, 37(1):369–375, 2011. `doi:10.1016/j.ceramint.2010.09.023`.

[164] Tomas Lourenco, Luis Matias, and Paulina Faria. Anomalies detection in adhesive wall tiling systems by infrared thermography. *Construction and Building Materials*, 148:419–428, 2017. `doi:10.1016/j.conbuildmat.2017.05.052`.

[165] Geotechnical Engineering Office. Geoguide 3 Guide to Rock and Soil Descriptions, 2017.

[166] M. M. Barbero-Barrera, N. Flores-Medina, and E. Moreno-Fernandez. Thermal, physical and mechanical characterization of volcanic tuff masonries for the restoration of historic buildings. *Materiales de construccion (Madrid)*, 69(333):179–e179, 2019. `doi:10.3989/mc.2019.12917`.

[167] Janet FC Sham, Wallace WL Lai, and Sin Yau Chiu. Effects of thermal contrast on size estimation of debonds in different external wall's composite finishes via passive infrared thermography and a modified gradient algorithm. In *The 3rd QIRT Conference Asia*, 2019.